RECRYSTALLIZATION IN TWO-PHASE ALLOYS

I. Baker

St. Catherine's College

Oxford.

A thesis submitted for the degree of Doctor of Philosophy in the University of Oxford, Trinity Term 1982.

Ian Baker
St. Catherine's College

D.Phil Thesis
Trinity Term 1982

Recrystallization in two-phase alloys

ABSTRACT

This study is concerned with the effect of particles, which are too small to produce Particle Stimulated Nucleation, on recrystallization. A single crystal model system of internally oxidised copper-aluminium was deformed by rolling. The deformed and annealed structures were investigated both electron-microscopically and optically. Measurements of the stored energy of deformation were combined with measurements of the recrystallization kinetics by the use of anisothermal differential scanning calorimetry.

The effect of particles on the mechanical properties of metals and the microstructural inhomogeneities produced during deformation in the single phase are reviewed. The literature concerning recrystallization is surveyed with emphasis on the possible sites for nucleation and the effects of a second phase.

Comparison of the deformed structure of copper-alumina and copper revealed that cells form at lower strains in the particle-containing material. These cells are smaller than those found in copper and show alignment with {111} planes. Dynamic recovery at higher strains leads to the formation of a banded structure from these cells. Microbands were found at all strains, they increased in frequency and decreased in width as the strain increased. Misorientation measurements using STEM microdiffraction could find no evidence of a slip homogenizing effect due to the particles, in fact larger misorientations were found across cell boundaries in particle-containing material.

Addition of particles raised the stored energy and this increase was greater at higher strains. A comparison of the recrystallization kinetics of particle-hardened and single phase material found complex behaviour in the former. Increasing the strain could lead to a change from complete suppression, to retardation, to acceleration of recrystallization in two-phase alloys. A model based on the properties of microbands and particle pinning is presented to account for these effects.

Acknowledgements

Many people have helped me in the course of this research project, I should like to extend my thanks to them all. In particular I should like to thank the following:-

Professor Sir Peter Hirsch F.R.S. for the provision of laboratory facilities.

The Science Research Council for financial support.

My supervisor Dr. J.W. Martin for his help and advice throughout this project.

Dr. R.D. Doherty and Dr. M.G. Scott of the University of Sussex for the use of the calorimeters.

The members of the laboratory workshop for their assistance, especially Mr. D.W. Pinfold.

The other members of the J.W.M. group especially Jeff Crompton, John Blind, Bill Clegg and Lyndon Edwards for their help, encouragement and friendship.

Helen Clamp for help with the preparation of the figures and photographs, proof reading and for her patience and gentle encouragement during the course of this project.

Jeff Crompton and Adrian Hopgood for their proof reading.

Glynis Edwards for her patient help and careful typing of this thesis.

Ian Baker

June 1982.

Preface

This thesis is an account of research carried out in the Department of Metallurgy and Science of Materials at the University of Oxford between October 1979 and June 1982. The work reported is original and is not substantially the same as any thesis submitted in this or any other university. Where the work of other authors has been included in this text this has been acknowledged and its source given in an alphabetical list of references at the end of the thesis. Part of this work has been presented at the 1st Risø International Symposium 'Recrystallization and Grain Growth in Multi-Phase and Particle-Containing Alloys', Roskilde, Denmark, September 1980. Papers based on this work will also be presented at the 5th International Conference on the Strength of Metals and Alloys, Melbourne, Australia, August 1982 and the 10th International Congress on Electron Microscopy, Hamburg, W. Germany, August, 1982.

Index

Chapter 1

Review of Literature

1.1 Introduction

This work is primarily concerned with the effect of small particles on recrystallization. It is now generally accepted that for an understanding of recrystallization the deformation microstructure needs to be characterized. Thus, this chapter starts by considering the macroscopic manifestation of particles on the mechanical properties of metals and the microscopic relaxation effects at particles which lead to dislocation formation. The terminology used to describe the microstructural features of deformation, with particular reference to the rolling deformation used here, is outlined.

In the second part of this chapter the general recrystallization phenomena and kinetics of primary recrystallization are described. The current nucleation mechanisms are reviewed and their occurrence at the microstructural features of deformation is discussed. The effect of solute elements on the kinetics of primary recrystallization is then briefly considered. Finally, the effect of a second-phase on recrystallization kinetics is described and the chapter closes by outlining the proposed work concerning the effect of small particles on recrystallization kinetics.

1.2 Particle Effects

1.2.1 The Effect of Particles on Tensile Deformation

The effect of a hard dispersed phase on the mechanical properties of metals and alloys has been extensively investigated in particular by conducting tensile tests on internally oxidised F.C.C. single crystals and Polycrystals.

Fig. 1.1 shows typical stress-strain data for pure and dispersion hardened copper polycrystals. Increasing the volume fraction of particles increases the yield stress and the initial work hardening rate. However, in the later stages of work hardening, the work hardening rate becomes similar to that of the pure metal and the curves only differ by approximately the difference in yield stress. Fisher, Hart and Pry (1953) first presented a model to explain this work hardening increment, τ_h, based on the Orowan mechanism shown in fig. 1.2. They obtained the result that

$$\tau_h \propto \frac{F_v^{3/2}}{r} \qquad (1.1)$$

where F_v is the volume fraction of particles and r the particle radius. Ashby (1966) suggested that this model would break down at small strains due to plastic relaxation and the equation has subsequently been shown to be incorrect e.g. fig. 1.1. Humphreys and Martin (1967) found no evidence of Orowan loops but did find prismatic loops and helices in $[\bar{1}01]$ directions in copper-silica.

The effect of hard second-phase particles on the well-known three-stage stress-strain curves of single phase F.C.C. single crystals has also been extensively investigated, fig. 1.3. It is found that increasing the volume fraction of particles increases the yield stress and the initial work hardening rate, thus transforming the linear stage I of easy glide into a stage α of parabolic hardening. The extent of stage α increases with increasing volume fraction of particles. Again, after the initially greater work hardening rate the stages β and γ of the dispersion hardened alloy are essentially the same as stages II and III in the pure metal. This indicates that the work hardening behaviour is controlled by the matrix after the initial stages and not by the particles.

Experimental data indicate that the yield stress in dispersion hardened alloys can be approximated by

$$\tau_y \sim \frac{Gb}{\lambda} \qquad (1.2)$$

where G is the shear modulus, b the Burgers vector and λ the interparticle spacing, shown in fig. 1.2; for example see fig. 1.4. Note that because in general the particles will not be distributed in an even array, dislocations will at first find easy paths between the particles, giving rise to a significant amount of microstrain prior to general yield.

As deformation proceeds, more loops are left around the particles so that the effective interparticle spacing decreases and thus the flow stress required to push a dislocation through the particles increases. However, after a small number of loops have formed the stress build up around the particles will result in plastic

relaxation. This flow stress has been found experimentally by Ebeling and Ashby (1966) to be given by

$$\tau = \tau_y + K\left[\frac{\gamma F_v}{r}\right]^{1/2} \qquad (1.3)$$

where K is a constant, γ is the true strain and F_v and r are the volume fraction and particle radius.

Ashby (1970) calls the dislocations required to accommodate particles 'geometrically necessary' (density ρ_G) and the dislocations which occur even in a single phase material 'statistically stored' (density ρ_s). The total number of dislocations is then $\rho_G + \rho_s$. ρ_G is given by

$$\rho_G = \frac{4\gamma F_v}{rb} \qquad (1.4)$$

This is an upper limit to ρ_G as some dislocations will disappear by mutual annihilation. Hirsch and Humphreys (1970) and Russell and Ashby (1970) measured ρ_G at low strains and found it to be near the theoretical value.

Ashby (1970) points out that in Stage II ρ_s increases as γ^2 whilst ρ_G increases as γ so that at high strains, ρ_G maybe swamped by ρ_s. Thus, geometrically necessary dislocations may only be important at low strains. This is partially confirmed by the work of Grant (1964), see table 1.1 below:-

Composition	Yield strength after internal oxidation (1000PSi)	After internal oxidation and 50% reduction. Yield strength (1000PSi)
Pure Cu	7.8	64
Cu-0.04%Al	16	65
Cu-0.22%Al	30	70
Cu-0.44%Al	35	70

Table 1.1 after Grant (1964)

He found that at high strains the difference in strength between pure and dispersion-hardened alloys was reduced. Thus, it is considered that at high strains the dislocation density in two-phase alloys will be higher than the single phase material but not significantly so.

1.2.2 Plastic Relaxation Mechanisms

The Orowan loops in fig. 1.2 can arrange themselves in two ways; i) in concentric arrays when the particle size is smaller than the slip line spacing, fig. 1.5a; ii) in a uniform stack when the particle size is of the same order as the slip line spacing, fig. 1.5b.

At room temperature deformed specimens can recover some of the work hardening. The simplest mechanism for this is by conservative climb of the Orowan loops, fig. 1.6, as proposed by Hirsch and Humphreys (1970). They found that whilst in Stage I up to 40% of the work hardening is recoverable in copper alumina, this falls to only 1% in stage II. Similar recovery has not been reported in polycrystals.

Humphreys (1980a) has surveyed the mechanisms of plastic

relaxation around particles and these will now be briefly reviewed. He has considered in general terms the ways in which plastic relaxation is possible. He considered a particle in a matrix, fig. 1.7(a), which is deformed by shear on the primary slip plane, fig. 1.7(b). If the particle does not deform as shown then a relaxation mechanism must occur in the matrix so that the particle may be accommodated. These mechanisms will cause the transfer of material from region A to region B. This can occur in two ways:- by transfer of matter to or from regions remote from the particle, fig. 1.7(c), (d) or by transfer of matter locally around the particle fig. 1.7(e), (f): the Orowan loop climb mechanism fits into (e). Fig. 1.8 shows in detail all the possible mechanisms. Fig. 1.8(a) and (b) show relaxation by the formation of primary prismatic loops; in (a) by generation of interstitial and vacancy loops and in (b) by generation of interstitial loops and voids. Similarly, fig. 1.8(c) and (d) show plastic relaxation by the formation of secondary prismatic loops; in (c) by interstitial and vacancy loops and in (d) by interstitial loops and voids. Humphreys (1980a) states that the dislocation mechanisms involved in the lattice rotations in fig. 1.7(e) and (f) are not well understood; however those that have been measured e.g. Humphreys (1979b) have always been of the type shown in fig. 1.7(e). Humphreys and Stewart (1972) proposed that the rotations could be accounted for by the shear loops shown in fig. 1.9. Humphreys (1979a) has shown that for a given strain the lattice rotations start at particle diameters of about 0.1 microns and increase with particle size up to 1 micron, fig. 1.10. Above this size, the rotations are particle size independent but increase as a function of strain as shown in fig. 1.11.

In addition to the above mechanisms very small particles may shear or fracture if the particle size is such that $r/b \leq 5$.

Humphreys (1980a) has considered all the above mechanisms as a function of particle size and strain for copper-silica. He plots r/b versus strain, fig. 1.12, in which each mechanism occupies a certain regime of particle size and strain.

1.3 Microstructural Features after Deformation

In reviewing the features that can be formed during deformation (usually rolling) of metals, the definitions of Malin and Hatherly (1979a) will be adopted; although confusingly these definitions have not been used by all workers.

A CELL can be defined as an array of dislocations surrounding an essentially dislocation-free region. Cells are formed at an early stage of rolling in high stacking fault energy metals e.g. as found by Swann (1963) in copper. The cells are usually equiaxed but may become elongated during rolling. The DISLOCATION DOMAIN is the unit within a cell into which the dislocations may be arranged. The dislocation domain is the 'effective particle size' of X-ray line broadening experiments. A POLYGONIZED CELL structure is present in aluminium after room temperature deformation e.g. Faivre and Doherty (1979) and may form in other metals from the cell structure after annealing. The larger polygonized cells which have started to migrate are sometimes termed SUBGRAINS.

MICROBANDS are long, thin (0.25microns) sheet-like features found in copper and other high stacking fault energy metals and alloys. They were first observed by Essman (1965) in tensile deformed single

crystal copper. Ahlborn and Sauer (1968) found that they formed at low strains (10%) and that their density increased with strain, whilst Horuchi et al. (1975) reported that they formed first on {111} planes in f.c.c. structures, further rolling causing them to cluster together and rotate towards the rolling plane. It has been suggested by Malin and Hatherly (1979b) that the Type III markings designated by Samuels (1954), which can be seen on a polished or etched surface, are manifestations of microbands.

TRANSITION BAND is the name given to the cluster of microbands separating adjacent areas of equiaxed cells. Hu (1963) and Walter and Koch (1963) found transition bands in silicon iron. Hu (1963) found a cumulative misorientation across them and drew the diagram shown in fig. 1.13 to demonstrate how they may form when deformation becomes inhomogeneous and the crystal breaks down into separate fragments of mutually misoriented regions. Dillamore et al. (1972) state the following four ways in which transition bands may arise

i) if, as a result of local differences in stress state, different parts of the crystal undergo different strains there will in general be some relative rotation.

ii) if the strain throughout a crystal is specified in all its components and is homogeneous, it is still possible that different combinations of slip systems may separately yield the imposed strain in different parts of the crystal, giving different slip rotations and causing relative rotation.

iii) a macroscopically imposed shape change may be achieved for a lower energy expenditure if the total strain is subdivided such that different regions undergo different strains, and again rotate relative to each other.

iv) a crystal may be oriented in such a way that it does not rotate when subjected to a specific strain, but that small displacements in opposite senses from the initial orientation would cause the two orientations to continue to diverge.

As transition bands and microbands are related to the crystallography they only occur within a single grain in polycrystals.

SHEAR BANDS were first noted by Grewen et al. (1977) in a Copper - 0.6%Chromium alloy. They were found to be about 2 microns thick, parallel to the transverse direction and inclined at 20-35° to the rolling plane. They are a form of plastic instability and occur in the area of a deforming zone which satisfies the condition $d\sigma/d\varepsilon < 0$ i.e. work softening occurs. They have been shown by Wakefield et al. (1977) to occur on the planes of maximum shear stress dictated by macroscopic plasticity and not by crystallographic glide; thus they can cut across grain boundaries. Dillamore et al. (1979), in an analysis of shear banding, came to the conclusion that the development of shear bands required not only that no more energy would be expended than during a homogeneous deformation, but also that the work softening was maximized through crystal rotation. They found experimentally that a strongly textured material could produce shear banding on a plane that is not the one predicted by the maximum macroscopic shear stress. Shear bands have more importance as the deformation increases so that above 90% deformation they become the dominant deformation mode. They have been found under severe loading by Craig and Stock (1970) adjacent to bullet holes in 70:30 brass.

Karduck, Goux and Gottstein (1979) found evidence of deformation twins in 75% rolled single crystal copper in the shear bands but none

in the matrix.

1.4 Recrystallization

1.4.1 Terminology and Classical Results

During plastic deformation of a metal at low temperatures most of the applied work is lost as heat and noise; however a small percentage (2-10%) is retained as the 'stored energy of cold work'. This stored energy manifests itself in the metal as an increase in :-

i) the number of dislocations (from 10^{10} - 10^{12} lines m^{-2} in the undeformed metal to 10^{14} - 10^{16} lines m^{-2} in the deformed metal)

ii) dislocation interactions

iii) point defects; however, at room temperature in a low melting point metal most of the excess vacancies and interstitials are mobile enough to anneal out.

The way the dislocations arrange themselves depends on :-

i) the crystal structure of the material being deformed

ii) the temperature of deformation

iii) the strain

iv) the strain rate

v) the purity (including the way any impurities are arranged e.g. as a precipitate)

vi) the stacking fault energy.

The cold-worked metal is in a high energy state but cannot spontaneously lower its energy. A return to the low energy state can

be effected by annealing, during which two types of process occur - recovery and recrystallization.

Recovery can be defined as all changes which do not involve the migration of high angle grain boundaries. The driving force is the reduction in strain energy. During recovery the following changes can occur:-

i) point defect annihilation

ii) unlike dislocations attract and annihilate each other

iii) like dislocations may arrange themselves in a low energy configuration e.g. low angle tilt boundaries which separate regions differing in orientation by less than 5^{o}; this is sometimes referred to as polygonization. Cahn (1949) demonstrated that deformation led to asterism of X-ray Laue spots and recovery led to each spot being replaced by several.

During an isothermal anneal recovery usually precedes recrystallization. Recrystallization is defined as the sweeping of a metal by high angle grain boundaries. Recrystallization may itself be subdivided according to the definitions of Beck (1954).

Primary recrystallization is the process in which new grains are nucleated and grow into deformed material. It ends when the migrating grain boundaries impinge. The driving force for primary recrystallization is the reduction in the number of dislocations.

Grain growth is the process whereby grain boundaries continue to migrate through the recrystallized structure. This leads to a smaller number of grains and an increase in the average grain diameter. The driving force is the reduction in grain boundary area per unit volume. Grain growth takes two forms:-

i) normal or continuous grain growth is the uniform growth of grains

until the grains are of comparable size to the dimensions of the specimens, when they become pinned by thermal grooving.

ii) abnormal or discontinuous grain growth is where a few grains only grow to a very large size. This process often occurs when normal grain growth is inhibited, for example by particles. This process bears a resemblance to primary recrystallization and for this reason is often called secondary recrystallization.

During primary recrystallization grain boundaries move away from their centres of curvature whilst during grain growth they grow towards them.

Walter and Dunn (1959) used the term tertiary recrystallization to describe the process by which grains of the lowest surface energy grow at the expense of others. The driving force is the reduction in surface energy.

The present work is concerned only with primary recrystallization. A large amount of experimental information about primary recrystallization is embodied in the following six laws, formulated by Burke and Turnbull (1952):-

i) a minimum deformation is required to initiate recrystallization

ii) the smaller the degree of deformation the higher is the temperature required to initiate recrystallization

iii) increasing the annealing time decreases the temperature required for recrystallization

iv) the final grain size depends chiefly on the degree of deformation and, to a lesser extent, upon the annealing temperature; being smaller the greater the degree of deformation and the lower the temperature

v) the larger the original grain size, the greater the degree of

deformation required to give equivalent recrystallization

vi) the degree of deformation required to give equivalent deformational hardening increases with increasing temperature of working.

Cahn (1965) added to these:-

vii) new grains do not grow into deformed grains of identical or small misorientation.

1.4.2 The Kinetics of Recrystallization

The kinetics of primary recrystallization can be represented by a geometric model for an isothermal phase transformation. The volume fraction transformed, X_v, at a given time, t, is described by the following relationship proposed by Avrami (1939,1940,1941)

$$X_v = 1-\exp(-kt^n) \qquad (1.5)$$

where n lies between 3 and 4 for three-dimensional nucleation. Cahn (1956) showed that n would be between 2 and 3 for two-dimensional nucleation and between 1 and 2 for one-dimensional nucleation. For the case of three-dimensional recrystallization with a constant nucleation rate, $\dot{N}$, and growth rate, $\dot{G}$, Johnson and Mehl (1939) derived

$$X_v \simeq 1-\exp(-f\dot{G}^3\dot{N}t^4/4) \qquad (1.6)$$

where f is a shape factor. However, in practice both $\dot{N}$ and $\dot{G}$ may be time dependent, so in general this is

$$X_v = 1-\exp\left[-f\dot{G}(t)^3\ \dot{N}(t)\ t^4/4\right] \qquad (1.7)$$

Assuming two-dimensional nucleation Anderson and Mehl (1945)

showed good agreement between theoretical and experimental results for fine-grained, lightly-deformed aluminium, with the nucleation rate being an exponential function of time. The growth rate was time independent in this case, see fig. 1.14.

Deviations from the Avrami equation have been found. Vandermeer and Gordon (1963) noted that recrystallization in aluminium containing small amounts of copper and involving a long annealing time proceeded slower than predicted by the Avrami equation, fig. 1.15. This retardation of recrystallization was due to a slowing down in the growth rate. This slowing of the growth rate and the subsequent retardation of recrystallization was found to be more pronounced the lower the annealing temperature. They ascribed this deviation to the fact that recovery was still occurring in the material that had not recrystallized and thus the driving force was continually decreasing. They drew a schematic diagram showing the rate of stored energy evolution with time, showing the arbitrary overlap of the recovery and recrystallization processes, fig. 1.16.

Comte and Form (1976) using a Photo Emission Electron Microscope also found deviations from the Avrami equation at lower annealing temperatures in oxygen-free copper. They suggested that recrystallization did not go to completion but reached a saturation value, so that a modified Avrami equation could be written

$$X_v = X_v(\text{saturation})\left[1-\exp(-kt^n)\right] \qquad (1.8)$$

1.4.3 Nucleation Mechanisms

Most recent research has tried to gain an insight into nucleation mechanisms by direct observation rather than by a detailed kinetic analysis. Models of nucleation have to explain the monotonic increase of nucleation rate with strain and the incubation period prior to recrystallization plus the following electron-microscopical observations:-

i) nucleation occurs in regions of high defect concentration

ii) a mechanism must lead to the production of a strain-free subgrain of supercritical size which is surrounded, partially at least, by a high-angle boundary

iii) a nucleus must have a similar orientation to the region from which it forms.

Three principal fundamental mechanisms have been proposed to account for the nucleation of recrystallization:-

1) Classical nucleation theory

2) Subgrain growth

3) Strain Induced Boundary Migration.

1) Classical Nucleation Model

Burke and Turnbull (1952) first applied classical nucleation theory to the nucleation of recrystallization and obtained

$$r_c = \frac{-2\gamma}{E} \qquad (1.9)$$

for the critical embryo size, r_c and

$$\Delta F_{\tau(c)} = \frac{16\pi\gamma^3}{3E^2} \qquad (1.10)$$

for the change in free energy on formation of a viable nucleus, $\Delta F_{\tau(c)}$, where γ is the specific interfacial energy and E is the strain energy of the deformed material. Thus they derived an expression for the nucleation frequency, $\dot{N}_e$

$$\dot{N}_e = \frac{nkT}{h} \exp\left[\frac{-\Delta F_g}{kT}\right] \exp\left[\frac{-16\pi\gamma^3}{3kTE^2}\right] \qquad (1.11)$$

where h is Planck's constant;

k is Boltzmann's constant;

T is the absolute temperature

ΔF_g is the activation energy for grain boundary self diffusion

and n is the number of atoms per unit volume.

Taking reasonable values for the interfacial energy at a given strain (and thus a particular misorientation and strain energy) they produced the values for the critical nucleus size, r_c, and nucleation frequency, $\dot{N}_e$, for a homogeneous strain, shown in table 1.2.

Table 1.2 After Burke and Turnbull (1952)

The relationships between nucleation frequency ($\dot{N}_e$), minimum radius for a viable nucleus (r_c) and strain (e).

Strain (e)	Interfacial energy(γ) (ergs/cm^2)	Strain energy (E) (ergs/cm^{2}x10^{-8})	Minimum radius(r_c) (Å)	Nucleation Frequency($\dot{N}_e$) (sec^{-1}cm^{-3})
0.01	48	0.38	250	-
0.02	107	1.52	140	-
0.05	210	9.5	44	10^{-500}
0.10	310	38.0	16	10^{-100}
0.15	385	86.0	9	10^{-21}
0.20	450	152.0	6	10^{+3}
0.30	500	342.0	3	10^{+21}

From the data, it is unlikely that homogeneous nucleation would occur in the lightly deformed material, as large nuclei, 50nm, are required, the formation of which by random fluctuations is unlikely. Orowan (1954) has shown that the activation energy for such a process is very large at 10^8eV. Conversely, heterogeneous nucleation can occur if regions of high strain energy occur in the material. However, even if nucleation occurred in a region of high local strain (of greater than 0.2), once such a nucleus grew outside the high strain region it would become subcritical. Also, nuclei forming on this model would have a random orientation with respect to the deformed state; this is at variance with the experimental observations.

The model accounts for an incubation period and gives reasonable

nucleation frequencies. No experimental methods of disproving the model appear to exist and since nuclei which may be only 0.6nm across are close to the resolution of the electron microscope their observation would be difficult. However, because of the objections raised above and because other models fit the experimental evidence better, this model has been discarded.

2a) Subgrain Growth Model

Originally, subgrain growth, as proposed by Cottrell (1953) and based on the observations of Cahn (1950), predicted that some strain-free cells, formed by classical polygonization, grow to full size grains. A condition for such growth is that an effective nucleus must differ substantially in orientation (10-15°) from the strained crystal into which it grows.

Cahn (1966, 1971) has developed this mechanism, shown schematically in fig. 1.17. A small region of high dislocation density, and therefore high strain gradient and high local misorientation, turns into a strain-free cell by a process of dislocation rearrangement and climb. Initial growth of the subgrain is mainly by sweeping up dislocations in its path i.e. dislocations are absorbed into the boundary so that the dislocation density, and hence energy and misorientation of the interface, increase. The driving force for this process (Cahn 1971) is the difference in energy between the dislocations in the interface and the isolated dislocations or low angle boundaries which have been consumed. As the misorientation of the interface continues to increase, the individual dislocations in the sub-boundary begin to lose their character and thus the sub-boundary becomes a conventional boundary. Growth then proceeds by

destroying dislocations rather than by their incorporation into the interface. This change represents a successful nucleation event and the rate of stored energy release and the movement of the boundary rapidly increase.

Experiments by Li, Edwards, Parker and Washburn (1953) and Bainbridge, Li and Edwards (1954) have shown that low angle tilt boundaries (less than 1^{o}) are mobile but that their mobility decreases as the misorientation increases. Similarly, Cottrell (1953) quotes considerable evidence in support of the view that small angle boundaries containing more than one Burgers vector have low mobility. Gjostein and Rhines (1959) have shown that the boundary energy of [100] tilt boundaries in copper reaches a maximum at 8^{o} misorientation. Viswanathan and Bauer (1973) found that both tilt and mixed character boundaries of 2^{o} and 5^{o} misorientation have mobilities several orders of magnitude less than those of higher angle boundaries. Graham and Cahn (1956) also found high mobilities in high angle boundaries, although this mobility may be orientation dependent (Aust and Rutter 1959).

Thus, the problem with this model is that it is unclear how the sub-boundary maintains its mobility during the transition stage, when it increases its misorientation without yet having acquired high angle boundary status. It is possible that a process of the kind described above may only occur for a simple tilt boundary.

Work by Messager (1961) and Vandermeer and Gordon (1959) on aluminium and Bollman (1959) and Granzer and Haase (1961) on nickel has been interpreted as supporting this model. The clearest evidence so far is that of Ray et al. (1975) who show micrographs demonstrating subgrain growth during in-situ annealing of heavily rolled copper in

the HVEM.

2b) Subgrain Coalescence

Hu (1963) first presented evidence of this variant of subgrain growth, which was first postulated by Smith (1948), in silicon-iron crystals. Hu's subgrain coalescence model is shown schematically in fig. 1.18 where a subgrain merges with its neighbour, not by sub-boundary motion, but by rotation of one of the subgrains until its lattice is parallel to that of its neighbour.

Li (1962) has shown that it is both thermodynamically and kinetically feasible for a subgrain to rotate spontaneously in a direction such that low angle boundaries decrease their angle of misfit whilst high angle boundaries increase their angle of misfit. This leads to both an increase in boundary angle and subgrain size, both being conditions favourable to the formation of a recrystallization nucleus. Li's model of subgrain coalescence is shown schematically in fig. 1.19. This model requires dislocation movement or diffusion along the disintegrating boundary towards BD and/or IG. The mechanism also involves a small amount of sub-boundary migration at C and H. The later stages of this model are the same as for nuclei formed by subgrain growth.

Walter and Koch (1963) in an electron microscopic study of silicon-iron crystals interpreted both their own and Hu's (1963) work in terms of subgrain growth, whilst Hu interpreted both in terms of subgrain coalescence. However, evidence from contrast effects across sub-boundaries is not always unambiguously interpretable.

Subgrain growth rates reported by Beck et al. (1959) in aluminium were in good agreement with Li's model. However, Smith and Dillamore

(1970), using high purity iron, and Vandermeer and Snyder (1977), using tantalum, found sub-grain growth rates much faster (up to $\times 10^5$) than predicted by Li's theory. Kreisler and Doherty (1978) found subgrain growth rates in aluminium which were compatible with both subgrain coalescence and sub-boundary migration.

Most electron microscopic evidence for this model is not conclusive and micrographs showing fragmentation of low angle boundaries are often attributed to thin foil relaxation effects. However, some particularly beautiful electron micrographs by Jones, Ralph and Hansen (1979) showing dislocations moving along a sub-boundary towards a high angle boundary, thus leading to the elimination of the sub-boundary, support this model.

3) Strain Induced Boundary Migration (SIBM)

This mechanism was first noted by Beck and Sperry (1950) in high purity aluminium. It is shown schematically in fig. 1.20. A bulge forms in the high angle grain boundary between grains A and B and grows into grain B, which has a finer subgrain structure and a higher dislocation density. The driving force is the difference in stored energy between the two grains. It is not a true nucleation process in the sense that a high angle boundary does not form but already exists and has only to migrate.

The mechanism has been confirmed electron-microscopically by Bailey and Hirsch (1962) in copper and silver. They formulated the following criterion for a bulge to grow:-

$$\Delta E - \frac{2\gamma \sin\alpha}{L} > 0 \qquad (1.12)$$

where ΔE is the strain energy per unit volume between the two grains, γ is the boundary energy and α and L are defined by fig. 1.21.

Further evidence for this mechanism is clearly seen in work by Bellier and Doherty (1977) in aluminium and Doherty and Martin (1962/1963) in aluminium-copper alloys.

Other fundamental mechanisms have been proposed besides those presented above e.g. Neilson's `Geometric Coalescence' and Burgers' and Verbraak's `Martensitic Nucleation' model, but are considered unlikely or have little supporting evidence.

1.4.4 Nucleation Sites

The fundamental mechanisms outlined above can occur at specific lattice discontinuities and specific mechanisms have been proposed to account for these. Some of the sites and mechanisms are outlined below:-

Transition Bands

Nucleation at transition bands was first noted by Hu (1963) in silicon-iron. Formation of nuclei was by the coalescence of subgrains within the transition band but never by growth of the outermost subgrain into the surrounding matrix. Walter and Koch (1963) also reported nucleation at transition bands in silicon-iron but stated it occurred by subgrain growth. Nucleation at transition bands has now often been found e.g. in aluminium (Bellier and Doherty, 1977), and in titanium (Schofield and Bacon, 1961). Doherty (1978) points out that all materials known to contain transition bands show preferential nucleation there on annealing.

Dillamore et al. (1972) proposed a model for nucleation at a transition band by migration of triple junctions so as to equalize surface tension c.f. grain growth. They suggest that a potential nucleus is one with a size advantage; the size advantage depending on the geometry and boundary conditions. The subgrain of length D_r, in fig. 1.22, is considered to be a potential nucleus because it has a free segment bd which can move towards ce, with ϕ being given by:-

$$\cos\phi = \frac{\sigma_r}{2\sigma_t} \tag{1.13}$$

where σ_r is the specific energy of random boundaries such as de and σ_t is the energy of boundaries such as ab and df. The configuration shown in fig. 1.22b is not stable and the condition that b and c should meet is given by

$$1 + m \geq d_t \tag{1.14}$$

which gives the condition for a subgrain to become a nucleus.

$$D_r \geq \frac{4}{3}(d_r + d_t(4\left[\frac{\sigma_t}{\sigma_r}\right]^2 - 1)^{1/2}) \tag{1.15}$$

The strain at which a band will satisfy this condition is given by the relationship between $d\phi/d\varepsilon$ and ϕ.

Shear bands and high strains

Shear bands have recently been identified as nucleation sites for recrystallization at high strains e.g. Grewen et al. (1977) and Huber and Hatherly (1979).

At some deformations (>90% rolling reduction) it seems that

individual matrix subgrains may be sufficiently misorientated (>20°) to grow into recrystallized grains without further development e.g. Ray et al. (1975) in copper, Kneynsberg et al. (1979) in silver. However Malin and Hatherly (1979b) point out that shear banding occurs at rolling reductions greater than 90% in copper and thus the misorientations reported by Ray et al. (1975) may have been due to inhomogeneous deformation.

Particle Stimulated Nucleation

Nucleation in the vicinity of large second-phase particles (>1 micron) is now well-established e.g. Leslie et al (1963), Haessner, Hornbogen and Mukherjee (1966).

This Particle Stimulated Nucleation, PSN, is associated with the lattice rotations that occur around large particles due to strain incompatibility. However, as Humphreys (1980b) points out, lattice rotations are a necessary but not sufficient condition for PSN since large lattice rotations are observed at particles one tenth of the size required for the PSN, compare figs. 1.10 and 1.23. The controlling factor seems to be the size of the 'deformation zone', which is of a similar size to the particle, over which these lattice rotations occur. The deformation zone consists of small subgrains (0.1 micron), which are largely strain and particle size independent, which grow to consume the deformation zone by sub-boundary migration. Fig. 1.24 shows the Humphreys (1980b) model for subgrain growth in the deformation zone. Three possibilities of growth occur:-

1) Fig. 1.24b shows a subgrain, A, near the particle which grows and consumes the deformation zone and rapidly produces a high angle grain boundary. This growth is favoured by a large orientation

gradient in the subgrain and thus by large particles and strains.

2) Fig. 1.24d; a matrix subgrain, B, grows into the deformation zone from its edge. This process is favoured by a large subgrain size. Growth will be slow and no high angle grain boundary forms so that this is not a viable nucleation mechanism.

3) Fig. 1.24f shows a combination of the above two processes. The most highly misorientated subgrains near the particle interface are consumed by matrix subgrains, B and C, whilst a subgrain D, in the middle of the deformation zone, grows. This may eventually lead to nucleation but with a different orientation to mechanism 1.

The condition for growth beyond the deformation zone, Humphreys (1979c) is obtained by an energy balance:-

$$d \geq \frac{4\sigma_b}{E} \qquad (1.16)$$

where d is the deformation zone diameter, σ_b the grain boundary energy per unit area and E the strain energy per unit volume. If the matrix substructure consists of subgrains of the diameter S this can be rewritten, Humphreys (1979c),

$$d \geq \frac{4\sigma_b S}{3\sigma_s} \qquad (1.17)$$

where σ_s is the sub-boundary energy.

Kamma and Hornbogen (1976) have suggested that PSN may be further enhanced if the particles are surrounded by a precipitate free zone.

Grain Boundaries

It is frequently observed that smaller cell sizes and higher dislocation densities occur near grain boundaries e.g. Hutchinson (1974). This is because of the geometrically necessary dislocations required to satisfy the continuity requirements at the grain boundary.

Doherty and Cahn (1972) suggested that subgrain coalescence could occur preferentially at grain boundaries. Jones, Ralph and Hansen (1979) found that SIBM did not occur often at grain boundaries in the aluminium-alumina they studied. However, nucleation occurred by coalescence of subgrains at the grain boundary. They drew schematic diagrams indicating two models for this process; fig. 1.25.

Faivre and Doherty (1979) reported that nucleation, via a subgrain coalescence process, occurred only at transition bands and transition band/grain boundary junctions.

Hansen and Bay (1979, 1981) found nucleation occurred at grain boundaries and transition bands in commercial purity aluminium and that nucleation at such sites was enhanced by the presence of large $FeAl_3$ particles; nucleation was not observed to occur at $FeAl_3$ particles which were not at these sites.

Twins have also been reported to act as nucleation sites; this has been reviewed by Cahn (1964) who likened twin/matrix interfaces to grain boundaries.

Thus it appears that nucleation can occur at all large lattice discontinuities and combinations of discontinuities. Hence, nucleation will normally occur at lattice discontinuities and in the absence of discontinuities such as in deformed $(110)[1\bar{1}2]$ F.C.C. single crystals recrystallization is extremely slow, e.g. Brown and Hatherly (1970a, 1970b) in copper and Heller et al. (1981) in aluminium.

1.5 The Effect of Solute Atoms on Recrystallization

Most work has shown that recrystallization is retarded by the presence of solute atoms e.g. Phillips and Phillips (1952) found that recrystallization of 99.99% pure copper was retarded by additions of phosphorus, silver, arsenic and cadmium; Blade, Clare and Lamb (1959), Bonisonni and Pagnelli (1965) and Lücke and Detert (1957) observed the rise of recrystallization temperature of aluminium with the addition of solute impurities; and Abrahamson (1962) observed retarded recrystallization in nickel after the addition of small quantities of transition metals. Table 1.3 by Dimitrov (1965) compares the temperature required to recrystallize commercially pure metals with zone-refined metals, in a given time.

Table 1.3 After Dimitrov (1965)

Element	Commercially pure metal (°C)	Zone refined metal (°C)
Aluminium	200	-50
Copper	180	80
Iron	480	300
Nickel	600	300
Zirconium	450	170

The solute atoms can affect the dislocation structure of the deformed metal by hindering the formation of a cell structure, Swann (1963).

Briefly, the possible interactions of solute atoms with dislocations are due to the following

i) size differences between solute and solvent atoms

ii) electrical interaction with the dislocation's electrical dipole

iii) differences in elastic moduli

iv) chemical interactions i.e. Suzuki locking

Although nucleation and growth rates are both influenced by solute atoms most experimental evidence suggests that their effect on the growth rate is the greater, thus most work has concentrated on this area.

Experiments by Aust and Rutter (1959) on boundary migration in zone-refined lead single crystals doped with tin, see fig. 1.26, produced two important conclusions

i) very small amounts of solute will dramatically retard boundary migration, the retardation increasing with solute content

ii) Kronberg-Wilson or other 'special' orientation boundaries migrate much more rapidly than random boundaries, but only if impurities are present.

However, Aust and Rutter (1960) did not find any difference between random and special boundaries when performing similar experiments with gold and silver impurities in lead.

Lücke and Detert (1957) first presented a theoretical model to try to account for the influence of solute atoms on grain boundaries. They assumed that solute atoms have a lower energy in the neighbourhood of a grain boundary and so form an atmosphere there: they reached the following conclusions

i) At high solute concentrations and low driving forces boundary migration would be controlled by the diffusion of a solute atmosphere

ii) As the concentration decreases migration rates increase until the

boundary can break away from the impurities when a large increase in migration rate would be expected

iii) At very low concentrations the migration rate should be concentration independent and equal to that of the pure metal.

The agreement between this theory and the results of Aust and Rutter (1959, 1960) was poor and other refined versions of the theory have been presented e.g. Cahn (1962) and Lücke and Stuwe (1963) and these are reviewed by Cotterill and Mould (1976). None of the theories so far presented completely explains the experimental data.

The experiments of Aust and Rutter followed the migration of striations left in lead single crystals after crystal growth. The driving force for the migration of such boundaries is extremely small. The work of Aust and Rutter, particularly the more rapid migration of 'special' boundaries, is often quoted in explanations of recrystallization behaviour. Their work may not be applicable since the driving forces involved in primary recrystallization are several orders of magnitude greater and the orientation dependence of boundary migration rate as a function of driving force is not known.

Cotterill and Mould (1976) quote several workers who have 'found' that solutes can accelerate recrystallization but state that in all cases the formation of a second phase was a strong possibility. An impurity may have a much larger influence on primary recrystallization if it is present as a solute rather than as a precipitate. Examples of this can be seen in the work of Richards and Pugh (1959) and Williams and Eborall (1953) on duralumin and Montariol (1963) on zone-refined aluminium doped with small amounts of iron, where ageing treatments reduced the amount of solute in the matrix and thus reduced the retardation of recrystallization.

However, recent work by Haessner, Hoschek and Tölg (1979) revealed that small additions of gold or palladium to silver and nickel to copper, led to an increase in the stored energy of deformation and a decrease in the recrystallization temperature of the metal. Fig. 1.27 shows the variation of stored energy and recrystallization temperature as functions of nickel content in copper. The precipitation of a second phase in this case was ruled out, since the matrix metal was of high purity and the alloying elements were completely soluble in the matrix.

In general, however, the addition of solute elements leads to a retardation of recrystallization.

1.6 The Effects of a Second Phase on Recrystallization

The effect of a second phase on recrystallization can be conveniently divided into two groups; 1) alloys in which the two phases are present in similar proportions and 2) alloys containing a discrete dispersion of second-phase particles.

1.6.1 Recrystallization of Coarse Two-Phase Alloys

Little work has been carried out on the recrystallization of coarse two-phase alloys. However, two early works produced a plethora of effects.

The recrystallization of α/β brass was studied by Honeycombe and Boas (1948) using optical microscopy and X-ray methods. During plastic deformation the α-phase deforms plastically before the β-phase and so suffers more strain. They found that recrystallization in the α-phase tended to nucleate randomly whilst in the β-phase tended to nucleate

discontinuously at grain boundaries. The β-phase tended to recrystallize more rapidly as its proportion decreased. Which of the two phases starts to nucleate first depends on the heat treatment prior to deformation. Clarebrough (1950) carried out similar work on a silver-magnesium alloy in which the amount of the β-phase was varied. He found that recrystallization of the α-phase occurred:-

i) at the α/β boundary at 10% β by volume

ii) away from the α/β boundary for 25% β by volume

iii) randomly at 50% β by volume.

He ascribed these results to changes in the mode of deformation with increasing volume fraction of β-phase.

Other effects may occur if annealing is not carried out at the same temperature as that at which the two-phase structure was formed; these are reviewed by Hornbogen (1980).

Mader and Hornbogen (1974) annealed deformed α/β brass at its equilibrium temperature and found that the recrystallization behaviour depended upon the prior strain. Below 40% strain recrystallization of β occurs first, then α recovers and finally recrystallization in the α occurs from the α/β interface. This behaviour is thought to be typical of a two-phase alloy where one phase (α) has a low, and the other (β) has a high stacking fault energy. Thus, in β, dislocations can rearrange themselves easily and recrystallization can occur easily. At strains above 70%, the β-phase undergoes a phase transformation to α_{MD}. The two phases left are both low in stacking fault energy so that recrystallization is difficult. During annealing diffusion of copper occurs from the α to the prior β grains and diffusion of zinc occurs from the prior β to the α grains. This tends to equalise the

composition and is, of course, more complete the smaller the grain size. During subsequent recrystallization, the β-phase reprecipitates. This leads to an ultra fine grain structure.

Vasudevan, Petrovic and Roberson (1974) studied silver-nickel alloys in which both phases were ductile. They concluded that the overall recrystallization rate was related to the individual recrystallization rates on a volume fraction basis.

Clarebrough (1950) concluded that the recrystallization behaviour of an alloy containing a 'massive' second-phase depends on four factors:-

i) the proportion of the two phases

ii) the difference between the equilibrium temperature and the recrystallization temperature

iii) the elastic limits of the two phases

iv) the composition of the two phases.

The effects occurring in coarse two-phase alloys are thought to be straight-forwardly explicable with electron microscopical observations.

1.6.2 Deformable Second-Phase Particles

Alloys in which particles deform at similar rates to the matrix have not been greatly studied. However, most observations have found that recrystallizaton in such systems is retarded.

Phillips (1966) using a copper-cobalt alloy found that both coherent and incoherent precipitates were sheared into lamellae during deformation. The smallest precipitates, 5.5-18nm, remained coherent whilst the larger coherent precipitates, 18-25nm, became incoherent

during deformation.

The coherent precipitates were found to break up and spheroidise on annealing above 600°C. They found a poorly developed cell structure in both aged and solution-treated alloys. The particles led to retardation of both recovery and recrystallization. Tanner and Sevri (1966), also using copper-cobalt, found similar results and in addition discovered inhomogeneous regions or `deformation bands'.

Phillips (1967) noted that γ' Ni_3Al precipitates (6-50nm) in a Ni-12.7%Al alloy were sheared into lamellae during deformation but that they remained coherent. However, in this case the precipitates had no effect on either the hardness or the recrystallization kinetics, as these were controlled by the large amount of aluminium in solution.

Kamma and Hornbogen (1976) have found that even hard carbides in a hypo-eutectoid steel were sheared at high strains if they were small enough. The cutting of precipitates led to local strain inhomogeneities in the form of `deformation bands'. This led to an increase in recrystallization rate compared to an alloy containing a similar volume fraction of larger particles. At higher strains ($\varepsilon >$ 80%) the deformation bands broadened and the strain became more homogeneous so that the small particle size alloy recrystallized slower than the large particle size alloy.

Apart from the work of Kamma and Hornbogen (1976) most work has found retarded recrystallization. This is probably due to the inhibition of cell structure formation and the reprecipitation of mechanically dissolved precipitate which occurs preferentially on dislocations; thus impeding nucleation.

Gas bubbles in a metal can also be regarded as a deformable

second-phase. These have been found by Ells and Evans (1963) in aluminium; Middleton et al. (1949-50) in platinum and Welsch, Young and Hehemann (1979) in tungsten to retard recrystallization. It appears that it is growth that is retarded by boundary pinning.

1.6.3 Undeformable Second-Phase Particles

In the above systems precipitation, dissolution, or a combination of the two, sometimes occurred. For a detailed review of the interaction between precipitation and recrystallization including the 'extra' driving force due to precipitation at the recrystallizing interface the reader is referred to Hornbogen and Köster (1978).

The survey below concerns only systems in which the particles are essentially stable; although coarsening must, of course, occur in an ageing precipitate during long anneals.

Large Particles: Acceleration of Recrystallization

The mechanism of Particle Stimulated Nucleation which occurs around large particles has been explained in section 1.3.4. Gladman, McIvor and Pickering (1971), using electron microscopy, found preferential recrystallization at large spheroidised carbides (0.5-10 microns) in ferrite. The smallest particle size at which PSN can occur is not known but it cannot be smaller than that at which lattice rotations occur i.e. ~ 0.2microns. Humphreys (1977) has investigated the relationship between particle size and the deformation at which PSN will occur. He found that PSN can occur at smaller particles as deformation increases, see fig. 1.23.

In all the systems quoted above and in section 1.3.4, the large particles were widely spaced. If the spacing of the particles is

decreased the nucleation rate must, initially, increase. Additionally, Porter and Humphreys (1979) have found that closely spaced, sub-critical particles may lead to PSN by forming a joint deformation zone. However, if the interparticle spacing is very small, the particles may mutually interfere with each other's nucleation processes and recrystallization occurs such that the final grain size is of the order of the interparticle spacing. This has been observed in aluminium alloys by Morris (1976).

Recently, Sandström (1980) has attempted to produce a semi-empirical model for PSN.

Other factors which have not yet been investigated are the effects of particle strength and shape and the effect of the strength and diffusivity of the particle-matrix interface.

Alloys Containing Fine Second-Phase Dispersions

In many works it is difficult to separate the effects of solute atoms from particles but the following were thought to be only particle effects.

i) Retardation of recrystallization

Retardation of recrystallization by closely-spaced small second-phase particles was first reported by Van Arkel and Burgers (1930). They noticed a slower rate of X-ray line sharpening during annealing for deformed tungsten containing thoria than for pure tungsten. Meijering and Druyvesteyn (1947) found that in internally oxidised copper alloys, the central oxide-free regions recrystallized readily, whilst the outer oxide-containing region resisted recrystallization up to close to the melting point of the metal. Alumina particles have been found to retard recrystallization in

internally oxidised alloys of copper, Wood (1959) and silver, Gatti and Fullman (1959).

Much work has now been done demonstrating retardation including a great deal of work on sintered compacts and extruded alloys. Preston and Grant (1961) found that extruded copper-alumina and copper-silica alloys resisted recrystallization almost to the melting point of copper, see fig. 1.28. Inman, Zwilsky and Boone (1964) reported a similar retardation in thoria-dispersed nickel. Westerman and Lenel (1960), Nobili and De Maria (1965) and Hansen and Bay (1972) have all reported that SAP is very resistant to recrystallization. Fig. 1.29 shows a graph of hardness vs. temperature for 1hr. isochronal anneals obtained by the author for SAP containing 7wt% alumina. Recrystallization was resisted up to the melting point.

Hansen and Bay (1972) using SAP containing 0.6 and 1.2wt% alumina found that the resistance to recrystallization increased as the oxide content increased and that it depended on the way in which the particles were arranged. For the 0.6wt% alumina alloy, the amount of retardation decreased as the deformation was increased.

The retardation of recrystallization has been ascribed to pinning of the sub-boundaries by particles (Doherty and Martin, 1962/1963).

Widely spaced small particles appear to have little influence on recrystallization; Hansen (1975) and Doherty (1980) quote evidence to support this view.

ii) Acceleration

The acceleration of recrystallization by particles too small to produce PSN was first reported by Martin (1957) using internally oxidised copper-silica. He found that the acceleration was greatest

for the largest volume fraction and coarsest particles. Haessner, Hoschek and Tölg (1979) have, similarly, found a lower recrystallization temperature for (110)[1$\bar{1}$2] copper single crystals containing alumina particles than for copper.

iii) Retardation and Acceleration

Doherty and Martin (1962/1963) using both polycrystalline and monocrystalline two-phase aluminium-copper alloys containing θ-$CuAl_2$ first showed that both acceleration and retardation of recrystallization can occur in the same system. They concluded that nucleation was the rate controlling step and that the recrystallization rate was dependent on the interparticle spacing (1-4 microns) and not the particle size (0.5-2 microns) or volume fraction of particles. The work of Doherty and Martin (1962/1963) suffered from the drawback of using an age-hardening system so that at long annealing times the precipitate coarsened making the interpretation of results difficult. The particles were also quite large and the acceleration of recrystallization by PSN is not ruled out.

Hansen (1975) drew a graph, fig. 1.30, showing the relationship between the recrystallization temperature and interparticle spacing for two sets of particles and thus suggested that particles smaller than 100nm cannot produce accelerated recrystallization. This, however, is not supported by the experimental evidence.

Three works have demonstrated that both acceleration and retardation of recrystallization can occur in a system in which the particles are too small to produce PSN; these are the internally oxidised alloys of copper-silica, Humphreys and Martin (1966) and copper-alumina, Chopra and Neissen (1974) and Baker and Martin (1980).

No mechanisms have been demonstrated in these alloys but the retardation has been ascribed to slip homogenization rather than sub-boundary pinning. The acceleration has simply been put down to an increase in the stored energy, due to the geometrically necessary dislocations required, although this has not been measured. Humphreys and Martin (1966) found that the grain size of both retarded and accelerated alloys were the same as those of pure copper suggesting that both nucleation and growth are affected to the same extent. Baker and Martin (1980) found that the grain size decreased as recrystallization was more rapid suggesting that nucleation was the important step, in agreement with Doherty and Martin (1962/63). Chopra and Neissen (1974) measured nucleation rates using X-ray techniques and also concluded that nucleation was the rate controlling step.

The effects of varying the particle size, interparticle spacing and degree of deformation have been investigated in the above alloys.

Interparticle spacing

Humphreys and Martin (1966), using internally oxidised copper-silica containing particles of 50 - 200nm diameter and 0.5 - 1 micron interparticle spacing, found that the recrystallization rate was determined chiefly by the interparticle spacing, the recrystallization rate increasing as the interparticle spacing increased, see fig. 1.31. Baker and Martin (1980) using single crystals of copper-alumina also found that for a given particle size, recrystallization was more rapid for a larger interparticle spacing.

Particle Size

Baker and Martin (1980) found a change from retarded to accelerated recrystallization as the particle size was increased for a

constant interparticle spacing.

Strain

Chopra and Neissen (1974) found a changeover from retarded to accelerated recrystallization as the rolling deformation was increased from 50% to 70%. However, their results are complicated by the use of polycrystals which on internal oxidation can lead to films of oxide along the grain boundaries as well as discrete particles inside the grains; e.g. Komatsu and Grant (1962) also found that internal oxidation of a copper-1.59%silicon alloy led to a much greater density of particles near the boundary and that particles could form preferentially on sub-boundaries and crystal defects. The effect of this film on recrystallization is not known. Also the loss of aluminium to the grain boundaries is not taken into account in their analysis of the particle sizes and spacings.

1.7 The Object of the Present Work

The micromechanisms involved in Particle Stimulated Nucleation have been clarified by Humphreys (1977). However, the micromechanisms of recrystallization involved in systems in which the particles are too small to produce Particle Stimulated Nucleation are not understood. The present work is concerned with the effect of such small particles in a system in which both acceleration and retardation of recrystallization kinetics can occur. Previous work in such systems has demonstrated that increasing the particle size and spacing can accelerate the recrystallization rate but since the electron-microscopical observations performed were confined to the rolling plane little microstructural information was obtained (due to

cell overlap) so that the micromechanisms involved could not be determined.

The preceding review has demonstrated that in recent years a great deal of interest has concentrated on elucidating the mechanisms involved in:-

i) the production of dislocations at particles and their effect on the mechanical properties; however this has usually been at low strains at which recrystallization will not occur, and

ii) the production of microstructures at large strains in single phase materials; often as a prelude to recrystallization studies.

However, little work has been carried out on the effect of small particles on the more heavily deformed structures that will recrystallize on annealing.

In the present study, using a model system of single crystal copper-alumina, the dislocation structures formed on rolling are characterized and compared with those of the pure single phase crystals of the same orientation. The development of the deformation structure with increasing strain is studied and the recrystallization kinetics and stored energies determined at each strain observed.

The object of the present study is therefore to determine the micromechanisms which lead to either acceleration or retardation of recrystallization as the dispersion parameters or strain are varied.

Fig. 1.1

Stress-strain curves for internally oxidised copper polycrystals (after Lewis and Martin, 1963).

Fig. 1.2

The Orowan mechanism

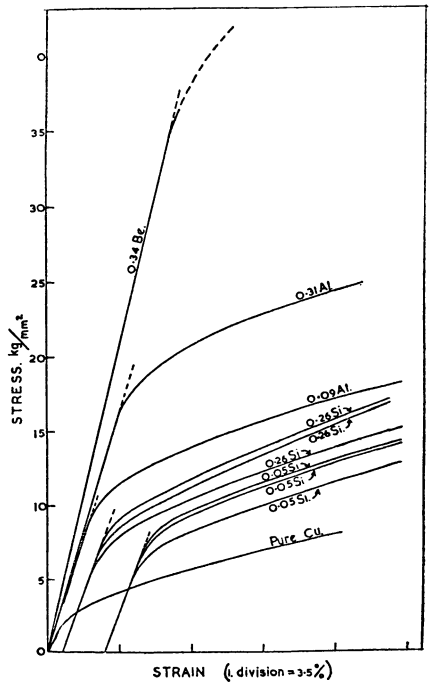
STRESS. kg/mm²
STRAIN (1 division = 3·5%)
0·34 Be
0·3 Al
0·09 Al.
0·26 Si.
0·26 Si.
0·26 Si.
0·05 Si.
0·05 Si.
0·05 Si.
0·05 Si.
Pure Cu.

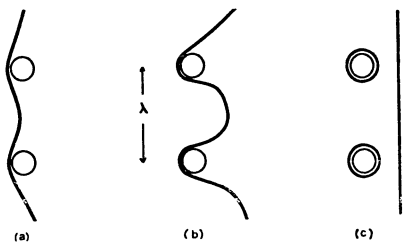
λ
(a)
(b)
(c)

Fig. 1.3

Shear stress-shear strain curves of specimens containing different volume fractions of SiO_2 particles, of diameter about 90nm. Curve 1. Pure unoxidised copper. f=0. Curve 2. Pure copper, oxidised and deoxidised. f=0. Curve 3. $f=0.33\times10^{-3}$. Curve 4. $f=0.66\times10^{-3}$. Curve 5. $f=1.0\times10^{-3}$. Arrows mark τ_{III} for pure copper, τ_y for particle-containing copper. (After Ebeling and Ashby, 1966).

Fig. 1.4

Plot of critical shear stress against reciprocal interparticle spacing. (After Lewis and Martin, 1963).

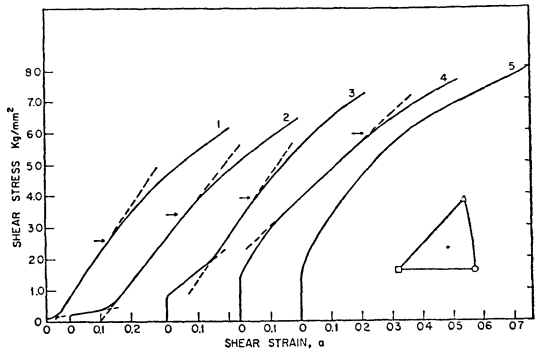
SHEAR STRESS Kg/mm²
SHEAR STRAIN, α
1
2
3
4
5

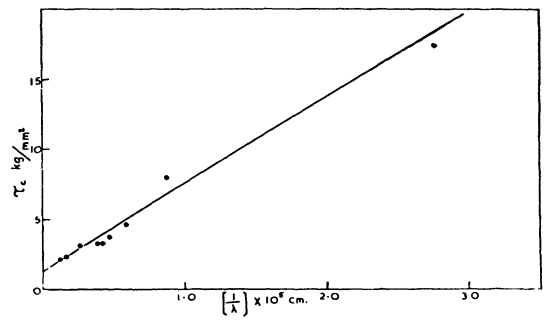
τc kg/mm²
(1/λ) X 10⁵ cm.

Fig. 1.5

Arrangement of Orowan loops around particles

a) concentric arrays are expected around particles smaller than the slip line spacing

b) whereas for larger particles a more uniform distribution of loops will form.

Fig. 1.6

Removal of Orowan loops by conservative climb.

(a)
(b)

Fig. 1.7

Plastic relaxation around particles.

a) particle in matrix; b) particle deformed by shear on primary slip plane; (c-f) relaxation mechanisms if particle does not conform to this shear will be by transfer of material from A to B: e) & f) local transfer of material; c) & d) transfer of material to or from regions remote from the particle (After Humphreys, 1980a).

Fig. 1.8

Plastic relaxation by the formation of primary prismatic loops.

a) Interstitial and vacancy loops

b) Interstitial loops and voids

Plastic relaxation by the formation of secondary prismatic loops.

c) Interstitial and vacancy loops

d) Interstitial loops and voids.

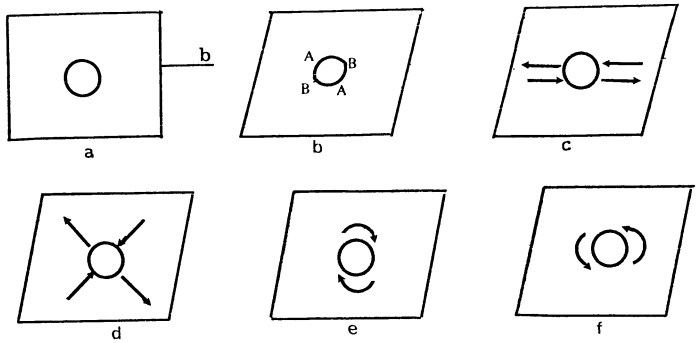
b
A
B
B
A
a
b
c
d
e
f

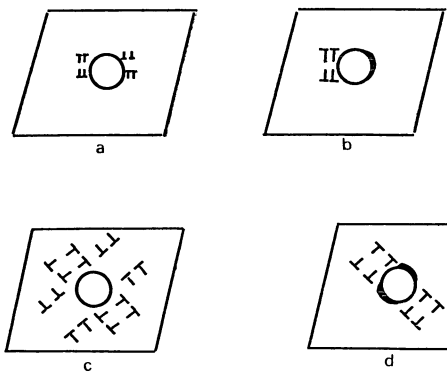
a
b
c
d

Fig. 1.9

Secondary shear loops generated at a particle (after Humphreys and Stewart, 1972).

Fig. 1.10

The magnitude of lattice rotations (α) at SiO_2 particles in copper (γ=0.38). (After Humphreys, 1977).

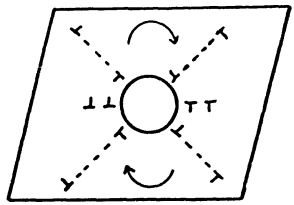

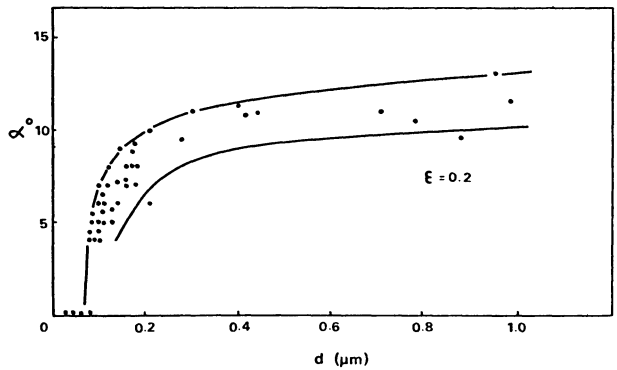
15
10
5
0
α°
0.2
0.4
0.6
0.8
1.0
d (μm)
ε = 0.2

Fig. 1.11

The lattice misorientations (α) at Si particles in Al crystals as a function of strain for particles greater than 1 micron. (After Humphreys, 1979a).

Fig. 1.12

Deformation mechanisms in Cu-SiO_2.

(After Humphreys, 1980a).

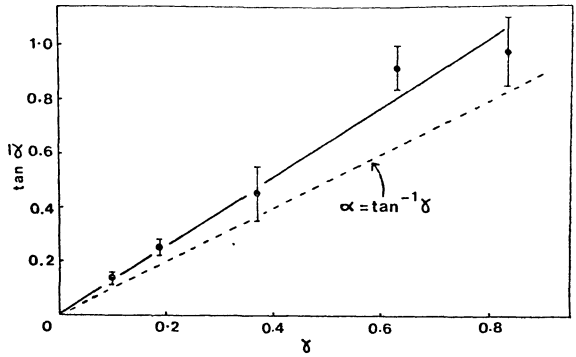
1·0
0·8
0·6
0·4
0·2
0
tan α
0·2
0·4
0·6
0·8
γ
α = tan⁻¹ γ

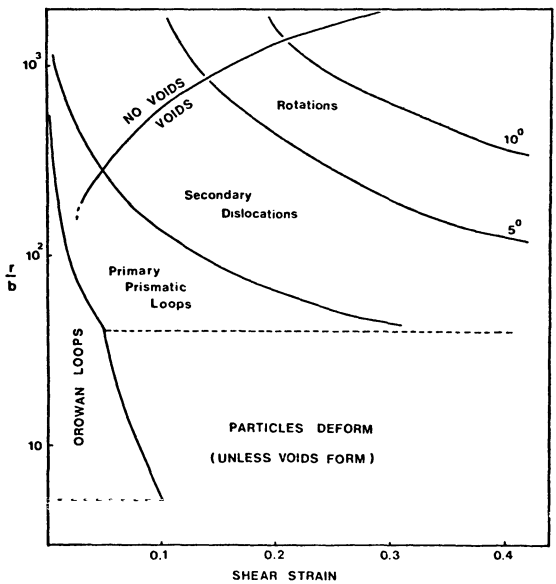
10³
10²
10
σ/τ
NO VOIDS
VOIDS
Rotations
10⁰
5⁰
Secondary
Dislocations
Primary
Prismatic
Loops
OROWAN LOOPS
PARTICLES DEFORM
(UNLESS VOIDS FORM)
0.1
0.2
0.3
0.4
SHEAR STRAIN

Fig. 1.13

Schematic representation of the deformation texture of the (001)[100] crystal. Using (001)[210] type of orientations as the ideal orientations of the deformation texture, rolling texture components can be derived by rotations of 30° around the [001] axis in both clockwise and counterclockwise directions from the initial orientation of the crystal. The resulting banded structure shows that alternate bands have the same orientation, while neighbouring bands differ in orientation by 30° and are separated by a boundary.

(After Hu, 1963)

Fig. 1.14

Comparison of experimental data with curve calculated from impingement theory for the recrystallization of aluminium; temperature=350°C, ϵ=0.051. (After Anderson and Mehl, 1945).

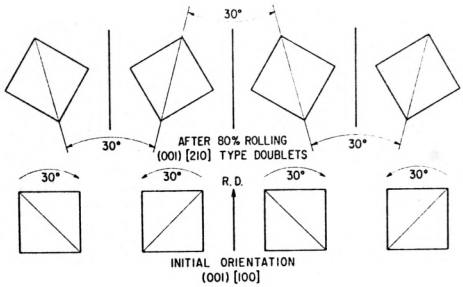
30°
30°
30°
AFTER 80% ROLLING
(001) [210] TYPE DOUBLETS
30°
30°
30°
R.D.
30°
30°
INITIAL ORIENTATION
(001) [100]

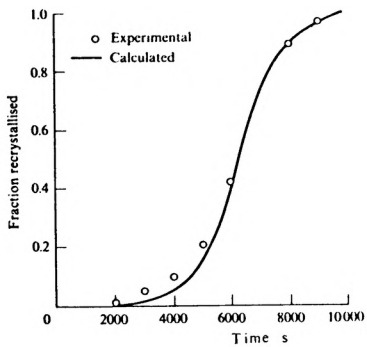
1.0
0.8
0.6
0.4
0.2
0
Fraction recrystallised
o Experimental
Calculated
2000
4000
6000
8000
10000
Time s

Fig. 1.15

Log_e $[1/(1-X_v)]$ vs annealing time plotted on a log-log scale for recrystallization in an alloy of zone-refined aluminium containing 0.0017 atomic-% copper deformed 40% by rolling at 0^oC. (After Vandermeer and Gordon, 1963).

Fig. 1.16

Schematic illustration of the overlapping of recovery and recrystallization in the rate of stored energy evolution vs. annealing time curve. (After Vandermeer and Gordon, 1963).

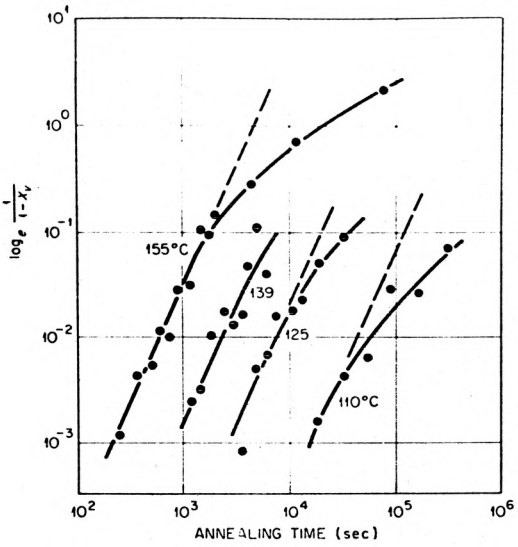
10^1
10^0
10^{-1}
10^{-2}
10^{-3}
$\log_e \frac{1}{1-X_v}$
155°C
139
125
110°C
10^2
10^3
10^4
10^5
10^6
ANNEALING TIME (sec)

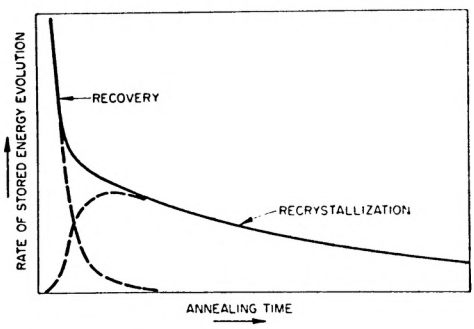
RATE OF STORED ENERGY EVOLUTION
RECOVERY
RECRYSTALLIZATION
ANNEALING TIME

Fig. 1.17

Nucleation by subgrain growth (schematic). Subgrain boundaries thickly populated by dislocations (dots) have a high misorientation angle, and are the most likely to migrate.

Fig. 1.18

Schematic representation for the formation of a recrystallized grain by the coalescence of subgrains. (After Hu, 1963).

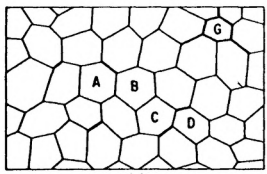

(a)

SUBGRAIN STRUCTURE BEFORE NUCLEATION.

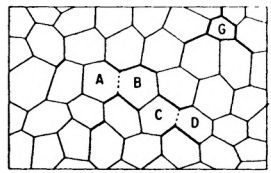

(b)

COALESCENCE OF SUBGRAINS A AND B, AND C AND D.

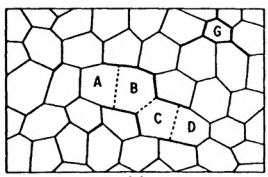

(c)

FURTHER COALESCENCE OF SUBGRAINS B AND C.

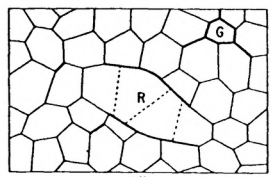

(d)

FORMATION OF A NUCLEUS WITH HIGH ANGLE BOUNDARIES.

Fig. 1.19

Schematic representation of subgrain coalescence by subgrain rotation. (a) Original subgrain structure before coalescence; (b) one subgrain is undergoing a rotation; (c) subgrain structure just after coalescence; (d) final subgrain structure after some sub-boundary migration. (After Li, 1962).

Fig. 1.20

Schematic drawing of grains A and B with their substructure (a) before, and (b) after the beginning of strain-induced boundary migration. This boundary migration is 'nucleated' by subgrain S of grain A, which is particularly large and is directly adjacent to the grain boundary.

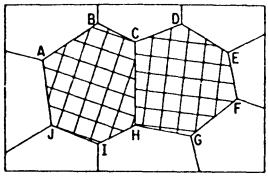

(a)

THE ORIGINAL SUBGRAIN STRUCTURE BEFORE COALESCENCE

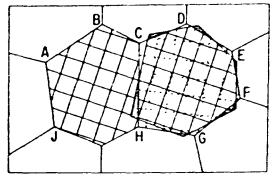

(b)

ONE SUBGRAIN IS UNDERGOING A ROTATION

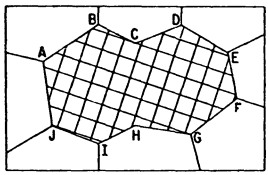

(c)

THE SUBGRAIN STRUCTURE JUST AFTER COALESCENCE

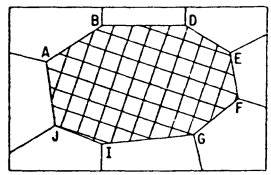

(d)

THE FINAL SUBGRAIN STRUCTURE AFTER SOME SUBBOUNDARY MIGRATION

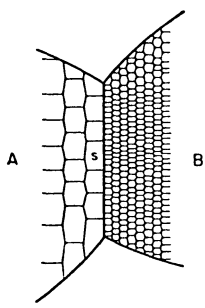

(a) BEFORE MIGRATION

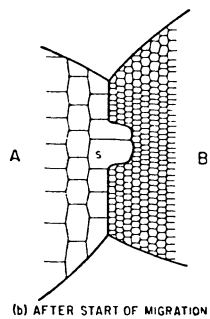

(b) AFTER START OF MIGRATION

Fig. 1.21

Bulge nucleation in SIBM.

Fig. 1.22

Schematic representation of a transition band (a) as formed, (b) relaxed on annealing, (c) detail of potential nucleus. (After Dillamore, Morris, Smith and Hutchinson, 1972).

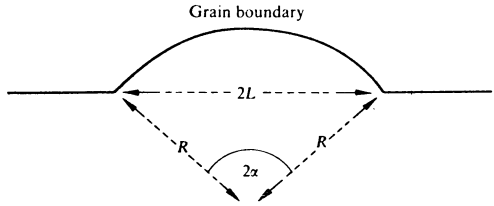
Grain boundary
2L
R
R
2α

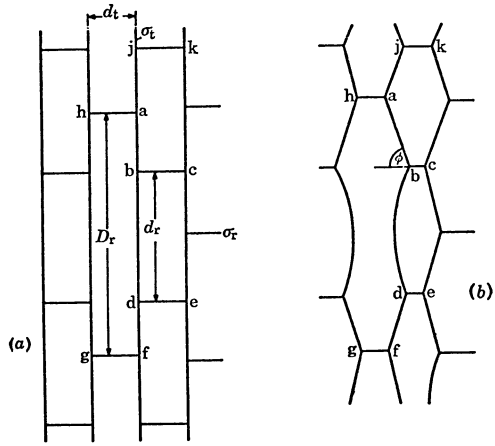
d_t
σ_t
j
k
h
a
b
c
D_r
d_r
σ_r
d
e
g
f
(a)
j
k
h
a
φ
b
c
d
e
(b)
g
f

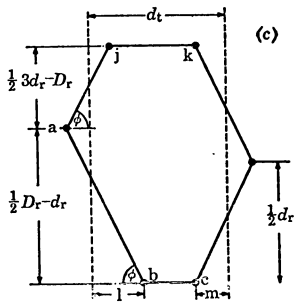
d_t
(c)
j
k
$\frac{1}{2}3d_r-D_r$
a
φ
$\frac{1}{2}D_r-d_r$
$\frac{1}{2}d_r$
φ
b
c
l
m

Fig. 1.23

The conditions of deformation and particle size for which nucleation is observed to occur at particles. (After Humphreys, 1977).

Fig. 1.24

The annealing behaviour of a deformation zone, see text for details. (After Humphreys, 1977).

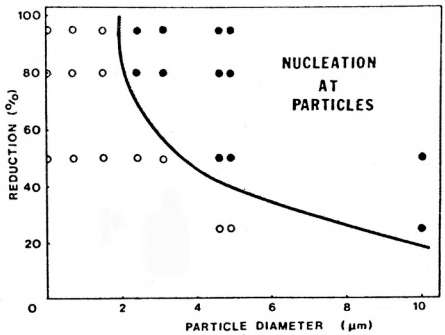
NUCLEATION
AT
PARTICLES
REDUCTION (%)
100
80
60
40
20
0
2
4
6
8
10
PARTICLE DIAMETER (μm)

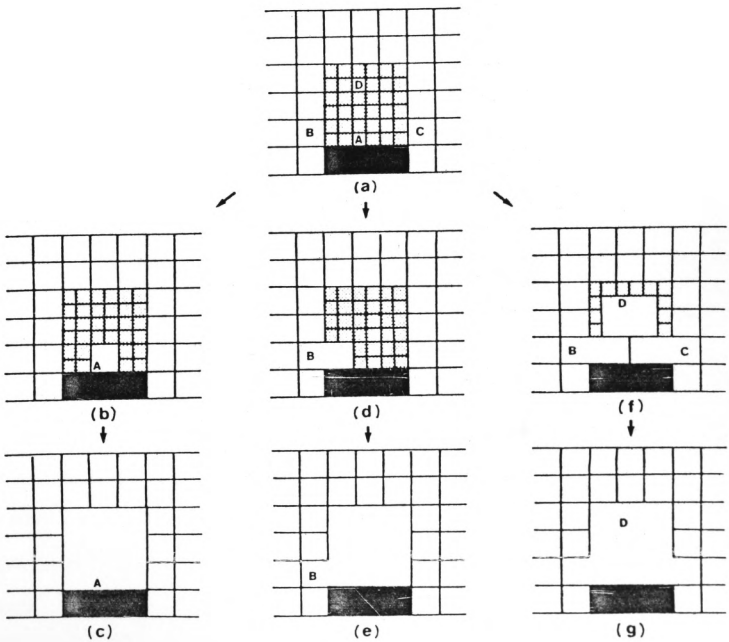
D
B
A
C
(a)
A
(b)
B
(d)
D
B
C
(f)
A
(c)
B
(e)
D
(g)

Fig. 1.25(a) Schematic diagrams illustrating the formation of a viable nucleus for recrystallization at a grain boundary by processes involving subgrain coalescence; (i) the initial recovered subgrain microstructure prior to any coalescence; (ii) illustrates a stage in the coalescence process where the sub-boundary between subgrains C and D, etc. has been partially accommodated into the high angle boundary inducing changes in the sub-boundaries between subgrains in grain 2 (e.g. F and G); (iii) at this stage large subgrains have developed on both sides of the high angle boundary; (iv) the large subgrain formed in grain 1 has grown back into its parent grain.

Fig 1.25(b) A schematic series of diagrams illustrating an alternative way to that shown in a) by which subgrain coalescence at a high angle boundary may lead to the formation of a viable nucleus for recrystallization: (i) the initial recovered microstructure in this case has the special property that alternate sub-boundaries in contact with the high angle boundary in grain 1 are of essentially opposite character; (ii) subgrain coalescence processes are largely confined to grain 1 and involve dislocation accommodation and annihilation in the high angle boundary; (iii) both the low angle and high angle segments of the interface bounding the large subgrain are assumed to have migrated; (iv) a later stage of the above process, where a nucleus is formed which 'straddles' the original position of the high angle boundary. (After Jones, Ralph and Hansen, 1979)

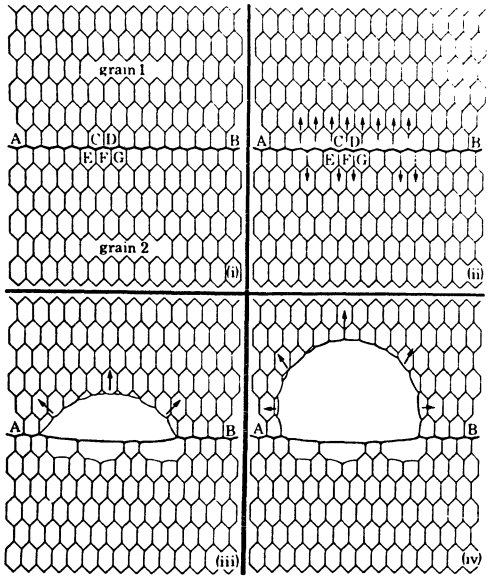
grain 1
grain 2
A
B
C
D
E
F
G
(i)
(ii)
(iii)
(iv)

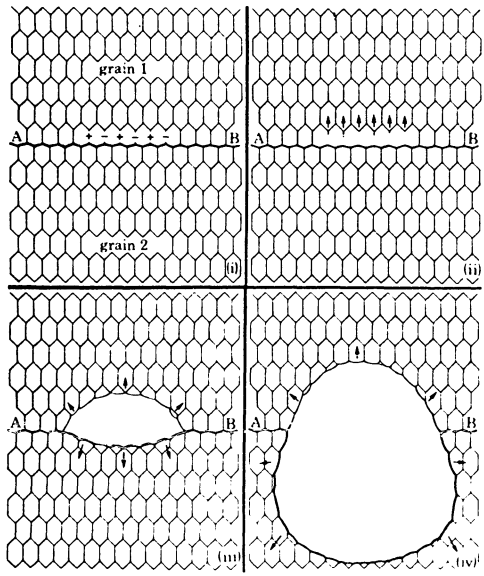
grain 1
grain 2
A
B
(i)
(ii)
(iii)
(iv)

Fig. 1.26

A comparison of rate of grain boundary migration at 300°C (logarithmic) vs wt. pct Sn for 'random' and 'special' grain boundaries. (After Aust and Rutter, 1959).

Fig. 1.27

Stored energy and recrystallization temperature of rolled Cu-Ni single crystals vs Ni concentrations (initial orientation (110)[1$\bar{1}$2], reduction of thickness 98%). (After Haessner, Hoschek and Tölg, 1979).

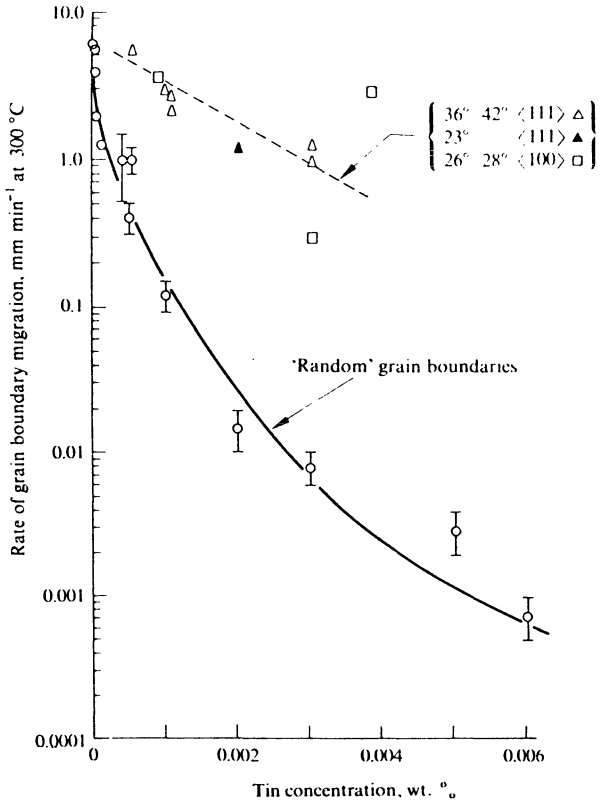
10.0
1.0
0.1
0.01
0.001
0.0001
0
0.002
0.004
0.006
Rate of grain boundary migration, mm min⁻¹ at 300 °C
Tin concentration, wt. %
36° 42° ⟨111⟩ △
23° ⟨111⟩ ▲
26° 28° ⟨100⟩ □
'Random' grain boundaries

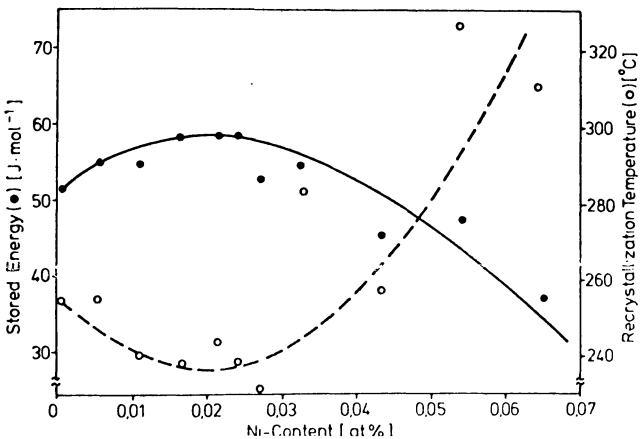
70
60
50
40
30
320
300
280
260
240
0
0,01
0,02
0,03
0,04
0,05
0,06
0,07
Stored Energy (●) [J mol⁻¹]
Recrystallization Temperature (○) [°C]
Ni-Content [at %]

Fig. 1.28

Room temperature hardness after 1 hour anneal, for copper powder alloys internally oxidised at 950°C and extruded. (After Preston and Grant, 1961).

Fig. 1.29

Recrystallization data for 50 & 75% rolled SAP 930 bar (containing 7wt% alumina). Hardness after 1 hour anneal.

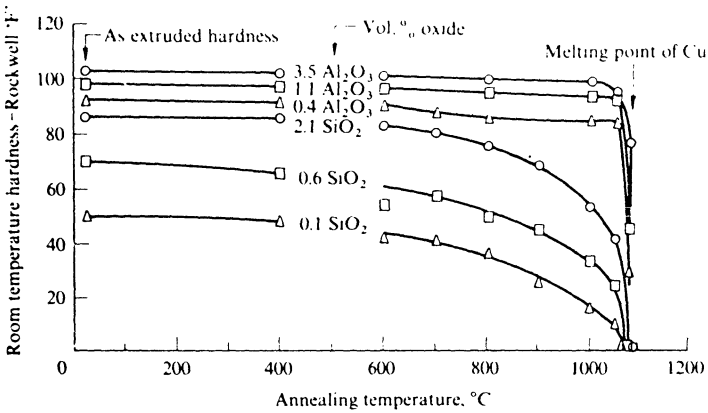
Room temperature hardness - Rockwell 'F'
As extruded hardness
Vol. % oxide
Melting point of Cu
3.5 Al_2O_3
1.1 Al_2O_3
0.4 Al_2O_3
2.1 SiO_2
0.6 SiO_2
0.1 SiO_2
120
100
80
60
40
20
0
200
400
600
800
1000
1200
Annealing temperature, °C

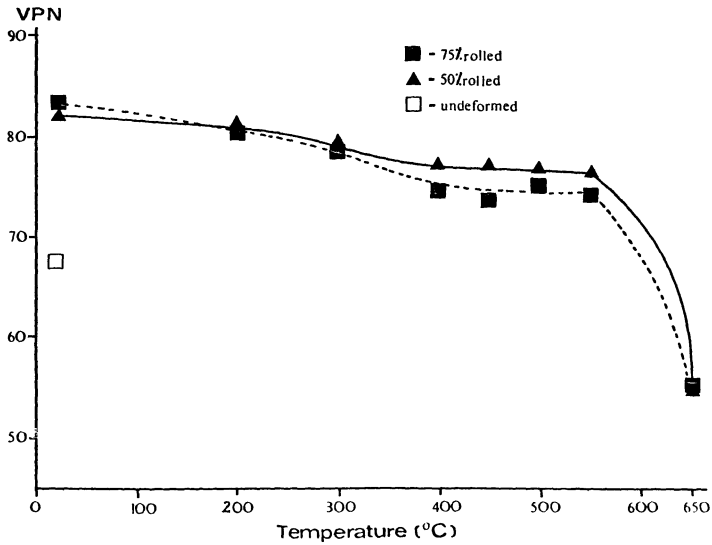
VPN
90
80
70
60
50
■ - 75% rolled
▲ - 50% rolled
□ - undeformed
0
100
200
300
400
500
600
650
Temperature (°C)

Fig. 1.30

Effect of interparticle spacing on recrystallization temperature.

(After Hansen, 1975).

Fig. 1.31

Effect of interparticle spacing on recrystallization kinetics for internally oxidised copper-silicon single crystals (After Humphreys and Martin, 1966).

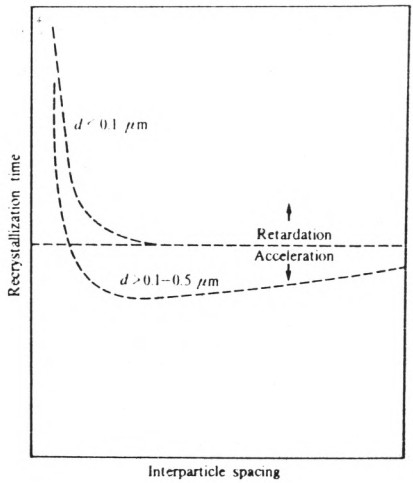
Recrystallization time
$d < 0.1\ \mu m$
Retardation
Acceleration
$d > 0.1$–$0.5\ \mu m$
Interparticle spacing

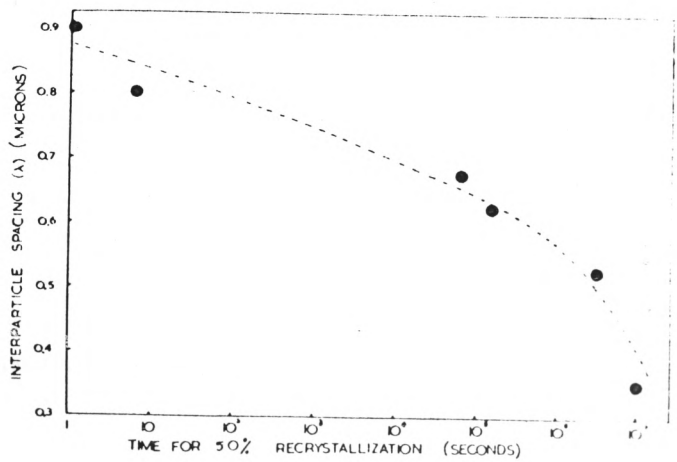
INTERPARTICLE SPACING (λ) (MICRONS)
0.9
0.8
0.7
0.6
0.5
0.4
0.3
1
10
10²
10³
10⁴
10⁵
10⁶
10⁷
TIME FOR 50% RECRYSTALLIZATION (SECONDS)

Chapter 2

Experimental Techniques and Methods

2.1 Introduction

Three alloys were used; these were the copper-based single crystals shown below:-

Alloy M	(110)[1$\bar{1}$2]	0.23wt% Aluminium
Alloy H	(111)[1$\bar{1}$0]	0.34wt% Aluminium
Alloy L	(111)[1$\bar{1}$0]	0.093wt% Aluminium

which were internally oxidised to give a high purity matrix containing alumina particles. Single crystals of pure copper of the above two orientations were produced for comparison purposes and some of them were also subjected to an internal oxidation heat treatment. This chapter describes the techniques of preparation, characterization, deformation and observation of the above materials.

2.2 Alloy Preparation

The copper-aluminium alloys used were prepared from 99.9998% Cu and 99.99% Al supplied by Messrs. Johnson Matthey & Co. Ltd. Analyses are shown in table 2.1.

Alloys were melted using either a Wild Barfield resistance vacuum melting furnace or an Inductalec induction melting furnace; both obtained vacuums better than 10^{-5} τ. In the Wild Barfield furnace

the material was melted in an alumina crucible and cast into a chill copper mould. Using the Inductalec furnace, melting was initially tried with an alumina crucible inside a graphite susceptor. However, the alumina crucible cracked frequently and acted as a heat insulator thus preventing the heat reaching the metal. Melting was successfully carried out by dispensing with the alumina crucible and melting the metal in the graphite susceptor itself, then casting into a chill copper mould. Before use the copper moulds were cleaned with 50% nitric acid.

2.3 Single Crystal Growth

Single crystals were grown in a graphite mould using a modified Bridgeman technique. The alloy was rolled into strips and spark machined to the size of the graphite mould. A diagram of the mould used is shown in fig. 2.1. All single crystals were grown from a seed of the desired orientation placed at the bottom of the mould. The single crystal growing furnace is shown diagramatically in fig. 2.2. The mould was supported on a water-cooled cold finger inside a recrystallized alumina tube which was evacuated to better than 10^{-6}τ. The counter-balanced platinum furnace was lowered at 20cm/hr to prevent thermal shock of the tube. Single crystals were grown by raising the furnace at 4cm/hr and were then checked for any 'rogue' grains by etching in 50% nitric acid.

2.4 Internal Oxidation

The grown single crystal, which was 12cm long and 2.3mm thick was sectioned as shown in fig. 2.3. The top and bottom of the crystal were removed to minimize segregation effects; the central section was retained for analysis. The orientation of the crystal was checked by X-ray back reflection Laue.

Alumina particles were produced in the remaining single crystal by internal oxidation using the method of Rhines et al. (1942). This consists of heating the specimens in a pack of equal parts of $Cu_2O/Cu/Al_2O_3$ in a static argon atmosphere. The Cu_2O/Cu mixture maintains a pressure of oxygen equal to the dissociation pressure of Cu_2O at the surface of the copper; this allows oxidation of the aluminium without the copper being oxidised. The alumina powder prevents the pack sintering to the specimen's surface. The heating was carried out in a horizontal nichrome furnace controlled to $\pm 3^{o}$ with a Eurotherm controller.

The times required for internal oxidation were determined by internally oxidising test specimens at varying times and observing the depth to which the internal oxidation front had penetrated. The internal oxidation front of a partially oxidised alloy which has been sectioned and etched in 50% nitric acid is shown in fig. 2.4. A graph of penetration depth of the internal oxidation front versus time is shown in fig. 2.5. The times used for internal oxidation were

Cu - 0.093Al : 10 hrs. @ $1000^{o}C$

Cu - 0.23Al : 15 hrs. @ $1000^{o}C$

Cu - 0.34Al : 250 hrs. @ $900^{o}C$

Internal oxidation produces a parabolic distribution of particle

sizes across the thickness of the specimen perpendicular to the internal oxidation front, with the smallest particles at the surface of the specimen. To minimize the spread of the particle size distribution, the outer one third of the crystal was removed by chemical polishing in a mixture of equal parts nitric acid, orthophosphoric acid and acetic acid.

The size and spacing of particles produced by internal oxidation can be varied by changing the solute content and the temperature. The particle size decreases as the temperature and solute are decreased.

Lewis (1963) found that the alumina particles in copper are crystalline plates lying on {111} matrix planes with the edges parallel to <110> matrix directions and obeying the following relations

$$(110)_{Cu} \;//\; (110)_{Al_2O_3}$$

$$(111)_{Cu} \;//\; (111)_{Al_2O_3}$$

He also found that particles were coherent up to 20nm, above which incoherency becomes a much more favourable state.

Humphreys (1967) found that the aspect ratio of alumina plates was 1.5:1 but Gould (1971) found a variation from 1.3:1 to 3:1 as the volume fraction increased from 1.7 to 9.45×10^{-3}. Baker (1979) found the aspect ratio increased from 2.2:1 to 3:1 as the particle size was increased in the same alloy. Thus, the aspect ratio depends on the particle size and therefore also depends on the solute content and oxidation temperature. The average aspect ratio for each alloy was approximately 3:1 in the present case.

Allain et al. (1979) have shown that alumina particles are very stable against coarsening.

2.5 Determination of Dispersion Parameters

One can, in principle, determine particle sizes in the TEM by using either thin foils or extraction replicas. There are, however, several disadvantages in using thin foils, namely:-

i) errors due to overlap, resulting in a distribution too heavily weighted towards large particles; corrections can be applied to take this into account,

ii) sectioning of the particles at the surface,

iii) uncertainty of foil thickness determination; it is sometimes difficult to determine the foil thickness to better than 15% due to thickness contour effects.

Ashby and Ebeling (1966) concluded that replicas are superior to thin foils for the following reasons:-

i) greater experimental ease

ii) simplicity of evaluation

iii) accuracy; especially when particle sizes are of the same order as the foil thickness, although replicas are poor for particle sizes less than 10nm.

For hard, inert particles in a soft matrix, mechanical polishing and etching do not section particles, they are either left in the surface or extracted whole. Ashby and Ebeling (1966) found that the extraction efficiency was independent of the particle size in copper-silica in which the silica particles were approximately 100nm in diameter.

Determination of particle sizes by extraction replicas has the advantage of not requiring all particles to be extracted, only that

all particles are extracted at the same rate. Thus particle sizes were measured directly and the interparticle spacing was found indirectly.

Specimens were mounted in resin and polished down to a 1 micron finish using SiC paper and then diamond paste. After polishing they were ultrasonically cleaned in ethanol for ten minutes then etched for twenty seconds in a straw-yellow coloured alcoholic ferric chloride solution, acidified with hydrochloric acid and followed by a wash in methanol. Carbon was evaporated onto the specimen for approximately 15 seconds from a height of 60mm in a vacuum of $10^{-5}\tau$. The replica was scored with a pin into 1.5mm squares and etched in the alcoholic ferric chloride solution. Before the replica became completely detached by etching, it was dipped in distilled water containing a small amount of ethanol. This solution caused the replica to come away from the surface and spread out; it was washed in 50% nitric acid and then in distilled water. The replica was caught on a grid and dried by touching the edge of the grid on a filter paper, care being taken not to allow the replica to touch the filter paper as otherwise it would have been drawn off.

Particles were photographed at a magnification of 55,000 times. This magnification was a compromise between obtaining a large particle size, so reducing measuring errors, and having a large number of particles on a micrograph (25-30). The largest particle dimension, x_A, was measured using a ten times magnifying scale and then placed in 9nm groups. Histograms for the three alloys are shown in fig. 2.6. These are each based on measurements of 500 particles. The histograms are approximately log-normal distributions, in agreement with results of other workers cited by Exner (1972).

In order to define an interparticle spacing, it is first

necessary to calculate an equivalent particle diameter, D_s, although this parameter has no physical meaning. D_s is given by:-

$$D_s = \frac{(3.18x_A t + 3x_A^2)}{4\pi}^{1/2}$$

where t is the plate thickness and x_A the average largest particle dimension. The planar centre-to-centre interparticle spacing λ_2, as derived by Fullman (1953) has been widely used in metallurgical investigations.

$$\lambda_2' = \left[\frac{\pi D_s^2}{6F_v}\right]^{1/2}$$

This equation takes no account, however, of the arrangement of particles. Corti, Cotterill and Fitzpatrick (1974) state that a good interparticle spacing parameter to use in deformation and recrystallization studies is Δ_3 the three-dimensional, nearest-neighbour, centre-to-centre spacing for a random array. For spherical particles this is given by

$$\Delta_3 = 0.55r\left[\frac{4\pi}{3F_v}\right]^{1/3}$$

where F_v is the volume fraction of precipitate which is found by assuming complete oxidation of all the solute. Δ_2, the analogous planar parameter is given by

$$\Delta_2 = 0.500r\left[\frac{2\pi}{3F_v}\right]^{1/2}$$

Table 2.2 shows the measured and calculated values for F_v, x_A,

D_s, Δ_2, Δ_3 and λ_2 for each of the alloys.

2.6 Deformation and Annealing

Deformation of the single crystals was carried out using a Robertson two high 5" rolling mill. Specimens were rolled down from 1.5mm thickness (the thickness after the chemical polishing of the internally oxidised specimen) by amounts of 5, 10, 18, 30, 50 and 87%. The specimens were not allowed to heat up during rolling. The end section from each specimen was discarded as these did not deform in the same way as the specimen as a whole.

Annealing was performed in a salt pot containing

either i) EFCO LTD/1 salt (range 190-580°C)

or ii) a 50:50 mixture of Li_2CO_3 and K_2CO_3 (range 500-800°C)

Before annealing the specimens the surface was etched back to remove any scratches in case these acted as nucleation sites for recrystallization.

2.7 Determination of Recrystallization Curves

Annealed specimens were mounted in resin and polished through finer grades of silicon carbide paper and diamond paste on selvyt to a 1 micron finish, then etched in freshly made 50% nitric acid. The percentage recrystallization on a plane of polish was determined by a systematic point count as outlined by Underwood (1970). This was shown to be the most accurate method for areal analysis by Hilliard and Cahn (1961). The point count was carried out using a grid placed on the projection screen of a Vickers M55 projection microscope.

2.8 TEM Specimen Preparation

Thin foils were made from the transverse, TS, and longitudinal, LS, sections and the rolling plane, RP. Most observations, however, were from the longitudinal sections of the rolled specimens. Thus, the processing to make a LS thin foil is shown schematically in fig. 2.7 and described below.

Rolled specimens were glued to a brass plate using a mixture of Durofix and graphite, a transverse section was then removed by spark machining using a wire cutter at the slowest speed. Copper was electroplated onto the transverse section until it was approximately 3.5mm in diameter. The electroplating was carried out in a solution of 200g per litre of $CuSO_4$ $5H_2O$ and 50ml per litre of H_2SO_4 with a large copper cathode at a current of 60mA closed-circuit. The solution was agitated with a magnetic stirrer.

The transverse rods were sliced into 1mm thick discs using a spark machine as before. The discs were then glued to a brass plate and 3mm discs trepanned from them. These discs were ground down to 12-thou. on 800 grade SiC paper. Thin foils were produced by a two stage process.

i) Electrojetting each side for 90 seconds using 33% H_3PO_4 at 100V, approximately 120mA half-wave rectified.

ii) Electropolishing to perforation in Struers D2, at 2V for the pure copper and 2.2V for the copper-alumina, half-wave rectified - approximately 60mA at room temperature.

After perforation, the discs were washed for 30 seconds in each of distilled water, methanol, ethanol and methanol again. They were then

dried by touching the edges onto filter paper. The specimens were observed immediately after preparation in the electron microscope. A polished disc is shown in fig. 2.8.

Previously the author had used a PTFE holder method for thin foil preparation (Part II thesis) but this was found unsuitable for these particular specimens as perforation took place preferentially along the interface between the electroplated copper and the rolled sections. Even when using the two-stage method it was not possible to prepare TEM specimens from specimens of greater than 50% reduction as perforation again occurred at this interface.

2.9 The Validity of Thin Foil Observations

Hirsch et al. (1977) reviewed two ways in which dislocation arrangements may differ in thin foils from those in the bulk material:-

i) by the introduction of dislocations during specimen preparation e.g. by spark machining or by careless handling of the foil.

and ii) by dislocation loss and rearrangement due to the relaxation of long range stresses during the thinning process.

Dislocations due to handling can usually be recognised since they are generally long and straight. Introduction of dislocations into the foil can usually be avoided with care. Hirsch et al. concluded that the best test of whether dislocations were introduced by handling is whether they are reproducible (in several foils).

On dislocation losses and rearrangement they came to the following conclusions:-

i) in low stacking fault energy materials the general character of the dislocation structure is unaffected

ii) the dislocation structure is usually unaltered except near the edge of the foil

iii) the loss of dislocations decreases with increasing deformation.

In the present work, dislocations were not seen near the edge of the foil; this was probably due to the high purity of the matrix, so that dislocations would not be pinned by solute atoms and could easily rearrange themselves. The dislocation structure was also found to change with thickness and in thinner regions was unrepresentative of the bulk. It was found that the dislocation-free areas were much larger in the copper than in the copper-alumina alloys. This would be due to particle-pinning of dislocations and the inherently greater dislocation density in the particle-hardened alloy. In specimens of the lowest deformations of copper, dislocations could only be seen near the limit of penetration of 100keV electrons; however, at higher deformations, greater than 30% rolling reduction, a representative dislocation structure could be observed in a 100keV TEM because dislocations find it difficult to slip out of the complex networks.

From the above observations it was decided that dislocation structures in lightly strained material (< 30% rolling reduction) viewed in a 100keV TEM were unrepresentative of the bulk material. Thus thin foils were normally viewed at 400keV in the HVEM.

400keV was chosen since Makin (1968) has shown that radiation damage can occur in copper above this voltage. Figs. 2.9 and 2.10 show the rotation and magnification calibrations determined at this voltage on the Oxford HVEM. They were produced by observation of a MoO_3 crystal and a calibration grid respectively at different

magnifications.

2.10 STEM Microdiffraction-Technique

STEM microdiffraction, as available on a JEM 100C with ASID unit, was used to obtain diffraction information from small areas approximately 25nm in diameter. The JEM 100C utilizes the focused probe technique where the scanning probe is stopped and a microdiffraction pattern is formed on the TEM screen. A problem with this technique is the high specimen contamination rate which leads to degradation of the diffraction patterns. Using fast film to record the microdiffraction patterns reduces this problem. The contamination spot produced by the stationary probe is useful as a marker to show from where the microdiffraction pattern was obtained.

The technique enabled misorientations to be measured between small dislocation-free regions by observation of Kikuchi line shifts and rotations. As misorientations were found to be small, it was found advisable to use a double exposure of the microdiffraction patterns from the two regions of interest on the same photographic plate. This minimized errors due to rotations and shifts of the photographic plates in their holders. A polaroid photograph of the region of interest was found to be useful for identification purposes and a permanent record of the region was taken using the instrument as a TEM. The beam divergence and probe size could be adjusted either by control of the condenser lens or by changing the specimen height. The latter method also changes the camera length greatly (by up to two and one half times). The beam divergence was also controlled by the condenser aperture. The angular extent of the pattern is limited by

the objective lens pole pieces; in the present work the width of the pattern ranged between 15 and 18°; however Kikuchi lines were not always present at the outside of the pattern due to diminution in intensity.

By using condenser aperture 3 at the lowest specimen height, the beam divergence was such that both discrete diffraction discs and Kikuchi lines were obtained; see fig. 2.12. By inserting condenser aperture 4 a spot pattern was obtained with a few Kikuchi lines in the centre; this spot pattern was used to determine the camera length for each set of Kikuchi line patterns, see fig. 2.11.

Misorientations were measured to approximately 0.1°. Fig. 2.13 shows the geometry of the STEM electron optics.

Table 2.1(a)

Analysis of copper used in this work

All concentrations are quoted in parts per million

Al < 1	Mg < 1
Ba < 1	Mn < 1
Be < 1	Mo < 1
Bi < 1	Ni < 1
B < 1	Si < 1
Cd < 1	Ag 1
Ca < 1	Na < 1
Cr < 1	Sn < 1
Co < 2	Ti < 5
Fe < 1	V < 1
Pb < 1	Zn < 3
Li < 1	

The symbol < indicates that the element was not detected, and that its concentration was therefore less than the level of detection indicated.

Table 2.1(b)

Analysis of Aluminium used in this work

Elements detected	(Parts per million)
Magnesium	10
Silicon	7
Iron	5
Copper	3
Calcium	1
Sodium	<1

Table 2.2

Alloy	F_v x10^{-3}	x_A(nm)	D_s(nm)	Δ_2(μm)	Δ_3(μm)	λ_2(μm)
L	3.9525	67	38	0.22	0.11	0.44
M	9.775	113	64	0.24	0.13	0.47
H	14.45	81	46	0.14	0.08	0.28

Fig. 2.1

Diagram of graphite mould used for growing single crystals.

Fig. 2.2

Schematic representation of the vacuum single crystal growing apparatus. The arrows indicate the water flow.

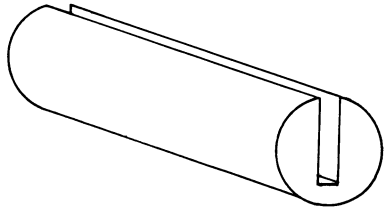

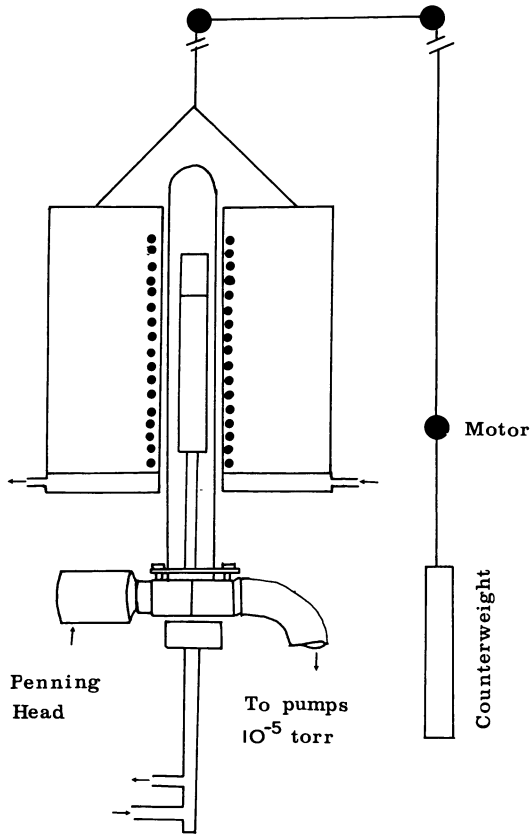
Motor
Counterweight
Penning
Head
To pumps
10^{-5} torr

Fig. 2.3

Showing sectioning of single crystal.

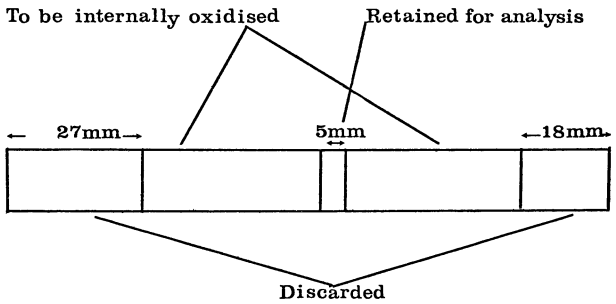
To be internally oxidised
Retained for analysis
27mm
5mm
18mm
Discarded

Fig. 2.4

Alloy H internally oxidised for 13 hours at 900°C and sectioned perpendicular to the oxidation front.

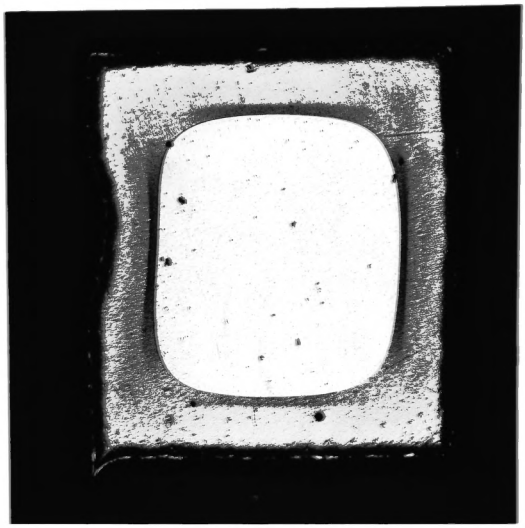

Fig. 2.5

Graph of depth of penetration of internal oxidation front against the square root of the time taken; alloys L, M and H.

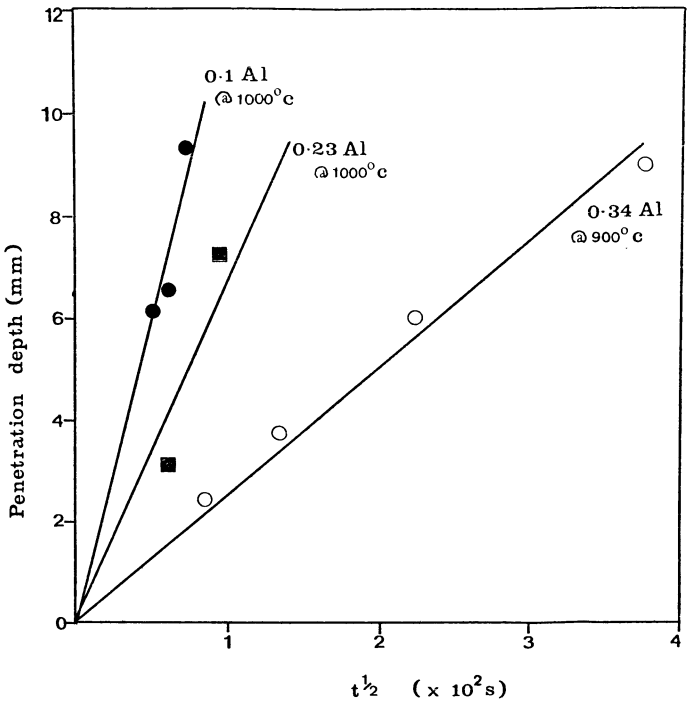
0·1 Al
@ 1000°c
0·23 Al
@ 1000°c
0·34 Al
@ 900°c
Penetration depth (mm)
$t^{1/2}$ (x 10^2s)
0
2
4
6
8
10
12
1
2
3
4

Fig. 2.6(a)

Particle size distribution. Alloy L.

Fig. 2.6(b)

Particle size distribution. Alloy M.

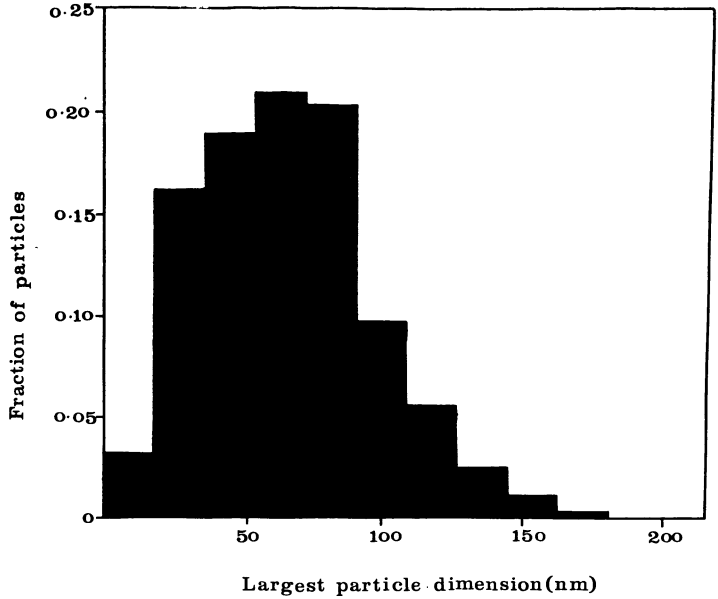
0·25
0·20
0·15
0·10
0·05
0
Fraction of particles
50
100
150
200
Largest particle dimension(nm)

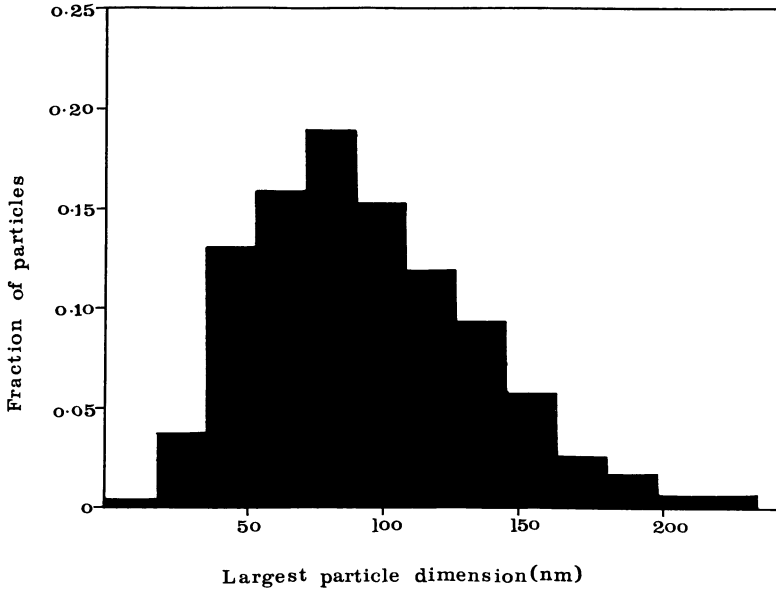
0·25
0·20
0·15
0·10
0·05
0
Fraction of particles
50
100
150
200
Largest particle dimension(nm)

Fig. 2.6(c)

Particle size distribution. Alloy H.

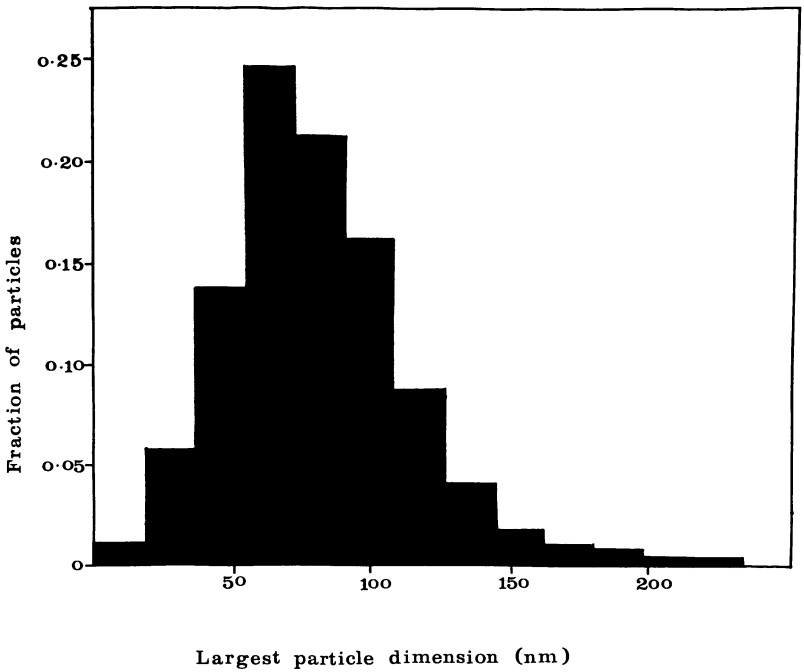
0·25
0·20
0·15
0·10
0·05
0
Fraction of particles
50
100
150
200
Largest particle dimension (nm)

Fig. 2.7

Schematic diagram showing preparation of a thin foil containing a longitudinal section:-

a) spark machine transverse slice

b) electrolytically deposit copper on transverse slice

c) section perpendicular to transverse direction

d) spark machine 3mm disc

e) dish disc by electrojetting

f) final thinning by electropolishing

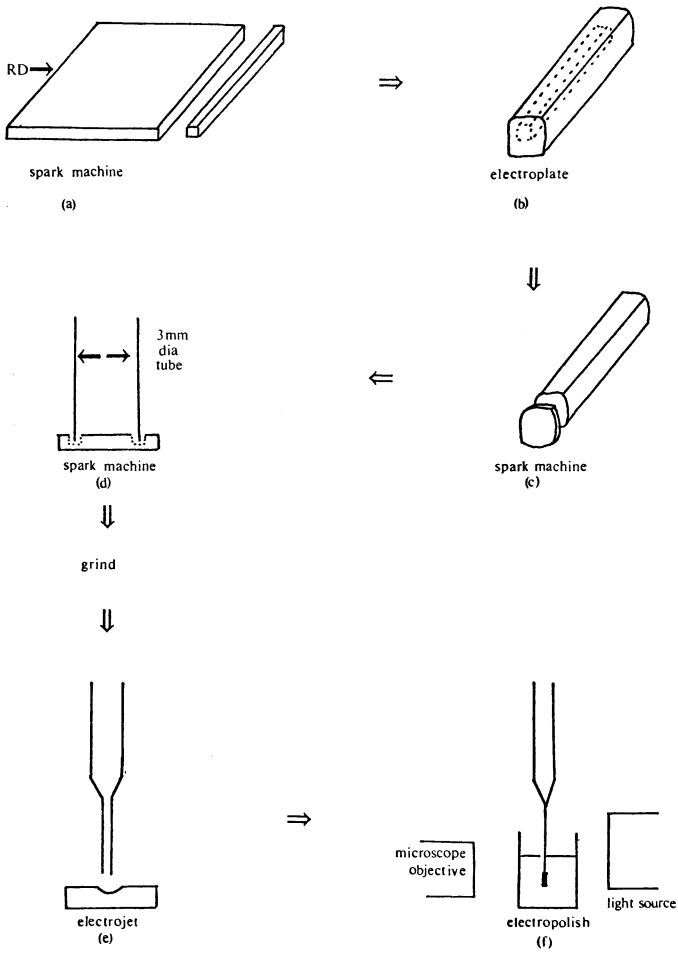
RD
spark machine
(a)
electroplate
(b)
spark machine
(c)
3mm
dia
tube
spark machine
(d)
grind
electrojet
(e)
microscope
objective
electropolish
(f)
light source

Fig. 2.8

Typical disc used to make thin foil showing rolled section surrounded by electroplated copper.

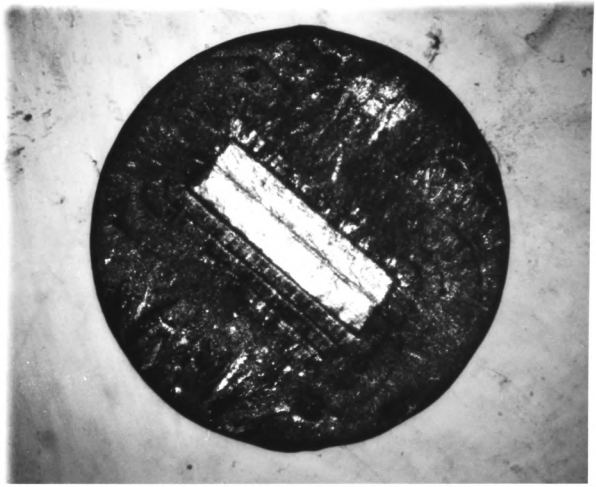

Fig. 2.9

Magnification calibration for Oxford HVEM at 400keV (side entry).

Fig. 2.10

Rotation calibration for Oxford HVEM at 400keV (side entry). Diffraction pattern is rotated 180 + x degrees anticlockwise with respect to image (for CL=63cm).

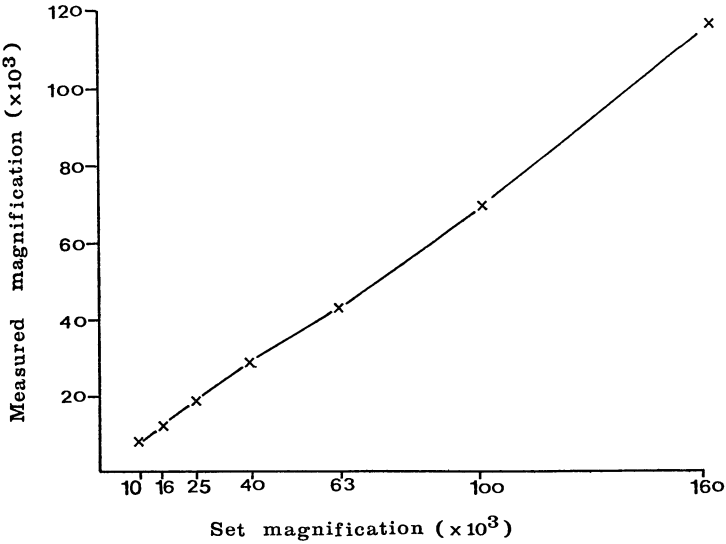
Measured magnification (×10³)
120
100
80
60
40
20
10
16
25
40
63
100
160
Set magnification (×10³)

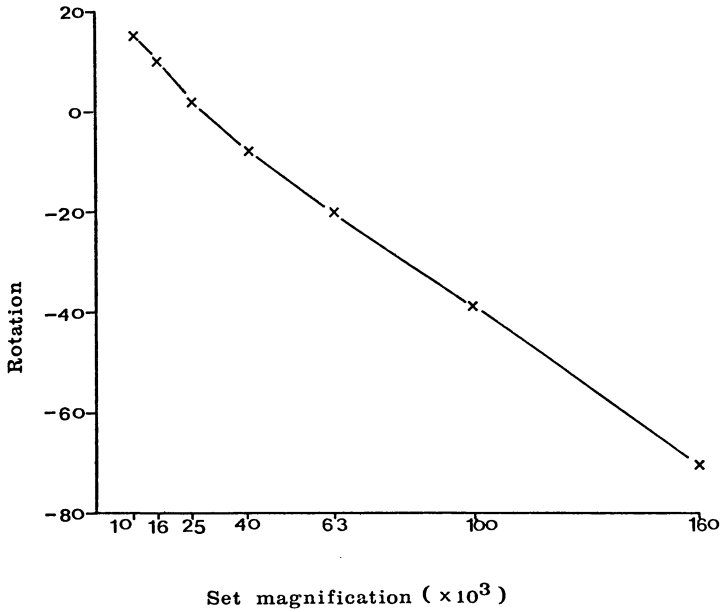
Rotation
20
0
-20
-40
-60
-80
10
16
25
40
63
100
160
Set magnification (×10³)

Fig. 2.11

Microdiffraction pattern obtained from a copper foil in 100C STEM using condenser aperture 4 and the lowest specimen height.

Fig. 2.12

Microdiffraction pattern obtained from a copper foil in a 100C STEM using condenser aperture 3 and the lowest specimen height.

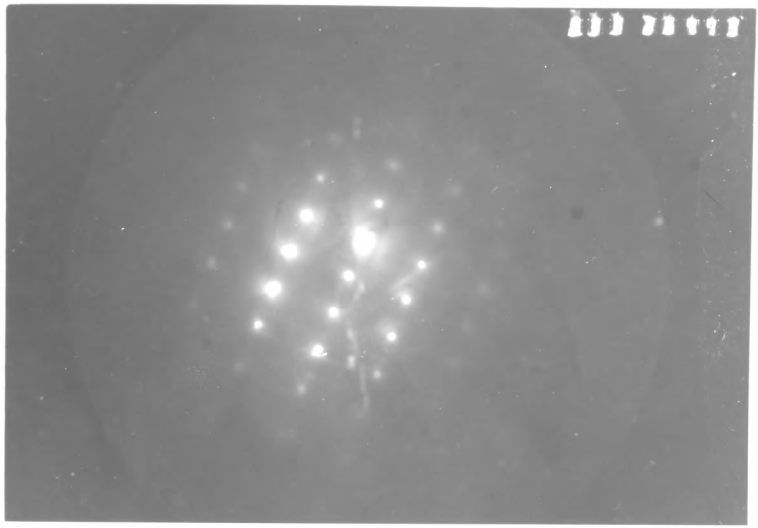

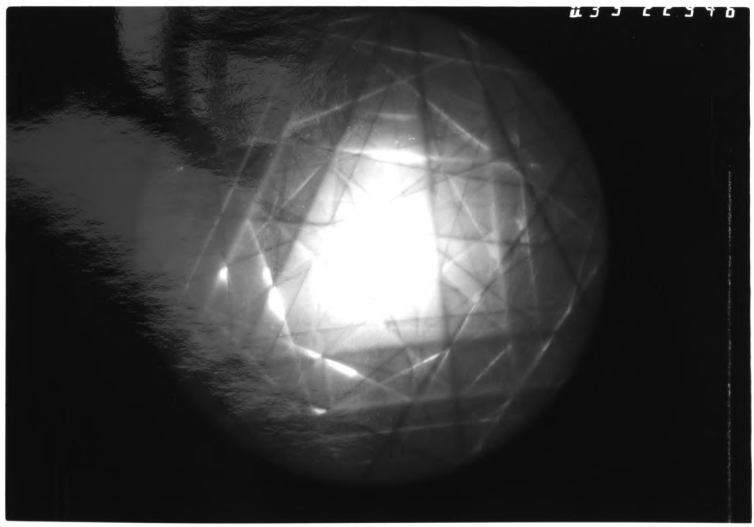

Fig. 2.13

Schematic ray diagram illustrating the reciprocity between TEM (upper row, read left to right) and STEM (lower row, read right to left).

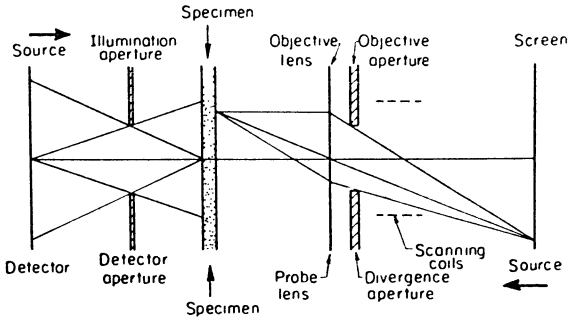
Specimen
Source
Illumination aperture
Objective lens
Objective aperture
Screen
Detector
Detector aperture
Specimen
Probe lens
Scanning coils
Divergence aperture
Source

Chapter 3

The Deformed State

Introduction

In this chapter the deformation structures observed in copper and copper-alumina (alloys L and H) (111)[1$\bar{1}$0] single crystals are described at equivalent true strains of 5, 11, 20, 36 and 69% (equivalent to rolling reductions of 5, 10, 18, 30 and 50%). Observations of specimens rolled to greater reductions were not possible due to the difficulties encountered in specimen preparation as outlined in section 2.8. In addition, (110)[1$\bar{1}$2] single crystals of copper and copper-alumina (alloy M) were examined at a strain of 69%. All observations were performed on longitudinal sections at 400keV in the Oxford HVEM unless otherwise stated.

The deformed structures are discussed and interpreted in comparison with the observations of other workers.

3.1 Results

3.1.1 The Deformation Structure of (111)[1$\bar{1}$0]-Copper Crystals

a) The homogeneous structure

No differences could be found between the dislocation structures, at a given strain, observed in pure copper and internally oxidised copper. Thus, the observations below apply to both.

After the initial deformation (5% strain) discrete dislocation

tangles were found enclosing large dislocation-free areas, figs. 3.1 and 3.2.

At 11% strain an equiaxed cell structure has formed (fig. 3.3) with few dislocations inside the cells. Care has to be taken during observation, that the beam is not condensed too greatly, or the same area of specimen observed for long periods, as dislocation rearrangement can occur e.g. fig. 3.4 is the same region as fig. 3.3 viewed for a longer period in which some dislocation rearrangement has occurred and some dislocations have slipped out of the foil.

Further deformation leads to a reduction in the cell size and increasing alignment of cell walls along the {111} traces close to the rolling plane, fig. 3.5 and 3.6. Fig. 3.7 shows a typical cell at 36% strain.

Selected area diffraction patterns taken with a SAD aperture encompassing several cells (1.7microns dia.) showed an increasing diffuseness of Kikuchi lines in the diffraction pattern. However, even at 69% strain, Kikuchi lines could still be seen in diffraction patterns, although diffuse, and no splitting of diffraction spots occurred. Thus although the increasing dislocation density leads to diffuseness in the Kikuchi pattern, the dislocations did not produce large or cumulative misorientations across cell walls. The misorientations across cell walls were measured at 69% strain using STEM microdiffraction; these were found to be small $0.3^{o} < \theta < 0.8^{o}$. A typical example is shown in fig. 3.8.

Measurements of the cell diameter parallel to the rolling direction showed little decrease in size when specimens had received strains greater than 11%. Histograms of the frequency of cell diameters observed normal to the rolling plane (from 100-150 cells)

are shown in figs. 3.12c, 3.13c and 3.14c for strains of 20%, 36% and 69%. The mean cell size and the width of the distribution both decrease as the strain is increased.

Inhomogeneities

Microbands were first observed in the electron-microscope at 20% strain, although they were an infrequent occurrence. The example shown in fig. 3.15 is 0.38 microns wide and lies along a {111} plane. The walls of the microband consist of intense dislocation tangles. Contrast differences across the band suggest that the misorientations across the walls of the microband are greater than those across the walls of the cells. The cell structure around microbands was found to be slightly different from the cell structure as a whole.

As the deformation was increased, the occurrence of microbands increased and they decreased in width. Figs. 3.16 and 3.17 show two microbands at 36%strain. They vary in width along their (3-4 microns) length but are a maximum of 0.2 microns wide. The interiors were found by tilting experiments to be fairly dislocation free, however, dislocation walls existed within the microbands perpendicular to their length. Contrast differences were also noted across these interior walls. The misorientations present across microband walls at 69% strain were measured using STEM microdiffraction, see figs. 3.18 and 3.19. They were found to be approximately 2^{o}, although misorientations between opposite sides of the microbands were found to be smaller (less than 1^{o}). The misorientations across walls occurring along the length of the microband were found to be of the same order of those along the length (2^{o}).

Below 69% strain only discrete microbands were observed, whilst

at this strain some microband clusters were found, see fig. 3.8. At each of the deformations examined in the electron microscope a copper crystal was sliced longitudinally, the free surface mechanically polished, as described in section 2.7 then all of the crystal except this new surface was covered in lacomit and the new surface electrolytically polished using the final TEM polish, described in section 2.8. The lacomit was physically stripped from the specimen and the specimen given a single light rolling pass in order to develop slip lines on the new surface. These slip lines or Type III markings have been identified by Malin and Hatherly (1979b) as corresponding to microbands. The slip lines were not evenly distributed throughout the specimen. Only two sets of straight slip lines were found at the centre of the specimen, fig. 3.22, whilst, near the specimen's surface, the slip lines were found to be more closely spaced and of a more complex nature, fig. 3.23. This effect is because of friction between the rolls. The effect of friction decreases at greater depths in the crystal and only in the centre is true plane strain observed. Increased deformation caused the slip lines to curve, fig. 3.25. This again is a friction effect and is because the crystals' slip planes are rotating at a rate which varies with distance from the surface.

These observations are essentially similar to those of Jago and Hatherly (1975) on copper single crystals. It had been hoped to measure slip line spacings, however, these varied not only through the thickness but also along the length. Thus, only the qualitative statement that the slip line spacing decreased with strain can be made, see figs. 3.20, 3.22 and 3.24.

3.2 Structure of Copper-Alumina (Alloy L)

3.2.1 The homogeneous Structure

In the copper-alumina alloy a cell structure has formed by 5% strain, figs. 3.26 and 3.27. The `blocky' cells have diffuse walls which lie along {111} planes. Most cells are elongated along the {111} planes close to the rolling plane, although some are elongated along other {111} planes. The cell walls in the rolling plane contain more dislocations than the other walls. Although most dislocations are in the dislocation walls the cell interiors also contain dislocations, especially around particles that do not lie in the cell walls. The walls parallel to the rolling plane are not continuous throughout the crystal but are often several microns long. On the other hand, the walls perpendicular to the rolling plane often stop when they intersect a wall parallel to the rolling plane. Further deformation (to 11% strain) leads to a reduction in cell dimensions, fig. 3.28, and many cells are now `elongated' in the rolling direction. The cell interiors also contain less dislocations.

Even in the particle-containing alloys where dislocations are pinned by particles, loss of dislocations can occur in thin regions of the foil. Near the edge of the foil no dislocations are observed, whilst in slightly thicker regions an anomalous cell structure is observed. The thickness of foil for which a representative cell structure can be observed is such that 100keV electrons are not useful, e.g. fig. 3.29 shows the cell structure observed at 100keV in a `thick' region of foil. Thus, all the observations of the cell

structure at low strains were at 400keV.

No change in the lengths of the cells was observed with increased deformation above 11% strain. However, the cell dimension normal to the rolling plane decreased continually with strain and histograms of the cell sizes at each strain are shown in figs. 3.10b-3.14b. Increased deformation caused the width of the distribution of cell sizes to decrease and become more `log-normal' in appearance.

The cells not only assume a lenticular appearance with increased deformation but the cell walls normal to the rolling plane are much thicker and contain more dislocations, figs. 3.32 and 3.33, up to 36% strain.

However, at 69% strain, some recovery has occurred, as the elongated cell structure has changed to a banded structure with sharp cell walls in which individual dislocations are difficult to resolve. Although the elongation is now still in the rolling direction, the alignment of walls with {111} traces is less prominent, fig. 3.34.

Selected area diffraction experiments in which the SAD aperture (1.7microns dia.) covered several cells found that no Kikuchi patterns could be observed at 20% strain and above. Splitting of diffraction spots also occurred above 20% strain and this became more pronounced with increased deformation. The splitting of diffraction spots indicates that small misorientations are present across cell walls. These misorientations also produced contrast differences between cells which increased with strain, until at 69% strain the contrast differences were large.

The misorientations across the sharp band walls observed at 69% strain were measured using the STEM microdiffraction technique, fig. 3.35. The misorientations were not found to be cumulative across the

bands and were typically 3-4°. The rotation axis between bands was found not to be the same in each case and was not rational. Misorientations of a similar order were also measured along the length of the band. Selected area diffraction from the region, fig. 3.35, indicated a 5° lateral spread of diffraction spots about the beam axis.

3.2.2 Inhomogeneities

Microbands were first observed at 11% strain. These were essentially similar to those found in the copper and lie along a {111} plane at approximately 55° to the rolling plane. The example shown in fig. 3.31 is 0.33microns wide and 4.5microns long. Observations of microbands at higher strains was difficult as the overall dislocation density was high and the cell size small. The occurrence of microbands was also examined optically using the same technique as for the copper. Similar observations were found to the copper, although the slip lines appeared to be less widely spaced, see fig. 3.21, with the proviso noted earlier that quantitative measurements are difficult.

Transition bands were seen in the TEM at 69% strain as a more confused cell structure in which the cells are elongated in a direction ~40° to the rolling plane; the band itself lying approximately parallel to the rolling plane trace, fig. 3.37. At 69% strain, they were only spaced about 20microns apart and continued throughout the foil. Malin and Hatherly (1979b) suggest they consist of clusters of microbands. Selected area diffraction shows large misorientations between the homogeneous banded structure (17.5 and 26°) and these microband clusters, although opposite sides of the

microband are less misoriented (8.5°) in fig. 3.38. The misorientations, as observed by spot splitting in diffraction patterns, are much greater in these transition bands than in the homogeneous banded structure.

Fig. 3.40 also shows the cell structure observed in a transverse section.

3.2.3 Alloy H

At the lowest strains, alloy H has a smaller cell size than alloy L, figs. 3.10-3.14, with more dislocations in the cell interiors, figs. 3.41 and 3.42. Otherwise, the dislocation structure found in alloy H is essentially the same as that in alloy L.

Although alloy H contains more particles than alloy L, recovery can still occur in thin regions of the foil. Fig 3.49 shows the change of cell structure with foil thickness. The edge of the foil is dislocation free. Slightly thicker regions contain an anomalous cell structure whilst a cell structure representative of the bulk is seen in even thicker regions. Diffraction patterns taken from the edge in which the anomalous cell structure is observed show 'extra' spots due to recovery. Malin and Hatherly (1974) similarly noted only a 2° circumferential spread in SAD patterns taken from thicker regions of 98%-rolled OFHC copper foils, whereas near the edge a wide orientation range with different orientations present could be found.

3.2.4 (110)[1$\bar{1}$2] Crystals

Using a (111)[1$\bar{1}$0] orientation the cell walls could be construed as lying parallel to the rolling plane rather than the {111} plane. However, fig. 3.51, which shows the cell structure at a strain of 69% for copper of (110)[1$\bar{1}$2], demonstrates that the cell walls lie along {111} planes. In thinner regions of the foil recovery again occurs and this leads to a large equiaxed 'cell structure' similar to that reported by some other workers, fig. 3.52.

Fig 3.53 shows the 'blocky' cell structure of a copper-alumina alloy at a strain of 69%. Elongation of cells is along the {111} plane which is closest to the rolling plane. Although no detailed measurements of cell sizes in these alloys were made the cell size was larger at 0.34microns in alloy M than those in alloys L and H at 69% strain. This could be because of the larger interparticle spacing in alloy M but could also be an orientation effect. e.g. Dillamore, Smith and Watson (1968) found that the cell size differed between grains in rolled polycrystalline iron. The cell size decreased as the rolling plane changed from (001) through (112) and (111) to (110) with [1$\bar{1}$0] in the rolling plane. Fig. 3.54 shows microbands in this material at approximately 30-35^{o} to the rolling plane. The 'blocky' cell structure seems to have been destroyed between microbands. The microbands were sometimes only 30nm wide.

The hardness was measured at each strain for the (111)[1$\bar{1}$0] crystals and the results are shown in fig. 3.55.

3.2.5 Summary of General Features of Deformation Structure of Copper

The essential features of the deformation structure formed during rolling of copper can now be summarised.

Cells form from dislocation tangles at 11% strain. Further deformation leads to a reduction in both the mean cell size - cells become narrower normal to the rolling plane but stay essentially the same length in the rolling direction - and the width of the cell size distribution. Some alignment with the {111} plane closest to the rolling plane also occurs at higher deformations.

Microbands are found to increase in frequency as the strain increases so that some microband clusters are found at 69% strain. Misorientations of approximately 2^{o} are found across these microbands at this strain, this is larger than those found across ordinary cell walls of $0.3^{o} < \theta < 0.8^{o}$.

3.2.6 Summary of Deformation Features in Copper-Alumina

The cell structure is formed at 5% strain. The mean cell size and cell size distribution width decrease with increasing strain. Sharp alignment of the cell walls with {111} planes is found until 69% strain when recovery produces narrower cell walls and less adherence of the boundaries to {111} planes. The cell structure appears more elongated in the rolling direction as the strain increases, this is due to a reduction in the cell thickness normal to the rolling plane.

The density of microbands increases with strain so that at 69% strain broad transition bands, containing large misorientation spreads, are found.

3.2.7 Comparison of Results for Copper and Copper-Alumina

The essential differences in the deformation structures of copper and copper-alumina can now be outlined. A higher dislocation density is observed in the copper-alumina than in the pure copper for a given strain. The cell structure forms at a lower strain in copper-alumina than in copper and the cells which form are smaller; this cell size is smaller for a larger number of particles. The mean cell size and width of the cell size distribution are both smaller at all subsequent strains in the copper-alumina than in the copper. The cells also show greater alignment with {111} planes in the particle-containing material.

A greater microband density is found in the copper-alumina and this leads to the presence of transition bands at the highest strain observed (69%). Larger misorientations are found across dislocation walls in the copper-alumina than the pure copper. Dynamic recovery was also found to occur in the copper-alumina at 69% strain.

Table 3.1 summarizes the differences between the deformation structure in copper and copper-alumina as a function of strain.

3.3 Discussion

3.3.1 The Deformed Structure of Copper

That cells form from discrete dislocation tangles, as found here, is well documented e.g. Embury, Keh and Fisher (1966). This process has also been observed dynamically by Tabata, Yamanaka and Fujita (1978). However, the morphology of the cells in copper and their

subsequent change with increasing strain is not agreed upon. Two distinct views of the cell morphology exist, these will be considered and compared with the present work.

Most early data are summarized in the results obtained by Wingrove (1972). He found that the equiaxed cells, with walls consisting of discrete dislocations which formed at strains below 100%, gave way to polygonised cells with sharp walls at higher strains. He shows a decrease in cell size with increasing strain until a strain of ~150%, after which no further reduction occurs; the cell size correlated well with the measured hardness values, see fig. 3.56. Cairns, Clough, Dewey and Nutting (1971) reported similar results in drawn copper tube and noted that at very high strains the polygonized cells, which were elongated in the rolling direction, gave way to a banded structure whose dimensions did not change with subsequent deformation although the misorientations across the band boundaries increased with strain (but were <5°).

Many workers have noted that the hardness and cell diameter are related by an equation proposed by Hall (1954):-

$$H.V. = H_o + \frac{k}{\overline{l}} \qquad (3.1)$$

where H.V. is the hardness, l the cell size and H_o and k are experimental constants. Similarly Friedel (1964) gives the hardening, σ, due to an unrelaxed cell structure as

$$\sigma = \frac{Gb}{\beta l} \qquad (3.2)$$

where b is the dislocation's Burgers vector, G the shear modulus and β

lies between 3 and 4, with l related to the dislocation density ρ by

$$l \propto \rho^{-1/2} \tag{3.3}$$

Holt (1970), using perturbation analysis, showed that a homogeneous dislocation array could lower its energy by forming cells with a 'wavelength' proportional to $\rho^{-1/2}$. He quotes considerable data to support this relation and the proposition that $l \propto \sigma^{-1}$. This relation has received recent experimental confirmation by Tabata et al. (1978). Using a HVEM at 2MeV to observe in-situ deformation of aluminium single crystals they found that mobile dislocations were stopped at cell walls and found no evidence of slip traces that had entered neighbouring cells.

Malin and Hatherly (1979a, 1979b), however, present a different picture of the changes occurring during deformation. They state that the equiaxed cells which are formed after 5-10% strain are still present at high strains with no change in their size (~1 micron). They suggest that after cell formation, subsequent deformation is accommodated by microband formation and that the banded structure, which is found at high strains, develops from these microbands which rotate to be parallel to the rolling plane during deformation. They explain that the reduction in cell size observed by other workers arises because a linear intercept method would be used to obtain cell sizes and that this includes not only the equiaxed cells but also microbands. As the latter increase in frequency during deformation, and are smaller than the equiaxed cells, an observed reduction in cell size occurs with increasing strain. Consequently, they also question the validity of equation 3.1. The equiaxed cells, they note, must be caused by a relaxation process since their morphology cannot be

related to the operating slip systems. Whether this relaxation occurs after load removal or during foil thinning is not known. However, Howie (1960), using slip plane sectioning of copper single crystals, found that the cell structure formed during stage III could be related to the operating slip system.

The cell structures found here decreased in size during deformation (and did not include measurements of microbands). The cell structure changed from being equiaxed at low strains to showing some alignment with {111} traces closest to the rolling plane as the strain increased. The equiaxed structure must form by relaxation.

That relaxation is easier at low strains was affirmed by two observations. Firstly, at low strains, dislocations in pure copper could only be observed in regions of the foil which were near the limits of penetration of 100keV electrons. Secondly, if the electron beam (at 400keV) was condensed or allowed to remain on the same area of specimen for long periods, dislocation movement occurred and slip traces were observed; these were more frequent at low strains. Hirsch and Valdré (1963) also noted that the extent of dislocation rearrangement during thinning and observation decreased as the deformation increased. Dislocations can be lost by three processes; reorientation of screws and subsequent cross slip out of the foil, dislocations can slip out of the foil edge, or if neither of these are geometrically possible, the dislocation length can decrease by reorientation of the dislocation in order to minimize its energy. At high strains, dislocations are involved in more complex tangles and these processes, thus, become more difficult.

However, the structures observed, even at low strains, are probably representative of the bulk when imaged in thicker foils using

400keV electrons. The plot of hardness against reciprocal cell size, fig. 3.57, which yields a linear relationship, suggests that the cell structure observed at 11% strain is fairly representative of the bulk. Thus the equiaxed cell structure observed at lower strains must form mainly by relaxation after load removal.

During deformation, locks and barriers will occur on active slip planes such that dislocation pile-ups occur, other dislocations will interact with these to produce tangles lying essentially along {111} planes. However, after removal of the load many dislocations will run back down slip planes, the length of loops which have been generated to by-pass obstacles will shorten and, in general, dislocations will move in order to minimize their energy. Subsequent deformation will occur on this equiaxed cell structure. The larger number of dislocations formed during subsequent deformation will refine the cell size and result in more complex tangles, so that relaxation after load removal becomes more difficult. Thus greater alignment with {111} planes occurs.

However, the equiaxed cells observed by Malin and Hatherly (1979b) must form by recovery during foil thinning since their dimensions do not change with strain. It is interesting to note that equiaxed cells could also be observed in the present work at high strains but only near the foil edge, fig. 3.52. The observation of equiaxed cells by other workers could be due to the nature of the slip in the polycrystals which they were deforming, since at least five slip systems would have to operate.

3.3.2 The Change of Cell-Size with Strain

The reduction in cell size as a function of strain has been investigated by several workers. In b.c.c. iron the cell size has been found to decrease continuously with deformation. Embury, Keh and Fisher (1966) found that this decrease in cell size was concomitant with the change in drawn wire diameter whilst Langford and Cohen (1969) found that the rate of decrease in cell size was initially greater than the decrease in drawn wire diameter but that with increasing strain the rate of decrease in cell size was less than the decrease in wire diameter.

In F.C.C metals, the cell size has often been found to reach a limiting value which depends on the stacking fault energy and purity of the metal. Thus, Embury, Keh and Fisher (1966) found that although the cell size in drawn copper wire initially decreased concomitantly with the wire diameter, the deviation from this 'geometric reduction' in size increased as the limiting cell size was approached.

If the cell structure, once formed, subsequently deforms only in the same way as the specimen as a whole and no other processes occur, then the cells can be said to be undergoing a geometric deformation. For cells undergoing a plane strain deformation, as the strain is increased, the cell size along the rolling direction (tensile axis) should increase continuously, whilst the cell size normal to the rolling plane (compression axis) should decrease continuously; the cell size in the transverse direction should be invariant as no macroscopic change in dimension occurs in this direction. The geometric deformation can be conveniently represented on a graph of log cell size against strain as a straight line. For plane strain, the

geometric deformation of the cell size normal to the rolling plane has a slope of -1 on such a plot. A steeper slope than this shows that new cell walls are forming whilst a slope less than this shows that cell walls are being destroyed.

In the present work on pure copper, the cell size in the rolling direction remained approximately constant after 11% strain, whilst the cell size normal to the rolling plane was found to decrease at a rate greater than the geometric reduction in size up to a strain of 36%, see fig. 3.58. Hu (1969) also found that the transverse and rolling direction cell size did not change in size with strain but that the cell size normal to the rolling plane decreased continuously with strain. Thus, measurements indicate that wall creation was occurring possibly by branching of existing walls; this process has been observed dynamically by Tabata et al. (1978). As the rate of decrease between strains of 36% and 69% is essentially the same as the geometric deformation rate, no net wall formation is occurring. This can be envisaged as a balance between dislocation multiplication, which will lead to wall creation, and dynamic recovery, which will lead to wall annihilation. At greater strains, the rate of decrease of cell size might be expected to lessen as recovery becomes more important, so that ultimately a limiting cell size is reached.

At very high strains (>500%) spontaneous recrystallization has been reported during cold rolling of copper e.g. Cairns, Clough, Dewey and Nutting (1971) and Nutting (1974). Recrystallization without annealing was found to occur in the present work at higher strains (>200%) in the copper-alumina, although the grains shown in fig. 3.59 were only found after storage at room temperature and not immediately after rolling. The ease of such recrystallization is very dependent on

the matrix solute content, thus spontaneous recrystallization might be expected in the present work at high strains due to the high purity of the matrix.

3.4 Inhomogeneities

Microbands (in the form of type III markings observed optically) were found to occur at all the strains used here. Although quantitative measurement of the microband density was difficult, qualitatively it can be asserted that their density increased with increasing strain, in agreement with the observations of Ahlborn and Sauer (1968). This increase in density was observed in the electron microscope by evidence of some microband clustering at higher strains.

Evidence was also found of a decrease in microband width with increasing strain. They ranged from 0.34 microns wide in alloy L at 11% strain to as small as 0.03 microns in alloy M at 69% strain. Misorientations across microband walls were found to be $\sim 2^{o}$ (which was considerably larger than that found across ordinary cell walls at $0.3^{o} < \theta < 0.8^{o}$).

Malin and Hatherly (1979b) state that microband interiors were full of dislocations. The present work does not support this view. The microband walls were found to consist of intense dislocation tangles whilst the interiors were concluded to be relatively dislocation-free since (i) few dislocations could be seen in the interiors during tilting experiments and (ii) good quality Kikuchi patterns could be obtained from the microband interiors. This difference in the structure of the microband interiors could, however, be due to differences in purity. The copper used in the present work was of

higher purity than that used by Malin and Hatherly (1979b) so that dislocations would experience fewer solute pinning effects and rearrangement would be easier. Dislocation walls were found along the length of microbands (at spacings of ~ 1 micron) and these were found to have similar misorientations across them to those across the microband walls (2^{o}).

The microbands were found to lie along {111} planes which were inclined to the rolling plane and no observations of their rotation to become parallel to the rolling plane were found in the electron microscope. However, their detection would be more difficult as they rotated towards the rolling plane since they would become aligned with the walls of the homogeneous cell structure. However, the curvature of the slip lines to become parallel to the rolling plane was found optically. This curvature was only found near the middle of the specimens where true plane strain occurs. Near the specimen surface, the randomising effect of the friction forces may have prevented rotation of the lattice. The curvature of slip lines is in agreement with the concept of microbands rotating to lie parallel to the rolling plane.

The mechanism of microband formation is not understood. Malin and Hatherly (1979b) have tentatively suggested that microbands are formed by co-operative shear on planes only 8nm apart (compared to the usual 30nm slip spacing in the homogeneous structure) on the {111} planes nearest to 35^{o} to the rolling plane. They can make no suggestions as to why microbands cluster together, however.

The present work does not lead to any clarification of the mechanism but does not contradict the model of Malin and Hatherly (1979b). However, the observations eliminate the suggestion by Ahlborn

and Sauer (1968) that microbands form by elongation and amalgamation of the ordinary cells, since the elongation of cells found here was in the rolling direction and microband formation was on {111} planes inclined to the rolling plane.

3.5 The Effect of Particles on the Deformed Structure

3.5.1 The Initial Homogeneous Structure

Although no attempt was made to measure the dislocation densities, due to the difficulty of these measurements, the density of dislocations in the copper-alumina alloys was by inspection obviously larger than that in the pure copper. The increase in dislocation density is due to the geometrically necessary dislocations required to accommodate the plastic strain around the particles. This dislocation density increase has been measured by Lewis (1963), who found that the dislocation density at 8% tensile strain was raised from 8×10^{13} m/m^3 in pure copper to 2×10^{14} m/m^3 in internally oxidised copper -0.26 silicon polycrystals. This dislocation density increase manifested itself in the present work as an increase in hardness in the particle-containing alloys (which was larger for a higher volume fraction of particles, fig. 3.55).

Besides an increase in dislocation density, the particles also modified the cell structure compared to the pure phase. The cell structure in the particle-hardened alloys formed at lower strains and was smaller in size. For pure copper it was noted that the cell structure forms from the discrete dislocation tangles. In particle-containing material, the discrete dislocation tangles are

associated with particles. This was demonstrated by Lewis and Martin (1963) who found that the spacing of dislocation tangles (at a tensile strain of 8.2% where a cell structure had not formed) in various internally oxidised polycrystals depended on the interparticle spacing.

The cell structure forms from these tangles and must therefore be related to the interparticle spacing i.e. the initial cell size was found to be smaller for alloy H which had a smaller interparticle spacing than alloy L. However, the cell size formed was larger than the interparticle spacing so that some particles can not be associated with cell walls; this was often noted to be the case. The larger number of dislocations and tangles also means that cells will form at lower strains.

The final difference in the initial cell structure, is that the particles cause the cell walls to be closely associated with {111} planes even at the lowest strains. A similar result was found by Swann (1963) in aluminium, where the equiaxed cells usually found in the pure metal were replaced by a more diffuse dislocation structure which was aligned along {111} planes when θ-$CuAl_2$ precipitates were introduced.

The particles can cause this alignment in two ways. Firstly, the geometrically necessary dislocations which form around particles will interact with the statistically stored dislocations forming complex tangles and locks from which relaxation will be difficult. Secondly, the particles themselves will prevent movement of dislocations. Thus relaxation of the cell structure will be inhibited.

3.5.2 The Effect of Strain: Band Formation

In the initial cell structure, at 5% strain, there is a difference between the cell walls parallel to the rolling plane which contain more intense dislocation tangles and other walls. The walls which constitute the boundaries to cells are not continuous. However, the walls parallel to the rolling plane are long, whereas other walls often stop when they meet a wall parallel to the rolling plane. This is shown schematically in fig. 3.60.

Subsequent deformation leads to a reduction in the cell size normal to the rolling plane which is greater than the 'geometric deformation', see fig.3.58. This can be achieved by the extension of the wall at X to position Y, in fig. 3.60. This is essentially the mechanism observed dynamically in the HVEM by Tabata et al. (1978) where new cell walls were formed by branching of previously formed ones. The extension from X to Y will be by the trapping of mobile dislocations.

This mechanism will also occur in other directions, so X will extend to Z as well. This is also required since from 5 to 11% strain, the cell size parallel to the rolling direction decreases in size, after which it remains essentially the same, whereas geometrically the cell size should be increasing.

Increased deformation (5-36% strain) leads to a more elongated cell shape with thicker dislocation walls and more dislocation-free interiors. Up to 36% strain, alloy L shows a reduction in cell size greater than that for geometric deformation, implying cell wall creation.

From 36-69% strain alloy L experienced a reduction in cell size

normal to the rolling plane at the rate of geometric deformation only. At 69% strain the microstructure also changes from the elongated cell structure to a banded structure with sharp cell walls. Some dynamic recovery has clearly occurred. The banded structure is aligned with the rolling direction but individual walls deviate considerably from the {111} planes. Recovery of the structure would have allowed cell walls to leave the sharply defined {111} planes and possibly take a lower energy configuration which may include more particles in these boundaries, although some particles still remain inside the bands.

This banded structure is similar to that observed in copper at high strains. It must form at a lower strain in the copper-alumina alloys because of the greater dislocation density and thus the greater driving force for recovery.

Note that in alloy H, the decrease in cell size appears to conform to the geometric deformation rate at a lower strain (20%) than in the pure copper or alloy L (36%). This is probably because of the much larger dislocation density, which will again mean a larger driving force for recovery.

The banded structure in the copper-alumina obviously forms from, and replaces, the elongated homogeneous cell structure found at lower strains. This supports earlier work of Embury, Keh and Fisher (1966) and Cairns, Clough, Dewey and Nutting (1971) on copper who suggested that the banded structure was derived from the homogeneous cell structure.

3.5.3 Relationship of the Interparticle Spacing to the Dislocation Structure

The initial cell size found in both alloys is greater than any of the interparticle spacing parameters shown in table 2.2 and even at the highest strain (69%) was still larger than Δ_2 for both alloys.

Embury, Keh and Fisher (1966) have examined the dislocation distributions for a 0.1C, 0.5Mo steel which was given different ageing treatments to produce two different carbide dispersions. In a specimen containing fine carbides (10nm) closely spaced (20nm) they found a cell structure formed which was much larger than the interparticle spacing. In a second specimen containing larger carbides (20nm) more widely spaced (40nm) no cell structure formed. At high strains a banded structure formed which was larger than the interparticle spacing (although the latter parameter was not specifically defined). In an iron alloy containing 2wt% copper, for which they do not give dispersion parameters but describe as much coarser, they found that the initial cell size was the same as the interparticle spacing and decreased on further deformation.

Hansen and Bay (1972) concluded that the cell size of rolled SAP was not greatly affected by either the particle content or the distribution of alumina particles i.e. the cell size for a uniform dispersion of alumina only decreased from 0.40 to 0.38 microns for a decrease in interparticle spacing (Δ_2) from 0.17 to 0.09 microns and became the same after 90% reduction at 0.29 microns. The cell size of pure aluminium was only slightly larger at these two deformations at 0.48 and 0.37 microns respectively.

A difficulty in comparing cell sizes and interparticle spacings

measured by different workers is that the specific interparticle spacing parameter used is often unstated and all the dispersion parameters, such as volume fraction and particle size, are not given so that the use of a single spacing parameter for comparison purposes is not possible. Thus the relationship between cell size and interparticle spacing often appears to be different in work by different researchers because of the use of different interparticle spacing parameters.

However, the initial cell size will be the same size as the interparticle spacing (or slightly larger as some particles occur inside cells, e.g. cells in alloy L were initially 0.89 microns thick whereas Δ_2 is 0.22 microns). Similarly, the final banded structure might be expected to be related to the interparticle spacing, since the bands form by recovery which will be inhibited by the addition of particles. The interparticle spacing may only be expected to influence the final `limiting' size of this banded structure if the interparticle spacing is smaller than the `limiting cell size' in the single phase. The banded structure found in the copper-alumina at 69% strain is unlikely to be the limiting cell size since it is larger than most single-phase `cell sizes' found by other workers and is larger at 0.23-0.24 microns than the interparticle spacings of alloys L and H (Δ_2 = .22 and 0.14 microns respectively).

3.5.4 Inhomogeneities

Microbands observed in the copper-alumina alloys are essentially the same as those found in pure copper, although their detection is more difficult because of the inherently greater dislocation density

of the homogeneous structure in the copper-alumina and because the cell walls are aligned with {111} traces.

Although quantitative comparison of the densities of microbands in copper and copper-alumina is difficult, four factors point to a greater density in the latter: i) Optically, microbands appeared closer in the copper-alumina, ii) Microbands were observed at lower strains in the TEM in the copper-alumina (11% strain) than in the copper (20% strain), iii) Malin and Hatherly (1979b) suggest that deformation by the formation of microbands occurs because deformation becomes increasingly difficult to accommodate in the homogeneous matrix as the strain increases. As the copper-alumina alloys have a smaller cell size and thus contain more barriers to dislocation motion, then microband formation might be expected at lower strains and should be more frequent. iv) Transition bands are observed at 69% strain in the copper-alumina and these are essentially the same as those observed in pure copper by Malin and Hatherly (1979b) at higher strains and consist of clusters of microbands.

A schematic representation of the deformed structure of the copper-alumina at 69% strain is shown in fig. 3.39.

3.6 Misorientations in Copper and Copper-Alumina

Information about the misorientations across cell walls was of three kinds: i) observation of contrast differences between cells (note that the absence of contrast differences across dislocation walls does not necessarily mean that no misorientations are present, since the contrast differences depend on the relative position of the rotation axis to the beam direction and the g value operating.

Conversely, contrast differences positively indicate that misorientations are present). ii) the degradation of a single diffraction pattern by the loss of Kikuchi lines and subsequent spreading and splitting of spots in SAD patterns, iii) misorientations measured directly from cells by STEM microdiffraction.

No real differences could be found between the two copper-alumina alloys (L and H), thus only a comparison of differences between alloy L and pure copper will be considered.

Both copper and copper-alumina showed increasing misorientations between cells as the strain was increased. However, degradation of diffraction patterns and contrast differences between cells were always larger at a given strain in the particle-containing material. This was best demonstrated by the use of the microdiffraction technique at 69% strain when misorientations of 3-4^{o} were found across the homogeneous banded structure in copper-alumina, which was much larger than those found across cells (0.3-0.8^{o}) or microband walls (2^{o}) in the copper.

The larger misorientations present across boundaries in the copper-alumina are due to the higher dislocation density in these alloys. The type of dislocations which compose the boundary will also be important in determining the magnitude of the misorientations present. For example, dislocations may occur as dipoles and no long range lattice curvature would occur across these. The latter type of dislocations will not be the geometrically necessary type. Thus extra dislocations in a boundary which are geometrically necessary will contribute to the misorientation across the boundary, whilst those in the single phase, some of which will be of dipole type, may not. Even larger misorientations were found across the transition bands in the

copper-alumina.

Brimhall and Huggins (1966) found only minor differences in the misorientations measured by selected area diffraction between rolled polycrystalline copper and copper-alumina, although they were slightly larger in the copper (14^{o} spread in 3 microns) than the copper-alumina (12^{o} spread in 3 microns). The particle sizes they used, 20-30nm, and interparticle spacings (λ_2), 180-250nm, were similar to those used in the present work.

The differences between the results of Brimhall and Huggins (1966) and those of the present work could be from three causes. i) the larger dislocation density in the single phase material they used, due to the larger number of slip systems needed in a polycrystal and the 'geometrically necessary' dislocations required for the compatibility of grains, could swamp any effects from the geometrically necessary dislocations due to particles. ii) the use of spot patterns from selected area diffraction alone is not very sensitive since the spreading of diffraction spots depends on the position of the rotation axis with respect to the beam axis. iii) recovery in the pure copper would result in a larger misorientation spread, this would be inhibited in the copper-alumina: recovery occurs most easily in rolling plane foils.

They also noted a smaller cell size in copper-alumina than copper and found walls in the copper-alumina aligned along low index directions at higher strains. Chopra and Neissen (1974) found that cells did not form in copper-alumina until higher strains. However, subsequent work has shown that little information can be obtained from the rolling plane foils which the above workers used due to the overlap of cell walls. Fig. 3.36 shows the structure seen in a rolling

plane foil in the copper-alumina (alloy L). Clearly little structural information can be seen and any measurement of the cell structure will lead to erroneous results. Thus, the 'lack of cell structure' reported in some particle-containing alloys is simply because of the smaller cell size in these materials and therefore cell overlap is more frequent in thin foil observations.

3.7 Summary

The deformation structure in copper can now be briefly summarized together with the effect of particles on this structure.

A cell structure forms from discrete dislocation tangles. The 'true' cell structure may be envisaged as that of the copper-alumina where barriers and locks form along {111} planes, so that the cell walls show alignment with the slip planes along which the dislocations glide. This structure is retained in the copper-alumina alloys since the intense dislocation tangles and the particles themselves prevent extensive dislocation movement so that little relaxation can occur. In pure copper, tangles are less intense so dislocation rearrangement can occur, thus the alignment with slip planes is much less (and non-existant at low strains).

The initial cell size in the particle-containing material is governed by, but is not the same as, the interparticle spacing, since the cell structure is formed from the dislocation tangles occurring around particles. The initial cell size in the pure copper is governed by the chance encounters of statistically stored dislocations. Thus as long as the interparticle spacing is less than the cell size that would form in the single phase the initial cell size in the

particle-hardened material will be smaller.

Increased strain reduces the cell size by wall formation due to the increased dislocation density (the width of the cell size distribution also decreases). This is reflected in the hardness so that the relation, $\sigma \propto l^{-1}$ (where σ is the hardness and l the cell dimension) is obeyed. At larger strains recovery becomes more important because of the higher dislocation density (and higher driving force for recovery) so that dislocation multiplication and subsequent recovery result in no net wall formation, although the dislocation density, ρ, should still increase in accordance with the relation $\rho \propto l^{-2}$. At high strains, when the driving force for recovery becomes larger still, net wall annihilation is envisaged so that a limiting cell size will be approached.

Microbands were found to occur more frequently at higher strains and with a decreased width. They were not found to form from the homogeneous cell structure.

Adding and increasing the number of particles decreases the cell size and increases the dislocation density, so that a greater driving force for recovery is present. Thus, recovery may become important at lower strains in particle-containing material, so that the decrease in cell size with increasing strain is slower in particle-containing material, although the initial cell size itself is smaller than the single-phase material.

The particles themselves may simply be envisaged as producing the initial cell structure. Subsequent properties depend on this smaller initial cell size. In this way, the results support the observation that the banded structure found in copper at high strains forms from the elongation and recovery of the homogeneous cell structure and not

from microbands which have rotated to be parallel to the rolling plane. Thus, the misorientations found across the recovered, banded structure found in the copper-alumina at 69% strain are essentially the same as those found in pure copper at higher strains by other workers. Similarly, the greater microband density at a given strain in the particle-hardened metal can be ascribed to the increased difficulty in deforming the homogeneous matrix, due to the smaller cell size, so that more deformation is accommodated by microband formation. The transition bands that were observed in the copper-alumina appear the same as those found by other workers in pure copper at higher strains. Finally, the misorientations found in the particle-containing material were much larger than those found in the single phase.

Thus, the concept of slip `homogenization' is supported by the production of smaller cells on deforming the copper-alumina. However, the larger misorientations present and the greater microband density at a given strain in the copper-alumina are at variance with this concept.

Table 3.1

Strain	Cu	$Cu-Al_2O_3$
5%	Dislocation tangles. Surface slip lines observed optically.	Cell structure formed aligned with {111} plane. Surface slip lines observed optically (smaller spacing than in pure copper).
11%	Equiaxed cell structure formed.	Reduction in thickness of cells to form more 'elongated' structure. First observations of microbands in electron microscope. Kikuchi lines in diffraction patterns become diffuse.
20%	Some alignment of cells with {111} plane closest to rolling plane. First observation of microbands in electron microscope.	Contrast differences between cells. Kikuchi lines no longer observed in SAD patterns.
36%	Curvature of slip lines noted.	Some splitting of diffraction spots in SAD patterns.
69%	Some contrast differences between cells noted. Only very diffuse kikuchi lines now present in SAD patterns. Clustering of microbands.	Recovery of 'elongated' cell structure to form band with sharp walls with misorientation of 3-4°; across them. Transition bands found in which very large misorientations are present.

Increasing frequency of microbands
Decreasing microband widths
Reduction in cell size

Fig. 3.1

(111)[1$\bar{1}$0] Copper crystal, 5% strain.

Fig. 3.2

(111)[1$\bar{1}$0] Copper crystal, 5% strain.

g[200]
0·5μ

g[200]
1 μ

Fig. 3.3

(111)[1$\bar{1}$0] Copper crystal, 11% strain.

Fig. 3.4

Above region, after some dislocation rearrangement has occurred whilst viewing in the HVEM at 400keV.

g[200]
1 μ

g[200]
0·5μ

Fig. 3.5

(111)[1$\bar{1}$0] Copper crystal, 20% strain.

Fig. 3.6

(111)[1$\bar{1}$0] Copper crystal, 20% strain.

g[200]
1μ

g[200]
{111} trace
1μ

Fig. 3.7

(111)[1$\bar{1}$0] Copper crystal, 36% strain.

Fig. 3.8

Microband cluster in a (111)[1$\bar{1}$0] copper crystal, 69% strain. Misorientations measured between the cells marked, using STEM microdiffraction, are:-

a-b = 0.4°

b-c = 0.4°

c-d = 0.3°

[200]
{111} trace
1μ

{111} traces
g[200]
0·5μ

Fig. 3.10

Cell size distributions at 5% strain.

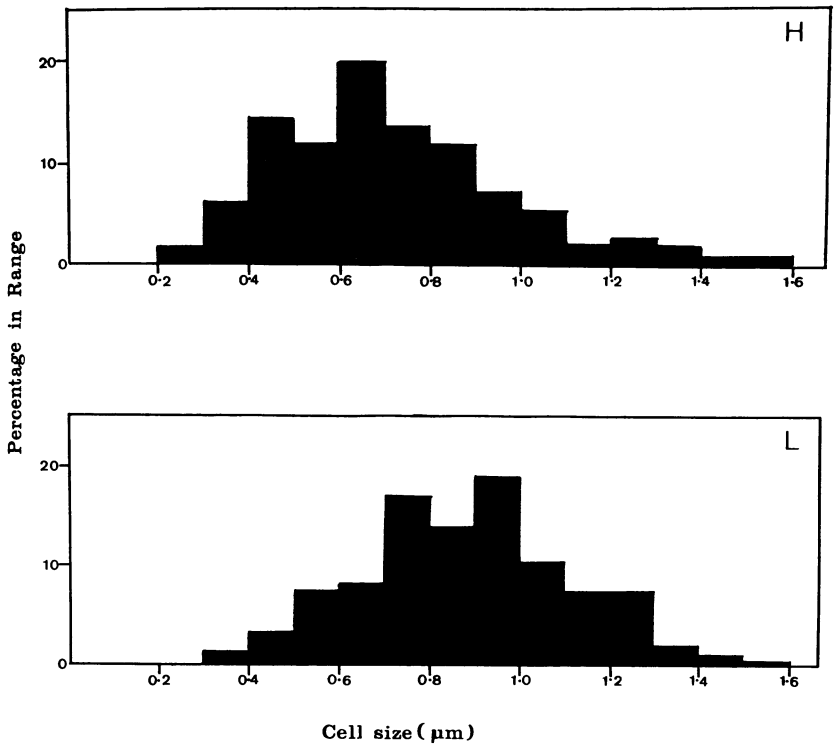
H
L
20
10
0
0·2
0·4
0·6
0·8
1·0
1·2
1·4
1·6
Percentage in Range
Cell size (μm)

Fig. 3.12

Cell size distributions at 20% strain.

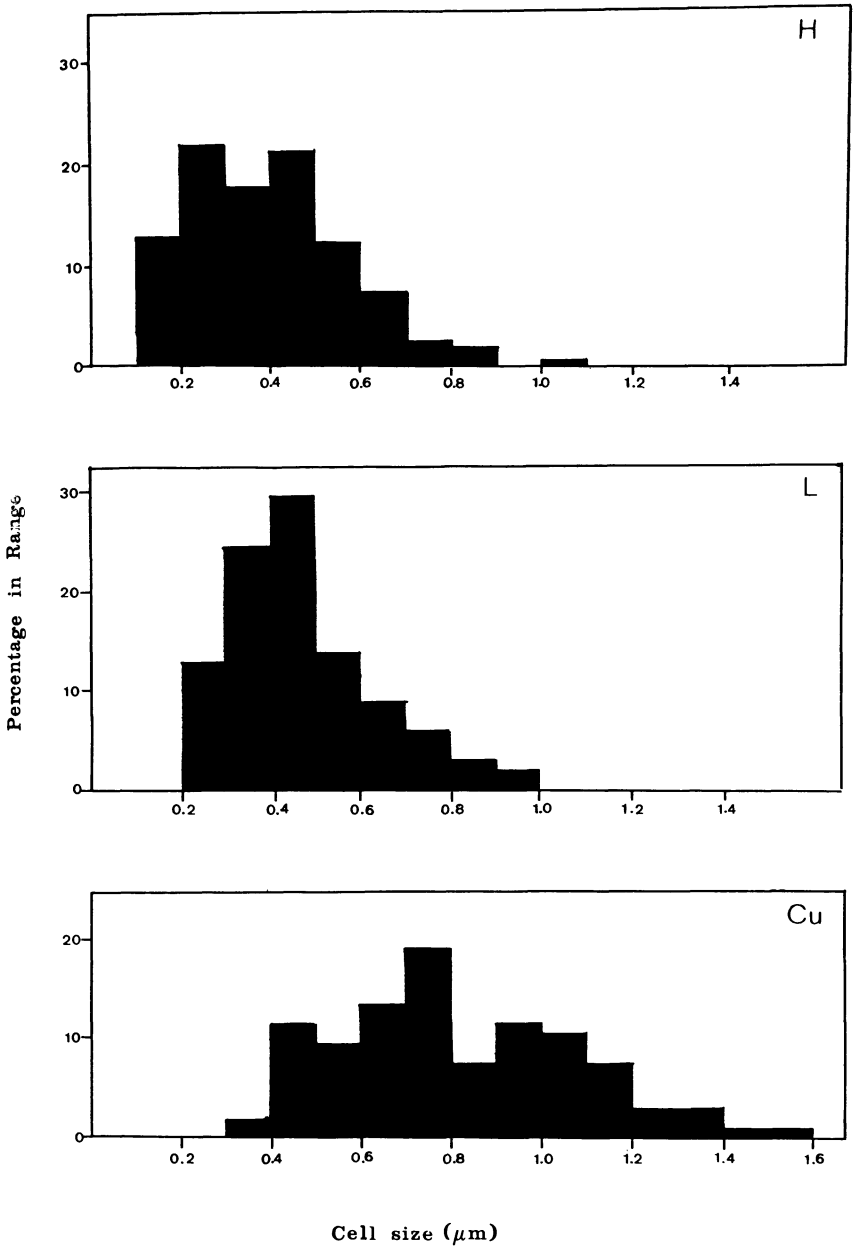
H
L
Cu
30
20
10
0
0.2
0.4
0.6
0.8
1.0
1.2
1.4
1.6
Percentage in Range
Cell size (μm)

Fig. 3.13

Cell size distributions at 36% strain.

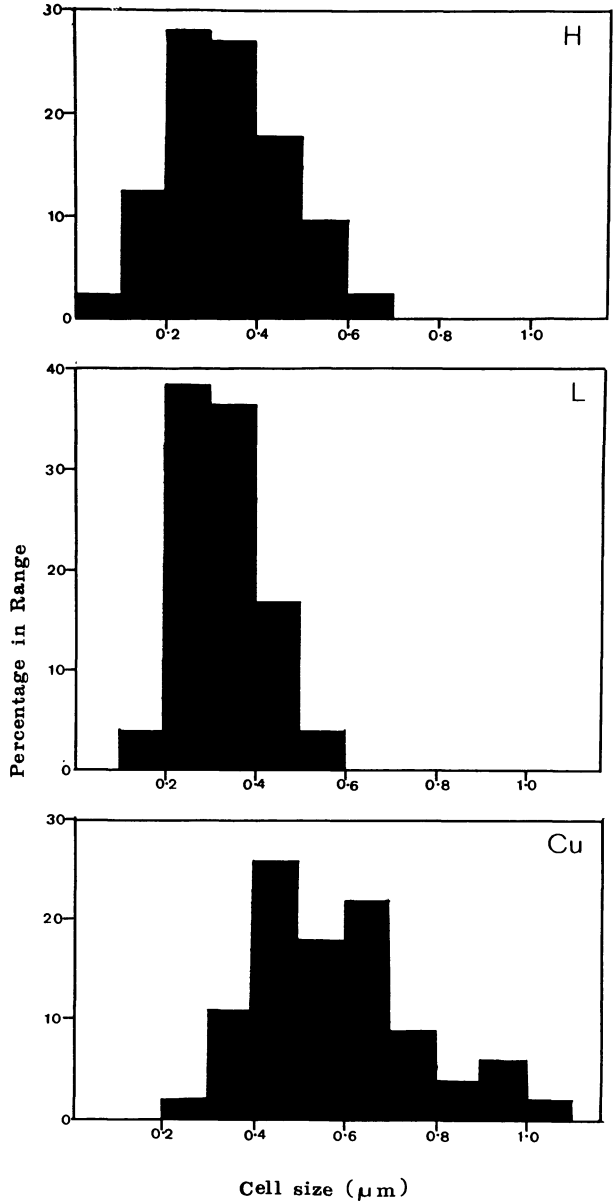
H
L
Cu
30
20
10
0
40
0·2
0·4
0·6
0·8
1·0
Percentage in Range
Cell size (μm)

Fig. 3.14

Cell size distributions at 69% strain.

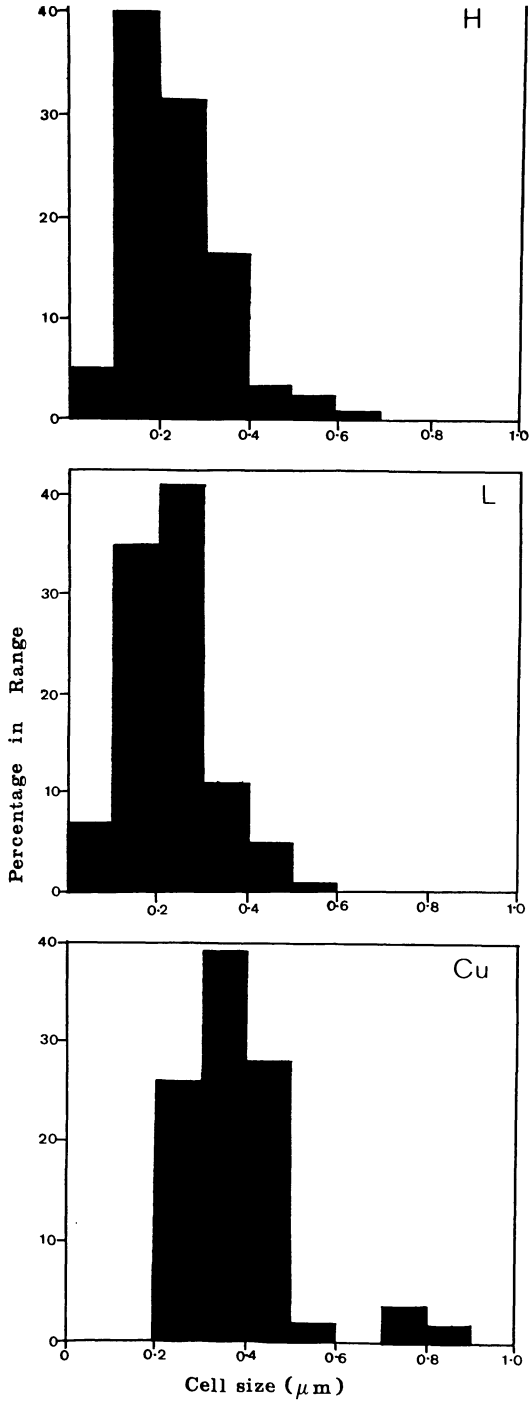
H
L
Cu
Percentage in Range
Cell size (μm)
40
30
20
10
0
0·2
0·4
0·6
0·8
1·0

Fig. 3.15

Microband in (111)[1$\bar{1}$0] copper crystal, 20% strain.

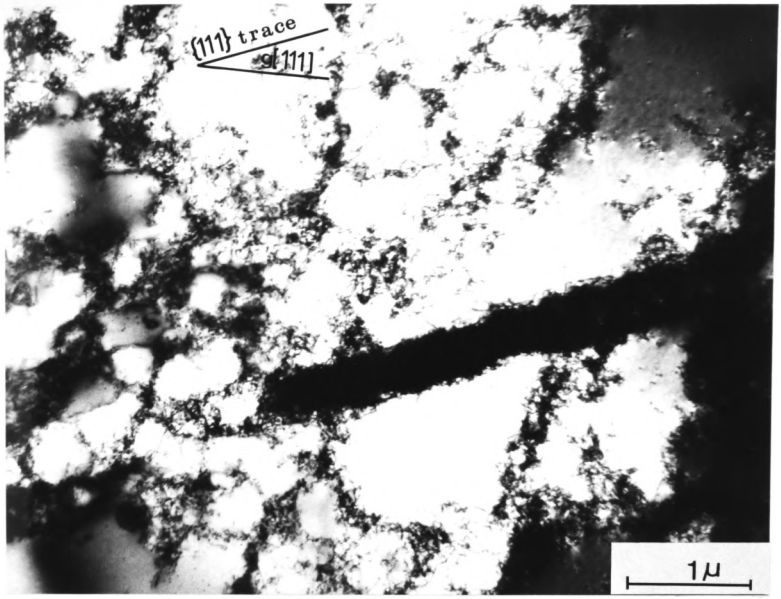
{111} trace
of [111]
1μ

Fig. 3.16

Microband in (111)[1$\bar{1}$0] copper crystal, 36% strain.

g [111]
(111) trace
0·2μ

Fig. 3.17

Microband in (111)[1$\bar{1}$0] copper crystal, 36% strain.

0·2μ
(111) trace
g [111]

Fig. 3.18

Microband in (111)[1$\bar{1}$0] copper crystal, 69% strain. Misorientations measured between the regions marked, using STEM microdiffraction, are:-

a-b - 1.9°

b-c - 1.9°

a-c - 0.8°

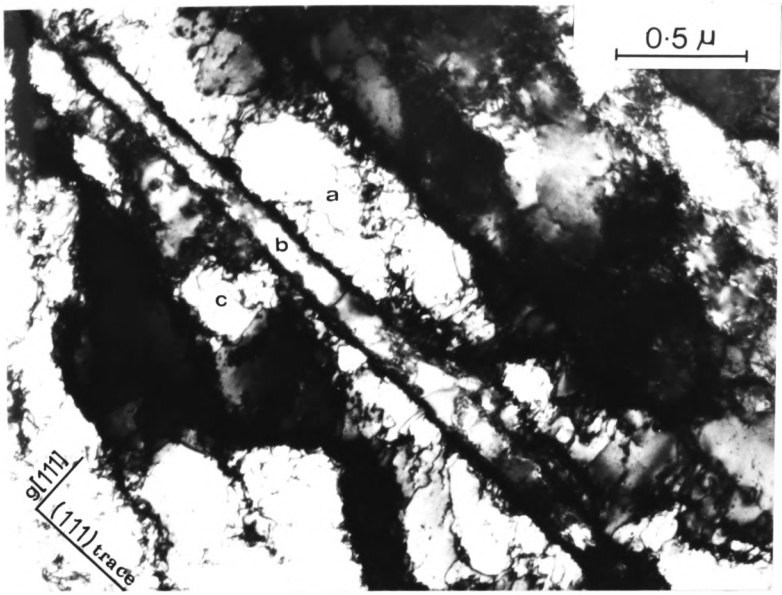
0·5 μ
a
b
c
g[111]
(111) trace

Fig. 3.19

Microband in (111)[1$\bar{1}$0] copper crystal, 69% strain. Misorientations measured between the regions marked, using STEM microdiffraction, are:-

A-B = 1.9°

B-C = 1.9°

A-C = 0.3°

B-D = 2.1°

E-F = 2.1°

F-G = 2.2°

E-G = 0.4°

F-H = 1.7°

A
B
C
D
H
E
F
G
{111} trace
0·2 μ

Fig. 3.20

Slip lines on a polished longitudinal section of a copper crystal, 5% strain.

Fig. 3.21

Slip lines on a polished longitudinal section of a crystal of alloy L, 5% strain.

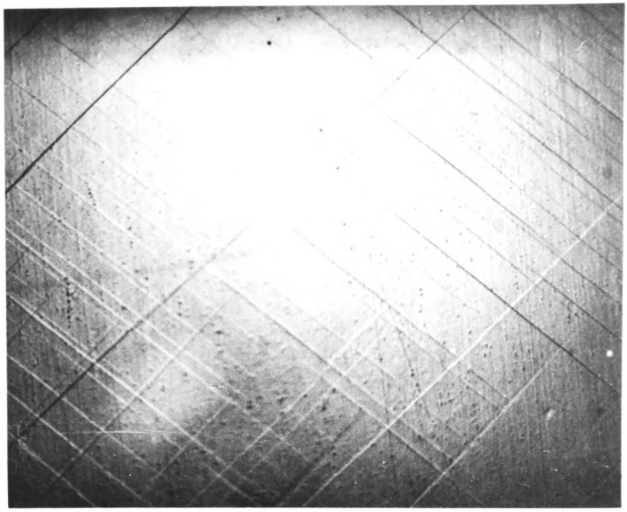

100μ

100μ

Fig. 3.22

Slip lines near the centre of a polished longitudinal section of a copper crystal, 11% strain.

Fig. 3.23

Slip lines near the surface of a polished longitudinal section of a copper crystal, 11% strain.

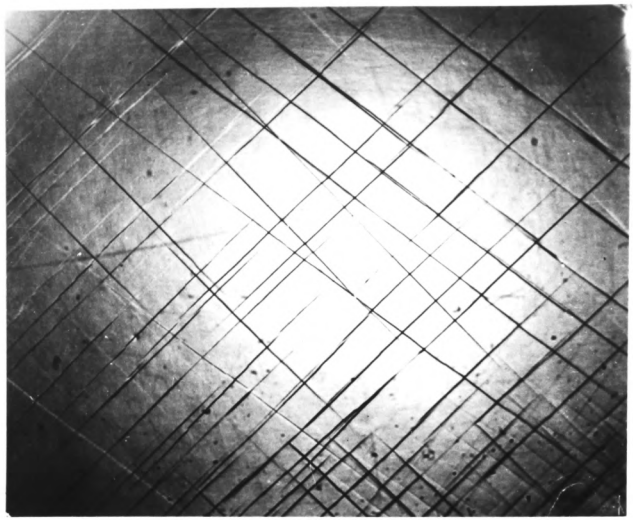

100μ

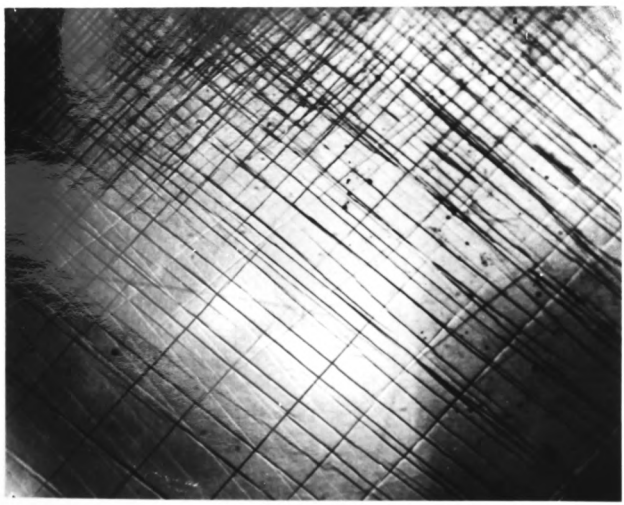

100μ

Fig. 3.24

Slip lines on a polished longitudinal section of a copper crystal, 20% strain.

Fig. 3.25

Curved slip lines on a polished longitudinal section of a copper crystal, 36% strain.

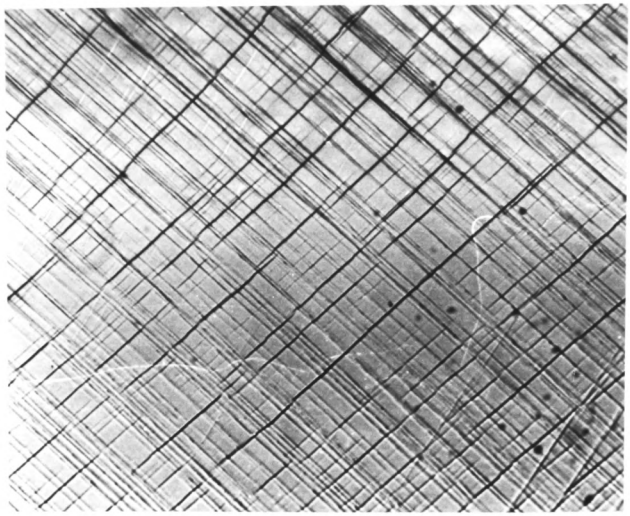

100 μ

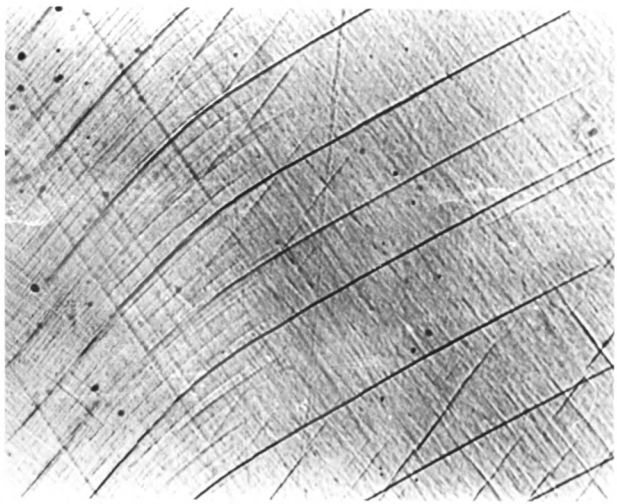

50 μ

Fig. 3.26

Alloy L, 5% strain.

Fig. 3.27

Alloy L, 5% strain.

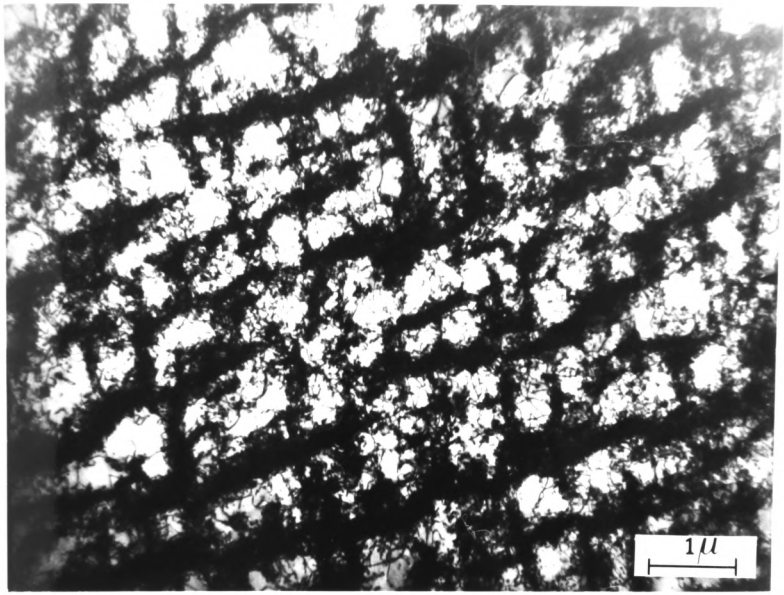

{111} trace
& R Ptrace

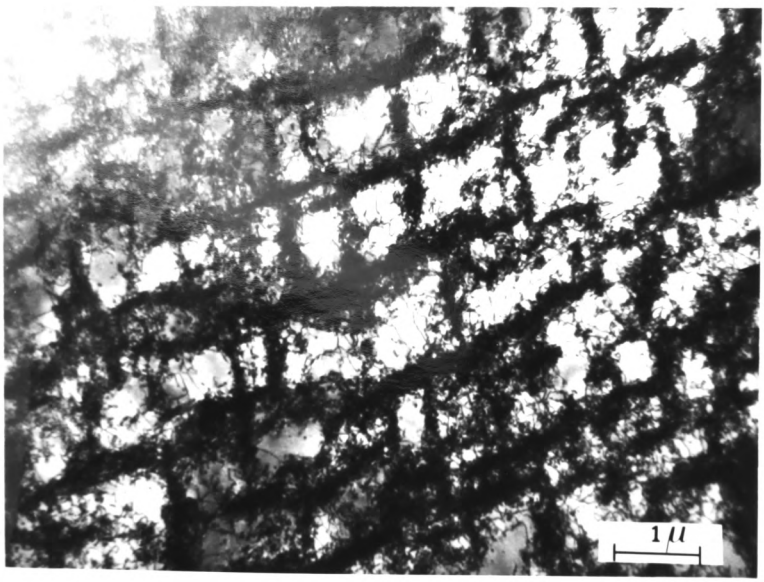

Fig. 3.28

Alloy L, 11% strain.

Fig. 3.29

Alloy L, 5% strain. Structure observed in 100keV TEM.

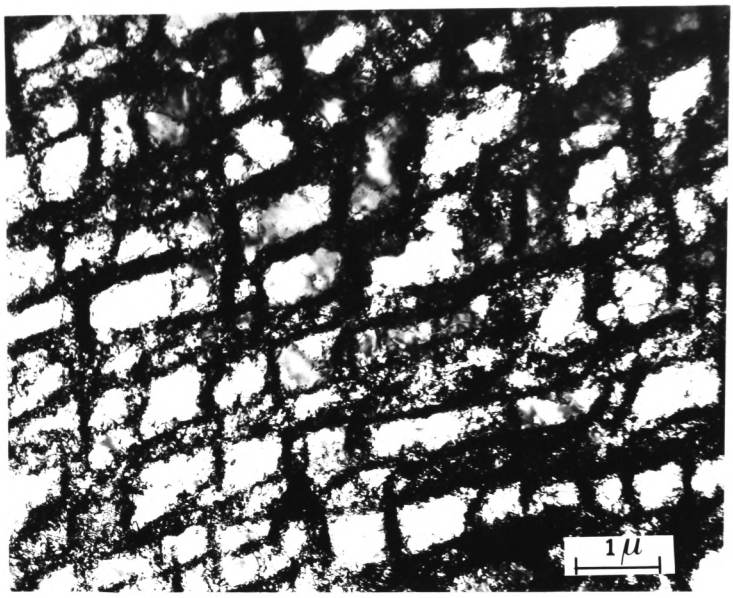
1μ


{111} trace
g {111}

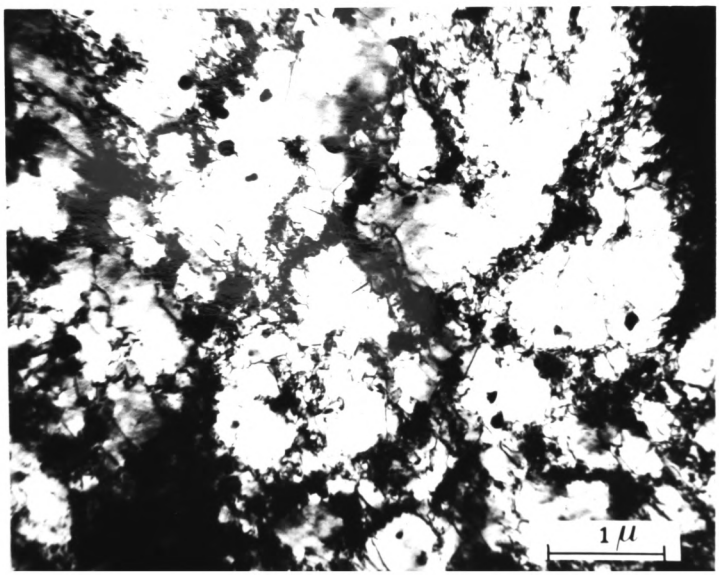
1μ

Fig. 3.30

Cell boundary in alloy L, 11% strain.

Fig. 3.31

Microband in alloy L, 11% strain.

g[111]
(111)trace
0·5μ

g[111]
(111) trace
0·2μ

Fig. 3.32

Alloy L, 20% strain.

Fig. 3.33

Alloy L, 36% strain.

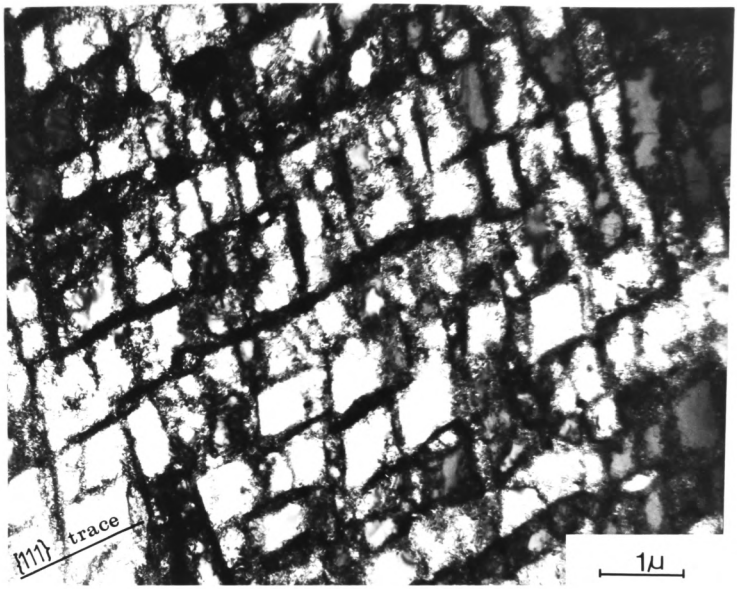
{111} trace
1μ

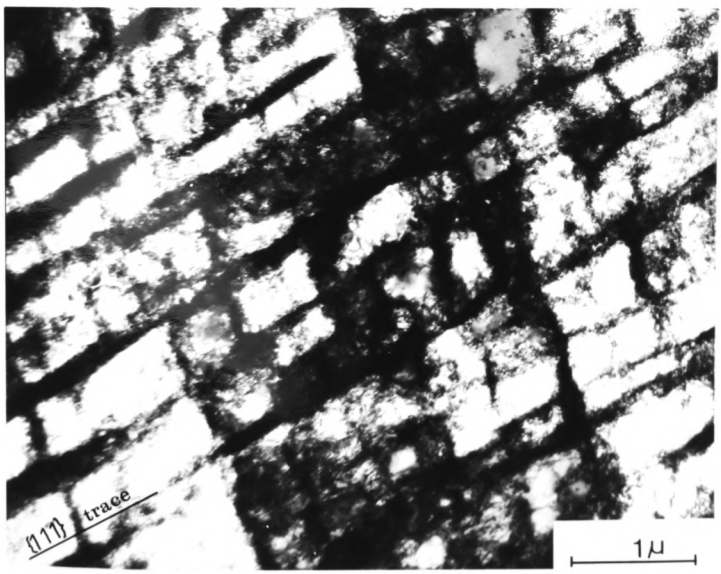
{111} trace
1μ

Fig. 3.34

Alloy L, 69% strain.


{111} trace
0·2 μ

Fig. 3.35

Alloy L, 69% strain.

Graph shows misorientations measured, using STEM microdiffraction, between points marked (dashed line) and the cumulative misorientation relative to 1 (full line).

foil trace
0·2 μ
2
3
4
5
6
7
8
9

MISORIENTATION (DEGREES)
6
4
2
1
2
3
4
5
6
7
8
SUBGRAIN NO.

Fig. 3.36

Structure observed in RP foil of alloy L at 69% strain.

Fig. 3.37

Alloy L, 69% strain.

The misorientation between the Transition band (T) and the homogeneous banded structure, measured from SAD patterns, is 12^{o}.

1μ

{111} trace
{111} trace
1μ

Fig. 3.38

Alloy L, 69% Strain.

The misorientations between the transition band, T and A and B, measured from SAD patterns, are 17.5° and 26° respectively. A and B differ by only 8.5°.

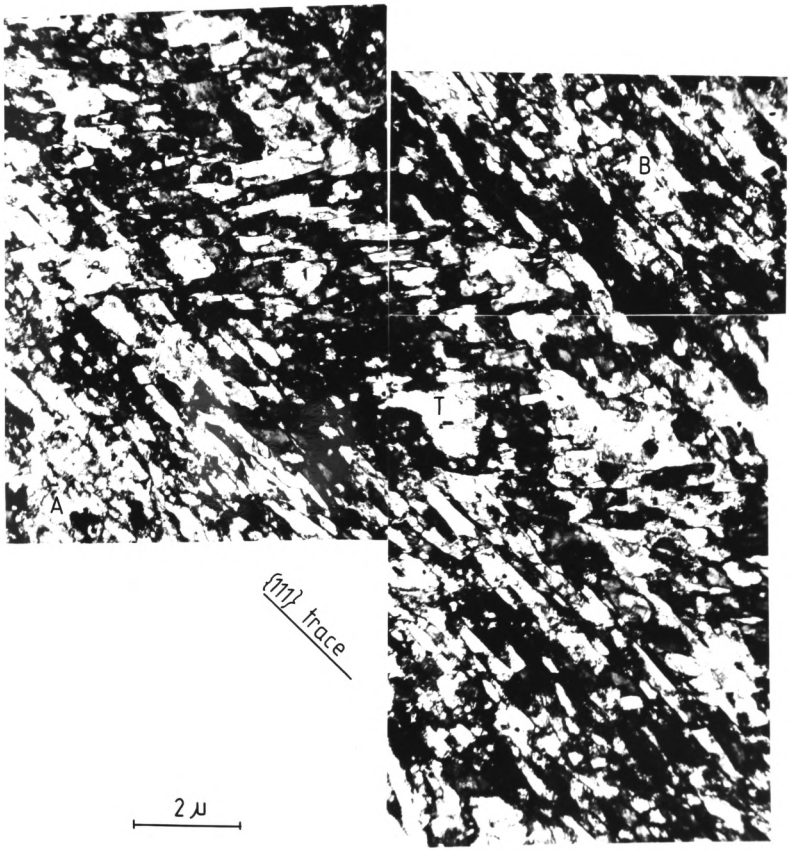
A
T
B
{111} trace
2 μ

Fig. 3.39

Schematic representation of the deformation structure observed in a longitudinal section of alloy L at 69% strain.

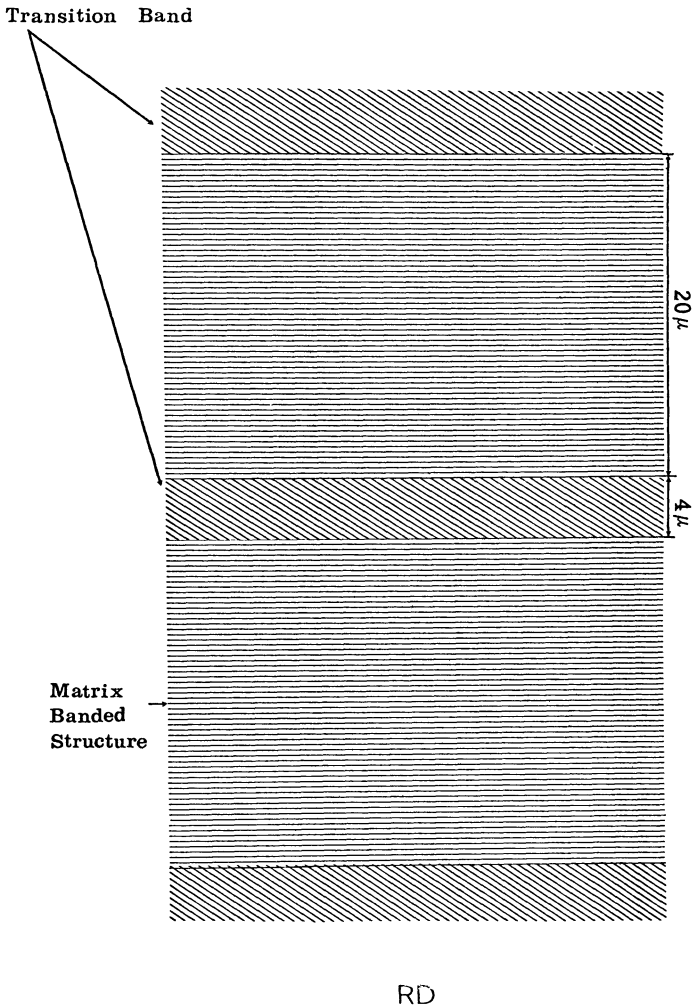
Transition Band
20μ
4μ
Matrix
Banded
Structure
RD

Fig. 3.40

Alloy L, 69% strain. Structure observed in a TD foil.

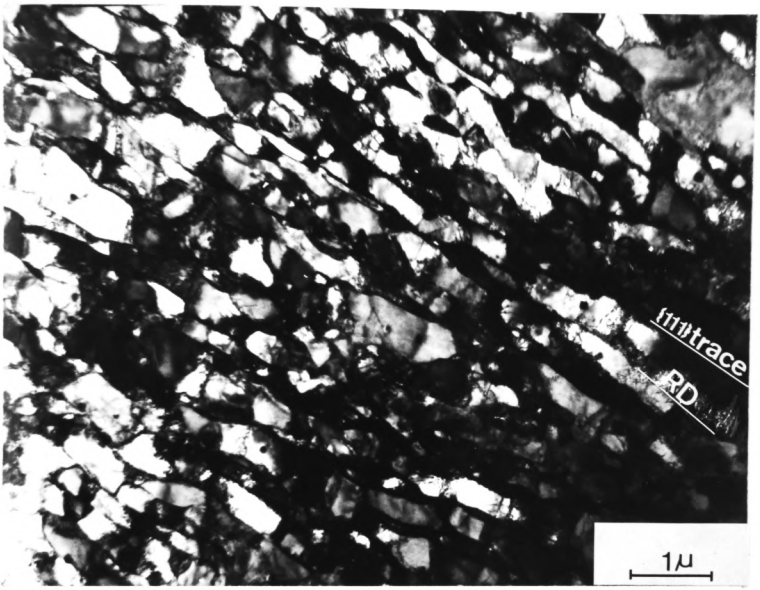
{111}trace
RD
1μ

Fig. 3.41

Alloy H, 5% strain.

Fig. 3.42

Alloy H, 5% strain.

(111) trace
1μ

(111) trace
0·5μ

Fig. 3.43

Alloy H, 11% strain.

(111) trace
0·25 μ

(111) trace
1μ

Fig. 3.45

Alloy H, 20% strain.

Fig. 3.46

Alloy H, 20% strain.

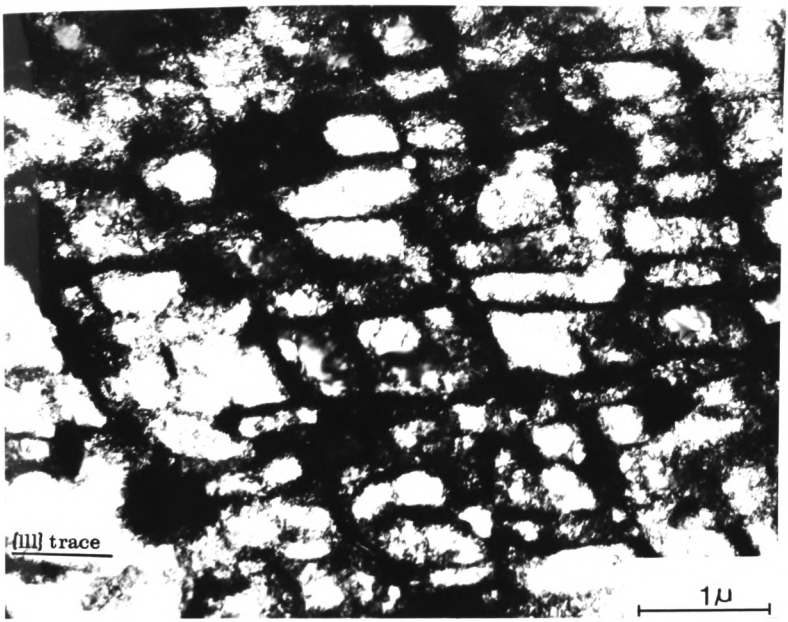
{111} trace
1μ

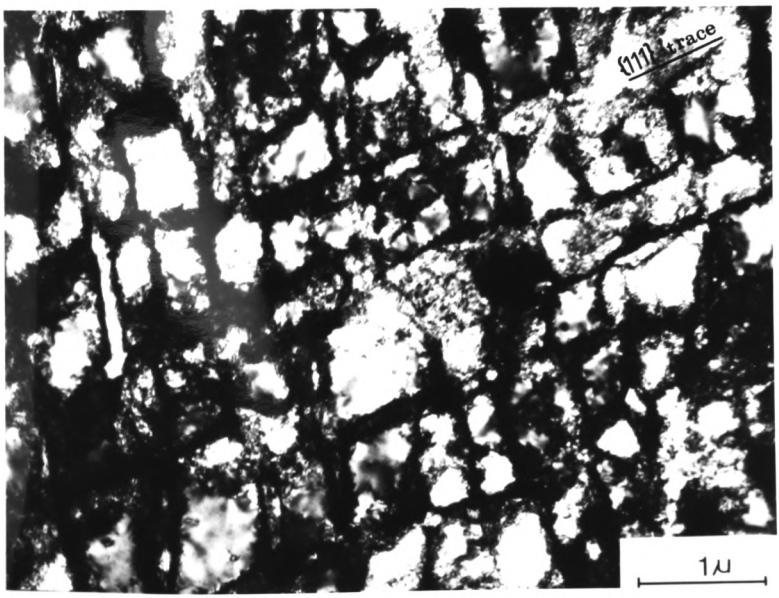
{111} trace
1μ

Fig. 3.47

Alloy H, 36% strain.

Fig. 3.48

Alloy H, 36% strain.

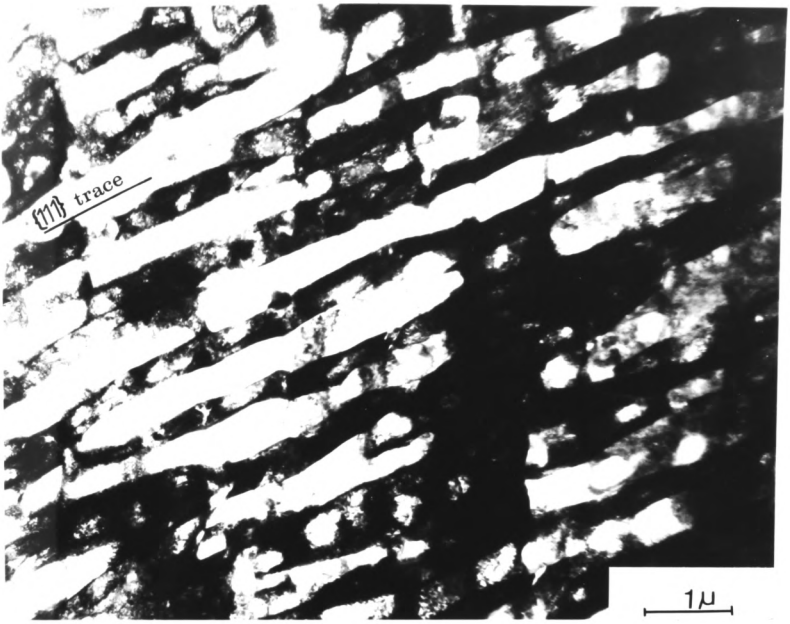
{111} trace
1μ

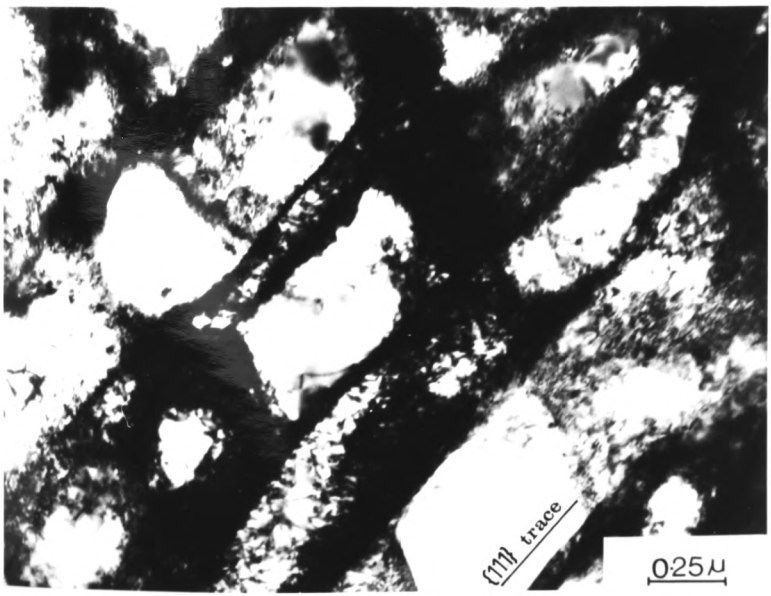
{111} trace
0·25μ

Fig. 3.49

Alloy H, 5% strain.

Shows the change of cell structure with thickness of foil.

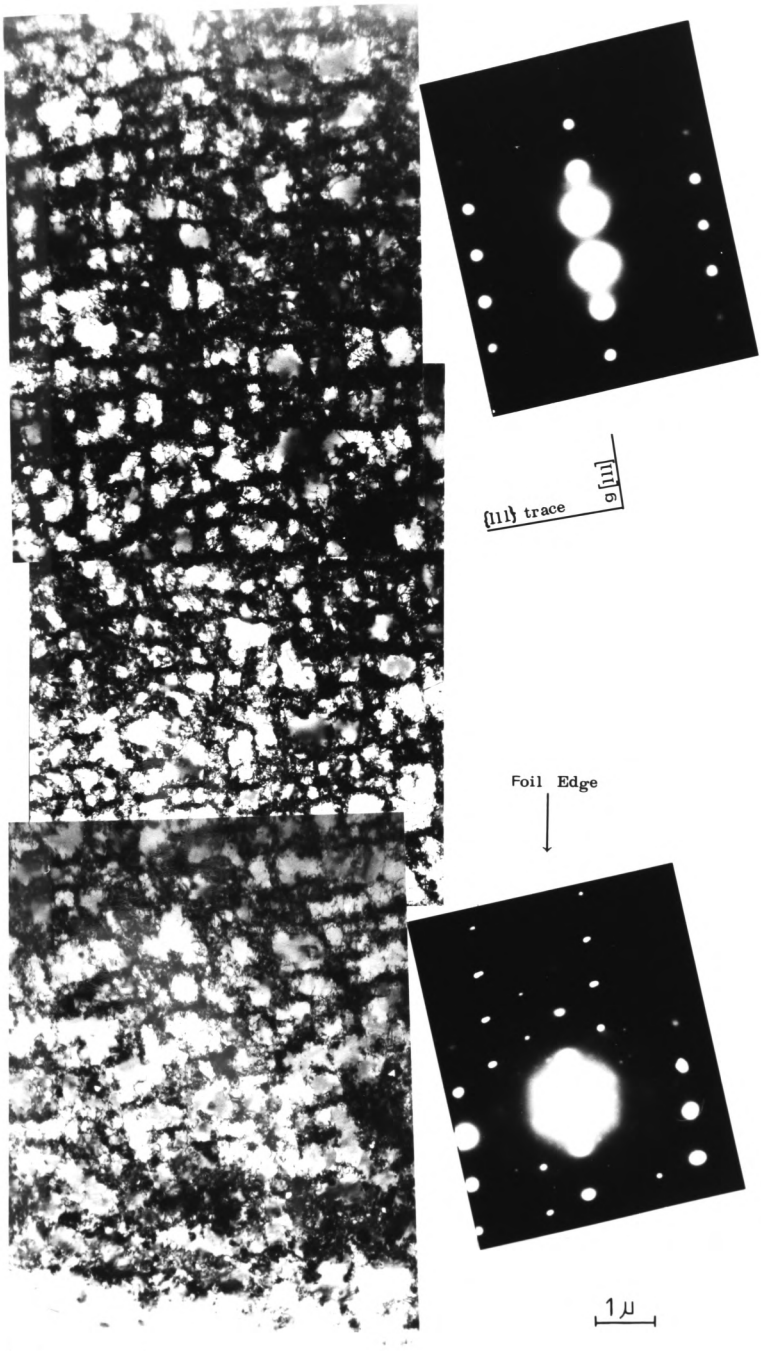
{111} trace
g [111]
Foil Edge
1 μ

Fig. 3.50

Shows a Transition band at T in alloy H at 69% strain.


T
RP trace
1 μ

Fig. 3.51

(110)[1$\bar{1}$2] copper crystal, 69% strain.

Fig. 3.52

Same specimen as above but nearer the foil's edge.

0·5 μ

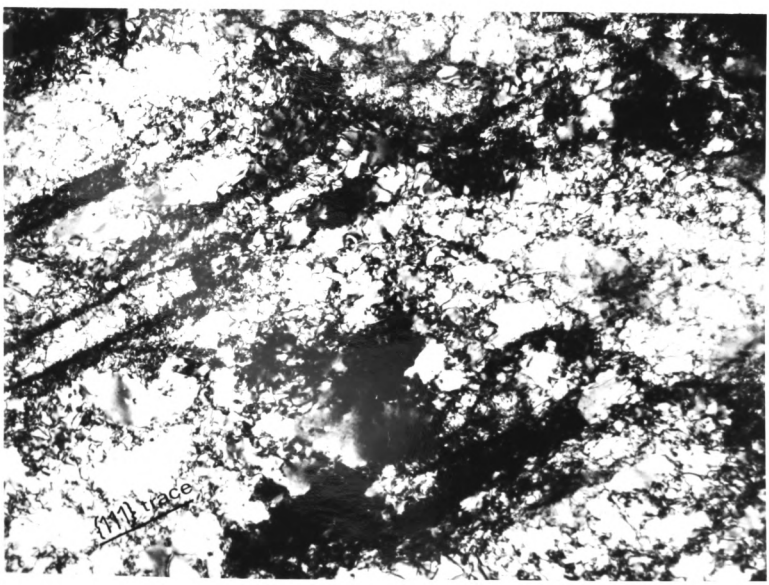

Fig. 3.53

Alloy M, 69% strain.

Fig. 3.54

Microbands in alloy M at 69% strain.

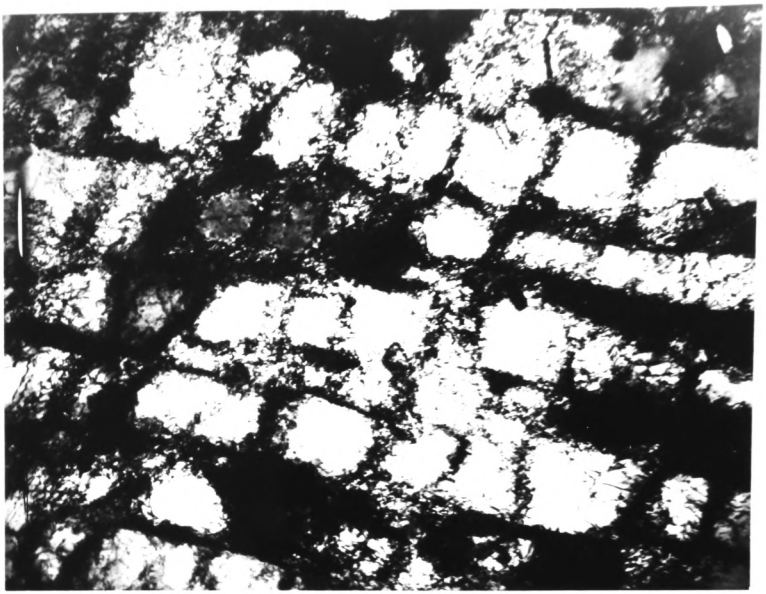

0·5 μ

RP trace

Fig. 3.55

Graph of hardness versus strain for rolled (111)[1$\bar{1}$0] crystals.

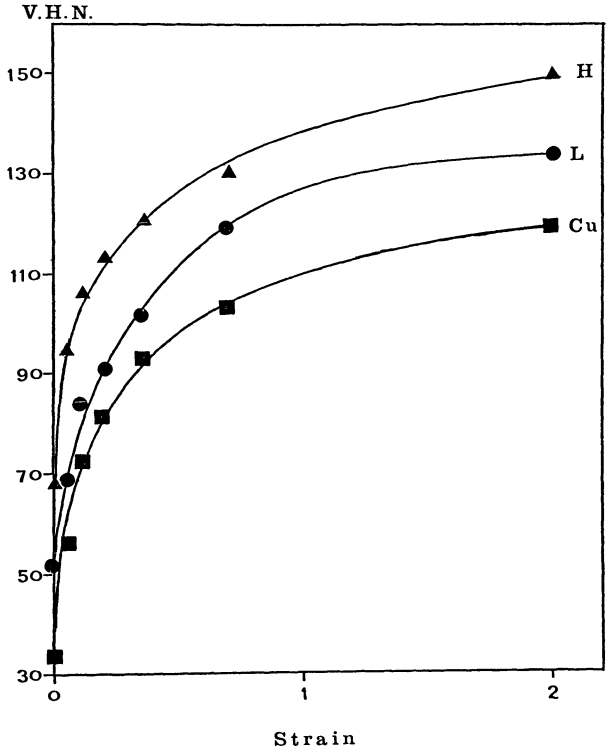
V.H.N.
150
130
110
90
70
50
30
0
1
2
Strain
H
L
Cu

Fig. 3.56

Relationships between true stress and true strain (●); hardness and true strain (O); subgrain size and true strain (▲).

(After Wingrove, 1972).

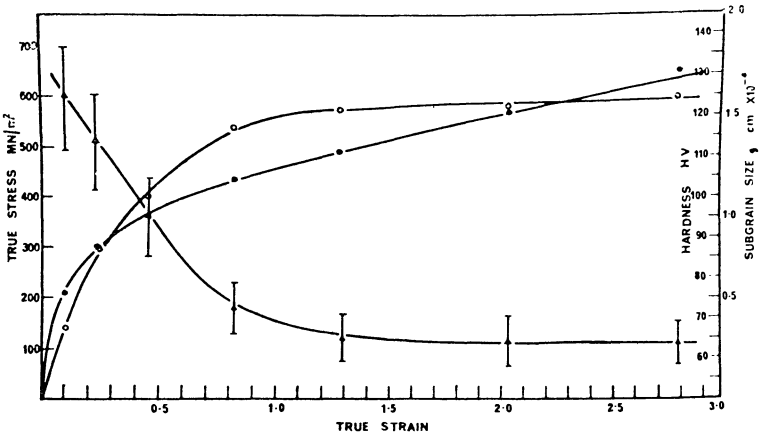
TRUE STRESS MN/m²
HARDNESS HV
SUBGRAIN SIZE δ cm X10⁻⁴
TRUE STRAIN
100
200
300
400
500
600
700
60
70
80
90
100
110
120
130
140
0·5
1·0
1·5
2·0
0·5
1·0
1·5
2·0
2·5
3·0

Fig. 3.57

Graph of hardness versus reciprocal cell dimension.

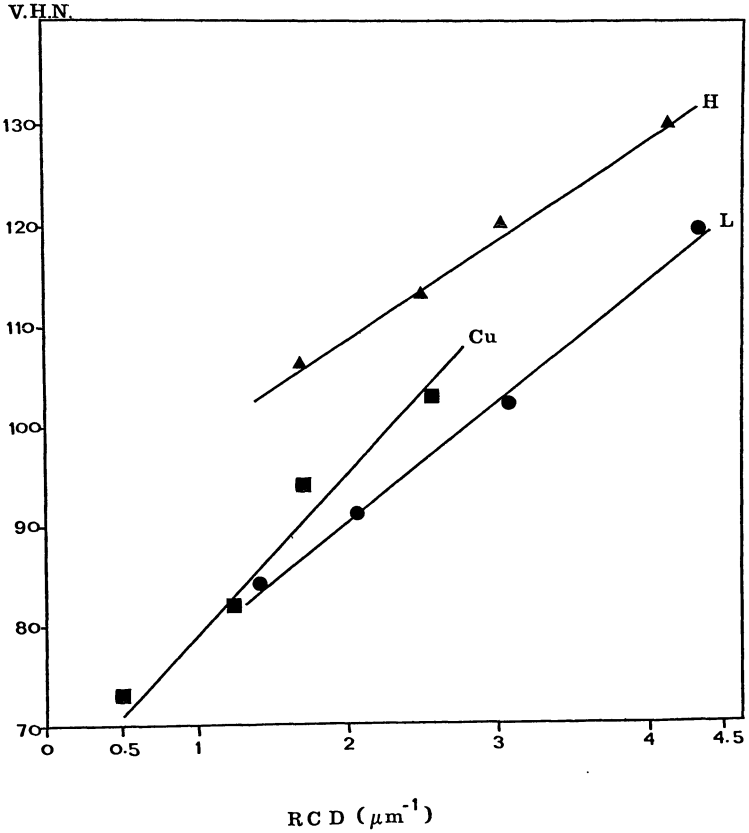
V.H.N.
130
120
110
100
90
80
70
0
0.5
1
2
3
4
4.5
H
L
Cu
RCD (μm^{-1})

Fig. 3.58

Graph of cell size versus strain.

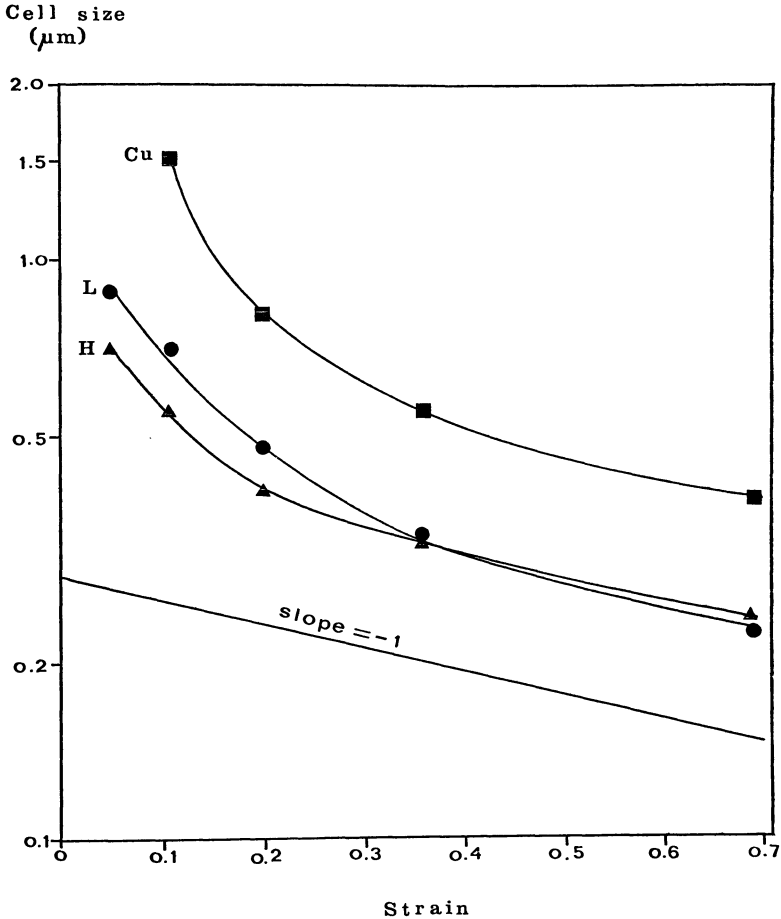
Cell size
(μm)
2.0
1.5
1.0
0.5
0.2
0.1
Cu
L
H
slope = -1
0
0.1
0.2
0.3
0.4
0.5
0.6
0.7
Strain

Fig. 3.59(a) & (b)

Nuclei in alloy M, 204% strain.

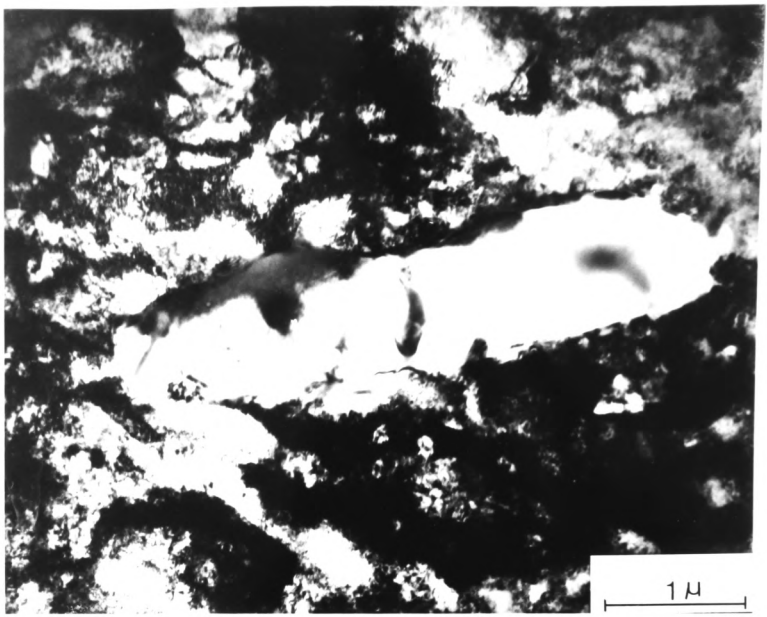
1 μ

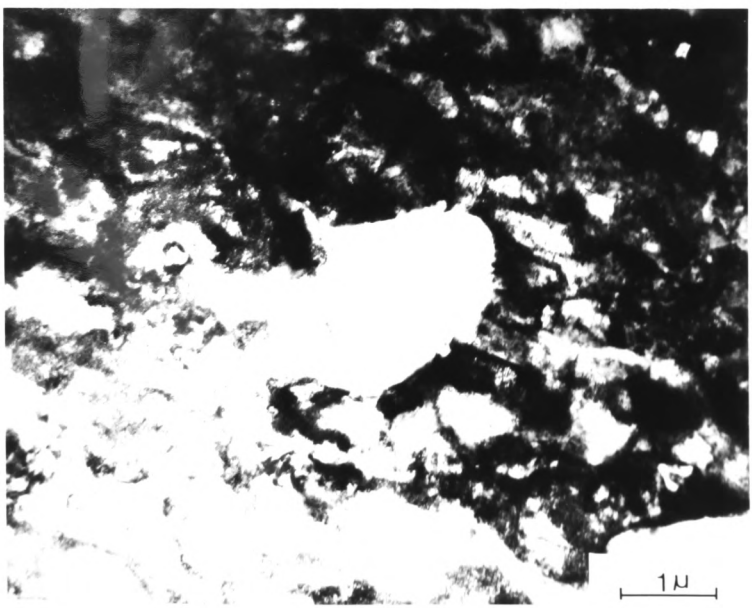
1 μ

Fig. 3.60

Schematic diagram of the cell structure observed in a longitudinal section of a copper-alumina alloy at 5% strain.

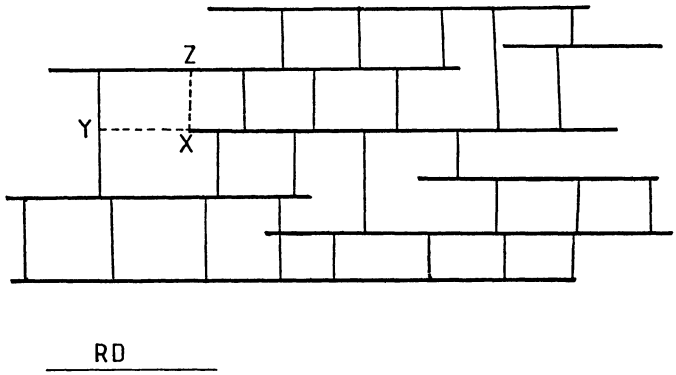
Z
Y
X
RD

Chapter 4

Stored Energies and Recrystallization Kinetics

Introduction

The experimental techniques and considerations involved in determining stored energies are outlined. The values of the stored energy and recrystallization temperature for the materials examined in Chapter 3 and for (111)[1$\bar{1}$0] crystals of copper and copper-alumina (alloys L & H) deformed to a true strain of 204% are presented. The results for the single phase material are discussed and compared to results found by other workers. The results for the two-phase material are discussed in Chapter 5.

4.1 Stored Energy Measurements

There are two principal methods of measuring the stored energy of cold work:-

i) Deformation Calorimetry in which the stored energy is calculated from the difference between the instantaneous heat evolution and the applied work (from the stress-strain data).

ii) Annealing Calorimetry in which the deformed specimen is annealed and the stored energy is measured on its release.

Other methods include solution calorimetry the main difficulty of which is the evolution of a large enthalpy of solution which masks the much smaller release of the stored energy of cold work. Ticknor and Bever (1952) overcame this difficulty by using liquid tin as a solvent. Bahk and Ashby (1975) have used two novel methods to

determine the stored energy of deformation of a heavily drawn internally oxidised copper-beryllium wire. One involved measuring the depression of the melting point (due to the retained stored energy) and the other the shape instability of the wire during annealing. However, the methods gave poor comparison, yielding values for the stored energy of 39 and 12.4 J/mole respectively.

4.2 Experimental Techniques

The present work utilizes annealing calorimetry in the form of anisothermal differential scanning calorimetry. This involved heating both a deformed specimen, whose stored energy is to be determined, and a reference specimen at a constant rate. The specimens were 5mm in diameter and varied in height and weight depending upon the degree of deformation. The specimens were spark machined from the rolled crystals described in section 2.6 and were then etched in nitric acid to remove any spark machine damage. The reference was a fully recrystallized sample of the same mass. Slight differences in mass between specimen and reference, which produce differences in thermal capacity, could be compensated for electronically.

Stored energies and the temperatures at which they were released were measured using two different machines. These were slightly different in their principle of operation and so are described separately below.

4.2.1 Perkin-Elmer DSC-2

This consists of two identical cylindrical platinum furnaces approximately 10mm in diameter. They sit in a refrigerated chamber and nitrogen is passed through the system. The specimen was placed in one furnace and the reference in the other.

The two furnaces were heated at a constant rate of 20 K/min. The difference in the power required to heat the two furnaces was automatically plotted as a function of temperature. When the specimen recrystallizes less power is required to heat the furnace in which it sits. This is seen in the graphical output as a peak. A typical example is shown in fig. 4.1.

Ideally if no heat output occurs from the specimen the graph of power difference against temperature should be a horizontal straight line. In practice this line may slope and curve. This can be electronically compensated for over a small temperature range. In addition, differences in the position of the specimens in their furnaces and how the lid of the furnace is sitting can lead to variations in slope and curvature of the graphical output. To overcome the above difficulties, the fully recrystallized specimen is rerun against the reference. This output is subtracted from the first run. The difference between the two i.e. the area under the peak, see fig. 4.1, represents the stored energy.

To obtain the stored energy and recrystallization temperature accurately the instrument has to be calibrated. This is done by heating samples of lead, zinc and indium whose enthalpy of melting and melting temperature are known; an example is shown in fig. 4.2. The actual melting temperature of the above were then plotted against

their measured melting temperature. The difference between the two was found to be negligible. The stored energy of deformation was found using the formula below:-

$$\Delta H_s = \frac{kRA}{WS} \qquad (4.1)$$

or

$$\Delta H_s = \Delta H_I \times \frac{W_I}{W_s} \times \frac{R_s}{R_I} \times \frac{S_I}{S_s} \times \frac{A_s}{A_I} \qquad (4.2)$$

where ΔH - Transition energy (calories/gm.)

R - Range Sensitivity (calories/sec.)

A - Peak area.

W - sample weight (gm)

S - Recorder chart speed (mm/sec)

k - Instrument Constant

where s refers to the specimen and I refers to the reference, in this case, indium.

The shape of the peak using this technique is not a fundamental property as the slope of the leading edge is a function of the heating rate due to the machine's thermal resistance. The sample size can also change the position of the peak. Fig. 4.3 shows the effect of increased sample size on a theoretical peak and how the transition temperature is defined for a sharp transition.

4.2.2 Du Pont Thermal Analyser

In this equipment both the reference and the specimen are heated in the same platinum furnace, through which nitrogen is passed, but they are placed on top of separate thermocouples. The furnace is heated at a constant rate and the thermocouples measure the temperature difference between the sample and the reference. If a heat related change takes place the sample temperature either leads (evolves heat) or lags (absorbs heat) the reference's temperature. The temperature difference between sample and reference from such a heat change is related to the differential heat flow. The machine is precalibrated and the heat flow and temperature are recorded at the maximum sensitivity by a microcomputer.

A typical graph of heat flow against temperature is shown in fig. 4.4. The specimen is not rerun as in the Perkin-Elmer but the beginning and end points of the curve are joined by a straight line and the area under the peak is calculated and displayed together with the peak and 'transition' temperature automatically. The stepped nature of the curve in fig. 4.4 is because the apparatus was used to measure comparatively small quantities and each step is due to the digital recording of the computer.

4.2.3 General Observations

The following remarks apply to both pieces of apparatus.

A nitrogen atmosphere was used in both the Perkin-Elmer and the Du Pont apparatus but oxidation of the copper was rapid above 500°C. The heat output from oxidation is much larger than the stored energy

of deformation and so, once oxidation occurs, the latter's measurement becomes impossible. It was found that although both machines were supposed to work up to 725°C their performance above 500°C was poor and that even on heating empty furnaces above this temperature a straight, horizontal, noise-free baseline could not be obtained. This meant that using continuous heating, the stored energy of the specimen deformed to lower strains could not be determined.

The stored energies measured were in the range 10-60 J/mole whereas the apparatus is usually used for the determination of phase transformation energies in which the transition energy would be greater than 1 KJ/mole. Thus in the present work, the machines were working on very sensitive ranges and noise was a problem.

Heating the sample slowly meant that the stored energy was evolved slowly over a long time and thus the peak is long and flat and merges into the noise level. Rapid heating meant a sharper peak but meant that a less sensitive recording range must be used and that the peak does not occur until a higher temperature; thus one is limited by the equipment's temperature range. Therefore a compromise heating rate of 20 K/min was used. The noise problem is also the reason isothermal experiments were not conducted. One needs to carry out the isothermal anneal at a temperature at which the stored energy will be released within about five minutes. This means that all specimens cannot be recrystallized at the same temperature. Thus a comparison of recrystallization kinetics between different specimens is not possible and the lower deformations still need to be recrystallized at higher temperatures.

In determining the stored energy by annealing calorimetry, two fundamental and unavoidable sources of error occur:-

(i) The internal stored energy, ΔU, is approximately equal to the enthalpy, ΔH, since at constant pressure the volume change in a metal is negligible so that the $P\Delta V$ term of equation 4.3 can be ignored:-

$$\Delta H = \Delta U + P\Delta V \qquad (4.3)$$

The Gibbs free energy of cold work is thus:-

$$\Delta G \simeq \Delta U - T\Delta S \qquad (4.4)$$

The configurational and vibrational entropy due to dislocations has been shown, by Cottrell (1953), to be negligible at ordinary temperatures. The entropy term due to point defects can be large: however vacancies do not contribute greatly to the energy in most metals at room temperature. Thus, measuring the stored energy is a very good approximation to the free energy of cold work.

ii) An error also arises since the release of energy during annealing does not return the metal to the lowest energy state i.e. the single crystal state. After annealing, some energy remains in the crystal as internal surfaces i.e. grain boundaries. However, this retention of some of the stored energy of deformation will have a negligible effect on the measured stored energy value.

A further error arises in anisothermal annealing methods, such as those used here. In anisothermal methods the stored energy of cold work is determined from the difference between the amounts of heat required to raise a cold-worked and annealed specimen through the same temperature interval. Bever, Holt and Titchner (1973) state that this difference does not result from a difference in the true heat capacities of the cold-worked and annealed specimens; heat capacities

apply to reversible changes, but an irreversible change takes place in the cold-worked specimens during heating. This gives rise to only a small error in the values obtained. However, the heat capacity of the cold-worked metal is probably less than 0.15% larger at room temperature and falls as the temperature rises.

4.3 Results

All the stored energies and recrystallization temperatures below are from measurements of a single peak and are an average of between three and five values.

4.3.1 (110)[1$\bar{1}$2] Crystals

The stored energy and recrystallization temperature were measured for the 50%-rolled (Strain=69%) (110)[1$\bar{1}$2] copper crystals and similar specimens containing alumina particles produced by internal oxidation at 1000°C (alloy M). Also, copper specimens, which had undergone the same internal oxidation treatment as the copper-alumina were compared. The results are shown in table 4.1.

Table 4.1 (110)[1$\bar{1}$2] Single Crystals -50% rolled

Material	Pure Cu	I.O.Cu	Cu-Al_2O_3 (alloy M)
Stored Energy (J/mole)	22	22	43
Rex. temp (°C)	403	373	281

The particle-containing material has a much higher stored energy and lower recrystallization temperature than the single phase. The

internal oxidation treatment appears to have no noticeable effect on the stored energy, however the recrystallization temperature is reduced.

The isothermal recrystallization kinetics of these three materials have also been investigated at 350°C by the method described in section 2.7. The results are shown in fig. 4.5. These confirm the results obtained from the continuous heating experiments. The grain sizes of the copper-alumina were smaller than the copper whilst the copper and internally oxidised copper had similar grain sizes.

The acceleration of recrystallization found in the copper-alumina compared to the untreated copper is partly due to the internal oxidation treatment. However, the acceleration of recrystallization by small particles is a real effect as the copper-alumina alloy is still accelerated when compared to the internally oxidised copper. Since the particle-containing material has to undergo the internal oxidation treatment and because this treatment affects even pure copper, subsequent experiments have used internally oxidised pure copper for comparison with copper-alumina rather than untreated pure copper.

4.3.2 $(111)[1\bar{1}0]$ Crystals

The recrystallization temperatures and stored energies of 50%-rolled (Strain=69%) specimens of copper (untreated), copper internally oxidised at 1000°C and copper internally oxidised at 900°C were determined, the values are shown in table 4.2.

Table 4.2 (111)[1$\bar{1}$0] Single Crystals 50% rolled

Material	Pure Cu	Cu I.O. @ 1000°C	Cu I.O. @ 900°C
Stored Energy (J/mole)	18	18	18
Rex. temp. (°C)	387	348	352

The effect of the internal oxidation treatment in lowering the recrystallization temperature is again demonstrated, and again no difference in stored energy was found between the oxidised and unoxidised copper. The temperature of internal oxidation seems to make a minor difference to the subsequent recrystallization temperature. The difference found is within the experimental error.

The stored energies and recrystallization temperatures of internally oxidised copper and two copper-alumina alloys (L,H) were measured at strains of 5, 11, 20, 36, 69 and 204%; the results are shown in table 4.3. Owing to the experimental limitations described in section 4.2, the values for the 20% strained alloy H and the 11% and 20% strained internally oxidised copper could not be measured. However, it was found empirically that, at the heating rate used, the recrystallization temperature corresponded to a temperature at which recrystallization was just complete in five minutes. Thus the recrystallization temperatures in table 4.3 for the above three materials are the temperatures at which recrystallization is just complete in five minutes and are presented for comparison.

Both copper-alumina alloys when rolled to only 5% and 11% strain and internally oxidised copper 5%-strained were not found to recrystallize on annealing. However, recovery occurred at higher

temperatures in these materials.

Table 4.3 (111)[1$\bar{1}$0] Single Crystals

True Strain (%)	Deformation (rolling reduction)	Material	Stored Energy (J/mole)	Rex. Temp. (°C)
204	87%	Cu-Al_2O_3 (L)	57	181
204	87%	Cu-Al_2O_3 (H)	59	218
204	87%	I.O. Cu	44	254
69	50%	Cu-Al_2O_3 (L)	26	287
69	50%	Cu-Al_2O_3 (H)	49	278
69	50%	I.O. Cu	18	348
36	30%	Cu-Al_2O_3 (L)	15	350
36	30%	Cu-Al_2O_3 (H)	34	345
36	30%	I.O. Cu	12	424
20	18%	Cu-Al_2O_3 (L)	13	382
20	18%	Cu-Al_2O_3 (H)	-	600
20	18%	I.O. Cu	-	470
11	10%	I.O. Cu	-	520

4.4 Discussion

4.4.1 The Internal Oxidation Effect

That internal oxidation can affect the properties of copper single crystals has been noted by Ebeling and Ashby (1966). They found that the tensile stress-strain curve of a copper single crystal was modified by internal oxidation, see fig. 1.3.

Haessner, Hoschek and Tölg (1979) also found that internal oxidation lowered the recrystallization temperature of 98%-rolled, (110)[1$\bar{1}$2], 99.9998%-pure copper single crystals, see table 4.4, by a similar amount to that found here. They also found that similar single crystals which contained alumina (whose dispersion parameters were not determined) still showed acceleration when compared with internally oxidised copper. Their stored energy results differ from those found in the present work in that a large increase in stored energy was found after internal oxidation of pure copper (15J/mole) even larger than the increase (10J/mole) due to the addition of the alumina particles. It is hard to envisage the origin of such a large increase in stored energy in the internally oxidised copper.

Table 4.4 (110)[1$\bar{1}$2] copper single crystals 98% rolled (After Haessner, Hoschek and Tölg, 1979)

Material	Stored Energy (J/mole)	Rex. temp. (^{o}C)
Cu-0.236 At% Al I.O. @ 900^{o}C	62	202
I.O. Cu	67	216
Pure Cu	52	255

They ascribed the acceleration of recrystallization by internal oxidation as due to the gettering of any residual solute.

Analyses of the copper single crystals used in the present work were commissioned; these indicated that solute levels were below the levels of detection. However, even small amounts of solute can have a large effect on the recrystallization kinetics, e.g. table 1.3.

Thus, the explanation of the reduced recrystallization temperature in the internally oxidised copper must be, in the absence of any differences in dislocation structure, due to the gettering of any residual solute, as proposed by Haessner et al. (1979). The solute will be removed from solution and form very small, widely-spaced particles. These will be so small in size and few in number that they will have a negligible effect on the stored energy and dislocation structure compared to pure copper.

The internal oxidation effect means that the previous work on the recrystallization kinetics of internally oxidised alloys reviewed in section 1.5.3 should have used internally oxidised copper as a control and not untreated copper. This means that the changeover from

acceleration to retardation with respect to the pure material would be shifted, although the relative rates of recrystallization of alloys of different dispersion parameters are, of course, unchanged.

4.4.2 The Orientation Dependence of Recrystallization and Stored Energy

The orientation dependence of the stored energy of deformation and the recrystallization kinetics have been investigated by several workers, often in copper.

Brown and Hatherly (1970a) using 98.8%-rolled copper single crystals found large differences in recrystallization rate with orientation; crystals with only small deviations from (110)[1$\bar{1}$2] and (111)[$\bar{1}\bar{1}$2] orientations were the slowest to recrystallize. They found that for the (110)[1$\bar{1}$2] orientation, deviations from the exact orientation gave rise to marked changes in the recrystallization rate but that deviations from the exact orientation in (111)[1$\bar{1}$0] crystals led to much smaller changes in recrystallization rate, see table 4.5.

Table 4.5

Recrystallization data for 98.6% rolled copper-single crystals annealed at 300°C. (After Brown and Hatherly (1970a))

Nominal Orientation	Misorientation (deg.)		Recrystallization Time.(min.)	Recrystallized Grain Size (mm)
	Plane	direction		
(111)[1$\bar{1}$0]	2	4	100	0.002-0.0016
(111)[1$\bar{1}$0]	5	1	1000	0.002-0.012
(110)[1$\bar{1}$2]	8	1	60	0.020-1.0
(110)[1$\bar{1}$2]	<1	<1	>1000	0.5-1.0
Polycrystal	-	-	1	0.002-0.020

The table also shows that the polycrystalline recrystallization time is markedly faster than that for single crystals. Brown and Hatherly (1970b) also studied the rolling textures of the single crystals but could find no significant features that pointed to the definition of a `fast' or `slow' texture which could be used to predict relative recrystallization rates.

They compared their recrystallization times for (110)[1$\bar{1}$2] copper single crystals with those found by other workers, see table 4.6, and concluded that the results of different workers are difficult to compare since crystals may have different solute contents and different deviations from the exact orientation. They suggested, however, that the differences in recrystallization rate could be due to differences in the length to thickness ratio of the crystals

investigated since the crystals with smaller ratios had a higher density of inhomogeneities near the surface.

Table 4.6

Recrystallization of (110)[1$\bar{1}$2] crystals. (After Brown and Hatherly (1970a))

Investigation	Misorientation (deg.)		Reduction	Recrystallization Time @ 300°C (min.)	Length-Thickness Ratio
	Plane	direction			
Hibbard and Tully (1961)	2	2	95	10	1.7
Liu and Hibbard (1953)	2	0	99.5	20	2.2
Brown and Hatherly (1970)	<1	<1	98.8	>1000	4.0
Brown and Hatherly (1970)	8	1	98.8	80	4.0

Haessner, Hoschek and Tölg (1979) have performed the only measurements of stored energies and recrystallization temperatures of rolled crystals of different orientations, see table 4.7. They also found that the (111)[$\bar{1}\bar{1}$2] orientation was the slowest to recrystallize in 98%-rolled copper.

Table 4.7

Stored energy and recrystallization temperature of 98%-rolled single crystals. (After Haessner, Hoschek and Tölg (1979))

Initial Orientation	Stored Energy (J/mole)		Recrystallization Temperature (°C)	
	Copper	Silver	Copper	Silver
(100)[001]	59		170	
	50		210	
(100)[011]	77		190	
(110)[001]	50		270	
(110)[1$\bar{1}$0]	42		153	
(110)[1$\bar{1}$1]	44		270	
(110)[1$\bar{1}$2]	52	85	255	182
		96		213
(111)[1$\bar{1}$0]	38	159	225	129
	29		270	
(111)[$\bar{1}\bar{1}$2]	40	120	300	160
(112)[1$\bar{1}$0]	84	167	120	125
(112)[$\bar{1}\bar{1}$1]	84	174	120	134
		188		132
(112)[0$\bar{2}$1]		152		123
(120)[2$\bar{1}$1]		145		113
(123)[0$\bar{3}$2]		161		125
(123)[$\bar{7}\bar{4}$5]	67		220	
polycrystal	47	138	169	122

However, they found that the (110)[001] and (110)[1$\bar{1}$1] orientations recrystallized slower than the (110)[1$\bar{1}$2] orientation in disagreement with the work of Brown and Hatherly (1970a). Comparing the orientations which were investigated in the present work they found that the (110)[1$\bar{1}$2] crystals had a larger stored energy than the (111)[1$\bar{1}$0] crystals. From measurements of several crystals of the (111)[1$\bar{1}$0] orientation they found two sets of values for the recrystallization temperature, one higher and one lower than the recrystallization temperature of the (110)[1$\bar{1}$2] crystals. They measured the stored energy and recrystallization temperature of ten single crystals each of the (112)[$\bar{1}\bar{1}$1] and (110)[1$\bar{1}$2] orientations and found little change in the recrystallization temperature or stored energy with variations in the rolling plane orientation of up to 5°. This is in direct conflict with the work of Brown and Hatherly (1970a).

The energy released on recrystallization, as measured both by Haessner, Hoschek and Tölg (1979) by anisothermal annealing and also in the present work, is the difference between the stored energy of deformation and the energy of recovery. The energy of recovery is fairly small compared to the total stored energy and has been found by Vandermeer and Gordon (1963) to decrease from 10% to 3% of the total stored energy as the strain was increased from 10% to 33% in tensile deformed polycrystalline copper.

Several workers have measured the stored energy of tensile deformed single crystals by deformation calorimetry. Bever, Holt and Titchner (1973) point out that stored energy values obtained from deformation calorimetry are always much higher than values obtained

from annealing calorimetry since they contain the energy of recovery and the energy which is released immediately after deformation, which can be 5-25% of the total energy. They also state that systematic errors can raise the stored energy value measured by this method. However, most workers using deformation calorimetry have found an orientation dependence of the stored energy e.g. Rönnpagel, Schulz, Hattendorf and Schwink (1979) in copper. An orientation dependence of the stored energy was also found by Gottstein, Bewerange, Mecking and Wollenberger (1975) using annealing calorimetry on tensile-deformed copper.

There are some irresolvable contradictions in the work surveyed above, particularly the effect of small variations in the orientation of crystals on the recrystallization temperature. The present work is, however, in agreement with most findings quoted above in that the present (111)[1$\bar{1}$0] copper single crystals have a lower stored energy and recrystallization temperature than the (110)[1$\bar{1}$2] crystals; Hibbard and Tully (1961) also found that the (110)[1$\bar{1}$2] orientation was the slowest to recrystallize of the four orientations investigated.

The present results and those of Haessner, Hoschek and Tölg (1979) indicate that a larger stored energy does not necessarily mean a lower recrystallization temperature.

Bailey and Hirsch (1960) and Bailey (1963) found that the stored energy increased linearly with the dislocation density, as determined by TEM, in tensile deformed polycrystals; although the reported values of the latter were only thought to be accurate to ±25% and to be consistently 20% low (due to dislocation loss and dislocations out of contrast). Thus a higher stored energy implies a higher dislocation

density and also that the crystal will be mechanically harder. A higher dislocation density in crystals of different orientations does not, however, mean that recrystallization will take place more rapidly; only that the average driving force is greater. The ease of recrystallization does not depend on the average properties such as the stored energies or dislocation density as much as the local properties i.e. how the dislocations are arranged. The average stored energy provides the driving force for recrystallization to proceed once nucleation has occurred. Nucleation, however, does not depend on the homogeneous cell structure found in metals but on the local deformation-produced inhomogeneities which will act as nucleation sites e.g. the (110)[1$\bar{1}$2] orientation in copper has been shown by Brown and Hatherly (1970b) not to form inhomogeneities such as transition bands until very high strains since the orientation is a stable one in rolling deformations.

The higher recrystallization temperature of the (110)[1$\bar{1}$2] crystals compared to the (111)[1$\bar{1}$0] crystals is, therefore, because of the lack of structural inhomogeneities produced during deformation which would act as nucleation sites; the large stored energy is thus of secondary importance and indicates only that a larger average dislocation density is present.

4.4.3 The Variation of Stored Energy with Strain

Bever, Holt and Titchner (1973) examined the data of several workers who measured the stored energy of deformation as a function of strain. The rate of stored energy increase was found to decrease as the strain increased for polycrystals, whilst for single crystals

deformed in tension the stored energy increase with increasing shear strain could be either upwardly concave or convex, depending upon the orientation.

Haessner and Hoschek (1976) have conducted the only investigation of stored energy as a function of rolling strain in single crystals. Their results for (112)[$\bar{1}\bar{1}$1] copper crystals, shown in fig. 4.6, show that the stored energy increased linearly with strain until high strains when a 'saturation' value of the stored energy was attained.

The values of stored energy measured for the various (111)[1$\bar{1}$0] crystals are shown as a function of strain in fig. 4.7. The values for copper and alloy L fit well on a straight line. The values for alloy H, which has a much larger particle content and a much larger stored energy for a given strain, do not lie on a straight line. The line drawn for alloy H presupposes that a saturation value of the stored energy has been reached, or is being approached, at the highest strain.

The stored energy E_s, as noted in section 4.4.2, arises principally from the dislocation density, ρ, so we may write:

$$E_s = \rho E_l \tag{4.5}$$

where E_l is the self energy per unit length of a dislocation i.e.

$$E_l = \alpha_s G b^2 \tag{4.6}$$

where G is the shear modulus and b the Burger's vector.

Bailey's (1963) value of α_s is approximately 4. Bever, Holt and Titchner (1973) note that most reported values of α_s lie between 2 and 3 for polycrystalline material as determined from relating the stored energy to the directly measured dislocation density. However, as the

latter is invariably an underestimate of the real value, then α_s must also be smaller. Taking α_s as 0.5, one can calculate the dislocation density from the stored energy values; the results are shown in table 4.8.

Bailey and Hirsch (1960) and Bailey (1963) noted that the flow stress, τ, was proportional to the square root of the dislocation density and subsequent work has supported the relation:-

$$\tau = \alpha G b \rho^{1/2} \qquad (4.7)$$

where α is approximately 0.5.

Tabor (1951) has shown that the Vickers hardness, H, at a strain ε_o is related to the flow stress, τ, at a strain $\varepsilon = \varepsilon_o + 8\%$ by the relation:-

$$H \simeq 3\tau \qquad (4.8)$$

At high strains, where the rate of work hardening is low and thus the metal approximates to ideal plastic behaviour, the flow stress can be reasonably estimated from the hardness at a strain 8% less than the strain at which the dislocation density is to be calculated. Using flow stresses determined from fig. 3.55 and using equation 4.8, the values of the dislocation density were determined from equation 4.7; the results are shown in table 4.8.

Table 4.8

Dislocation densities in single phase copper.

Strain, ε (%)	$\rho \times 10^{15} m/m^3$ from τ; eq(4.7)	$\rho \times 10^{15} m/m^3$ from E_S; eq.(4.5)	$\frac{\tau^2}{GE_S}$
36	2.46	1.12	1.10
69	3.28	1.68	0.98
204	4.59	4.10	0.56

Reasonable agreement is found between the two methods of estimating the dislocation density and values are similar to those found by other workers at similar deformations in copper.

Bailey (1963) found that a plot of E_S against τ^2/G gave a straight line fit for copper and silver as predicted by amalgamating equations 4.5, 4.6 and 4.7, i.e.

$$\frac{\tau^2}{GE_S} = \frac{\alpha^2}{\alpha_S} \simeq \text{constant} \qquad (4.9)$$

The ratio $\tau^2/E_S G$ was, however, not found to be constant here; there are several possible sources of error to account for this.

On increasing the strain the spacing of dislocations must decrease i.e. the dislocation spacing within the dislocation walls decreases and the cell size itself also decreases, thus the interaction between dislocations increases. This means that α_S in equation 4.6 changes, albeit very slowly, with strain. Thus, the r.h.s. of equation 4.9 is not constant; α may also change if the deformation mechanism alters. Additionally, at high strains (>100%)

the cell structure changes from one containing walls of discrete dislocations to a polygonised structure where the walls are sharp low angle boundaries. Thus, the dislocation density calculated at high strains would have no physical meaning.

Errors also occur in using the hardness in order to derive the flow stress for two reasons. Firstly, Wingrove (1972) has shown that in rolled polycrystalline copper at high strains, >150%, the hardness 'saturates' whilst the true stress continues to increase, see fig. 3.56. Thus, the flow stress is not calculable from the hardness at high strains. This uncertainty would explain the decrease in the value of τ^2/GE_s at a strain of 204% since the hardness would provide an underestimate of the flow stress. Secondly, Thompson and Flewitt (1975) reported that the hardness of rolled polycrystalline niobium is not a unique function of strain but depends on the particular surface of the specimen on which the hardness indentation is made. There are two reasons for this. Firstly, an indentation on a surface normal to the rolling plane is a strain reversal and a Bauschinger effect would be expected. Secondly, the cell dimensions vary with specimen orientation, so that the hardness indenter encounters a different orientation and cell structure in each section. Thus, a single value of the hardness may not be representative of the flow stress in rolled specimens.

Taking into account the above errors, the dislocation density as determined from the hardness and the stored energy show reasonable agreement.

The theoretical work done in applying a stress τ through a strain $d\varepsilon$ is given by

$$W = \int \tau d\varepsilon \qquad (4.10)$$

Now if the stress and strain are assumed to be related as:

$$\tau = C\varepsilon^m \qquad (4.11)$$

where m is a fractional work hardening exponent. Then substituting for τ in equation 4.10 and integrating:-

$$W = \frac{C\varepsilon^{m+1}}{m+1} \qquad (4.12)$$

Now, combining equations 4.7 and 4.11

$$C\varepsilon^m = \alpha G b \rho^{1/2} \qquad (4.13)$$

From, equations 4.5 and 4.6

$$E_s = \alpha_s G b^2 \rho \qquad (4.14)$$

using equation 4.13 to eliminate ρ in equation 4.14

$$E_s = \frac{\alpha_s C^2 \varepsilon^{2m}}{\alpha^2 G} = K\varepsilon^{2m} \qquad (4.15)$$

Thus the ratio of the theoretical work expended during deformation to the energy stored is

$$\frac{W}{E_s} = \frac{C\varepsilon^{m+1}}{K\varepsilon^{2m}}$$

$$= K'\varepsilon^{1-m} \qquad (4.16)$$

For an ideal plastic metal, m=0 i.e. no energy is stored during deformation, so that W/E_s increases linearly with strain. However, all

real metals work harden, so m is greater than zero but less than one. Equation 4.16 predicts that the greater the work hardening exponent, the smaller is the ratio of the expended energy to the stored energy increase. Bever, Holt and Titchner (1973) quote considerable evidence to support the statement that the ratio of the stored to expended energy decreases with increasing strain, as expressed by equation 4.16.

For F.C.C. metals parabolic hardening is often found, i.e. m=1/2, thus from equation 4.15 the stored energy will increase linearly with the strain. This result was found experimentally in the present work.

The graph of stored energy versus strain must deviate from the linear relationships, found here, at low strains in order to accommodate the zero energy requirement at zero strain; the stored energy will be slightly greater than zero due to the 'grown in' forest dislocations, but negligibly so. Although the exact form of the relationship at lower strains is not known, the slope of the graph must increase as zero strain is approached, thus more energy is stored for a given strain increment at lower strains.

The stored energy increase is the difference between the dislocation multiplication and dynamic recovery. At high strains any increase in dislocation density is balanced by dynamic recovery, so that a saturation value of the stored energy occurs. This saturation value will correspond to the 'limiting cell size' discussed in Chapter 3.

Thus, at low strains little dynamic recovery can occur. At medium strains the extent of dynamic recovery increases such that the stored energy increases linearly with strain (this corresponds to parabolic strain hardening). At very high strains dynamic recovery removes any

increase in dislocation density so that a 'saturation' value of the stored energy, and hence dislocation density, is found.

4.5 Summary

A prior internal oxidation treatment has been shown to lower the subsequent recrystallization temperature of deformed copper but not to affect the stored energy. This change in recrystallization kinetics, which was independent of the oxidation temperature, was ascribed to the gettering of residual solute.

The stored energy of copper single crystals has been shown to depend on their orientation. The recrystallization kinetics cannot, however, be predicted from the stored energy values alone.

The above two results demonstrate that the correct control to use for comparisons of recrystallization rate of particle-hardened single crystals produced by internal oxidation with single phase crystals is internally oxidised pure single crystals of the same orientation. Previous research, thus, has not used the correct control for assessing the changeover from acceleration to retardation in particle-hardened single crystals.

The dislocation densities estimated from hardness measurements and stored energy values are found to be in agreement. It has been demonstrated that the linear increase in stored energy with increasing strain that was experimentally found is to be expected for a metal which demonstrates parabolic work hardening.

Fig. 4.1

Typical output from Perkin-Elmer DSC2. Sample is (110)[1$\bar{1}$2] copper crystal, strain=69%, weight=89.88mg. Heating rate is 40 K/min.

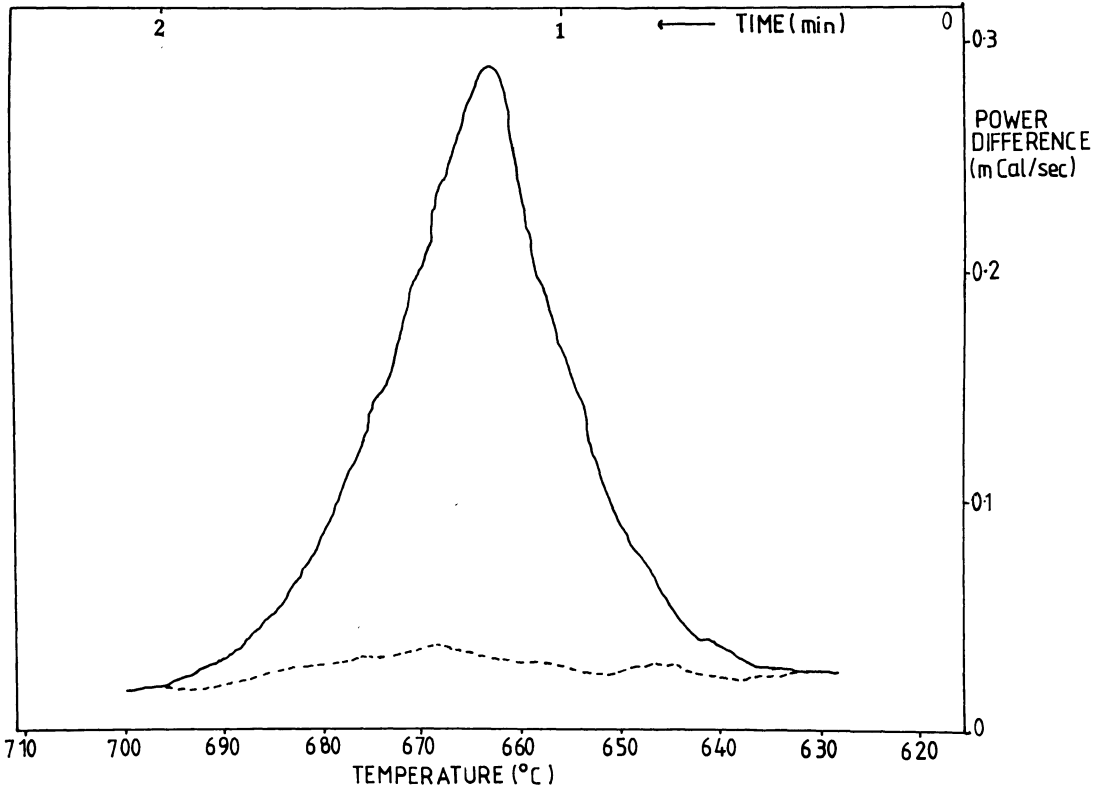
2
1
TIME (min)
0
0·3
POWER
DIFFERENCE
(m Cal/sec)
0·2
0·1
0
710
700
690
680
670
660
650
640
630
620
TEMPERATURE (°C)

Fig. 4.2

Output from Perkin-Elmer DSC2 for Indium reference sample, weight=4·09mg. Heating rate=20 K/min.

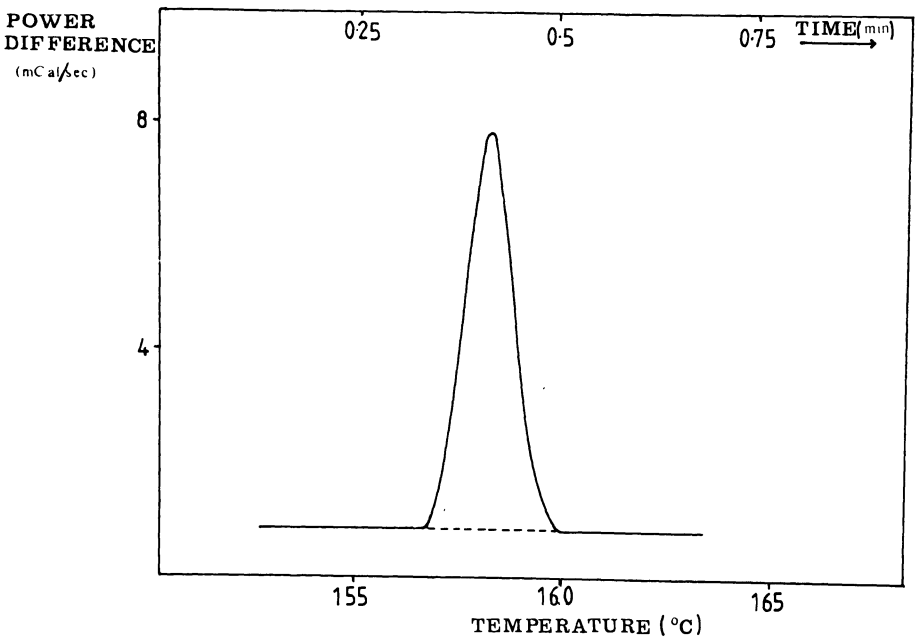
POWER
DIFFERENCE
(mCal/sec)
8
4
0·25
0·5
0·75
TIME(min)
155
160
165
TEMPERATURE (°C)

Fig. 4.3

Schematic diagram of theoretical output of Perkin-Elmer DSC2 for a sharp transition and a rapid heating rate. T denotes the transition temperature. The dotted curve shows the effect of increased sample size.

POWER

DIFFERENCE

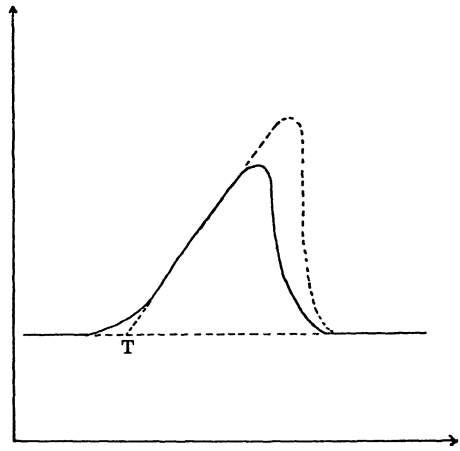

TEMPERATURE

Fig. 4.4

Typical output from Du Pont Thermal Analyser. Sample is alloy L, strain=204%, weight=22.46mg. Heating rate is 20 K/min.

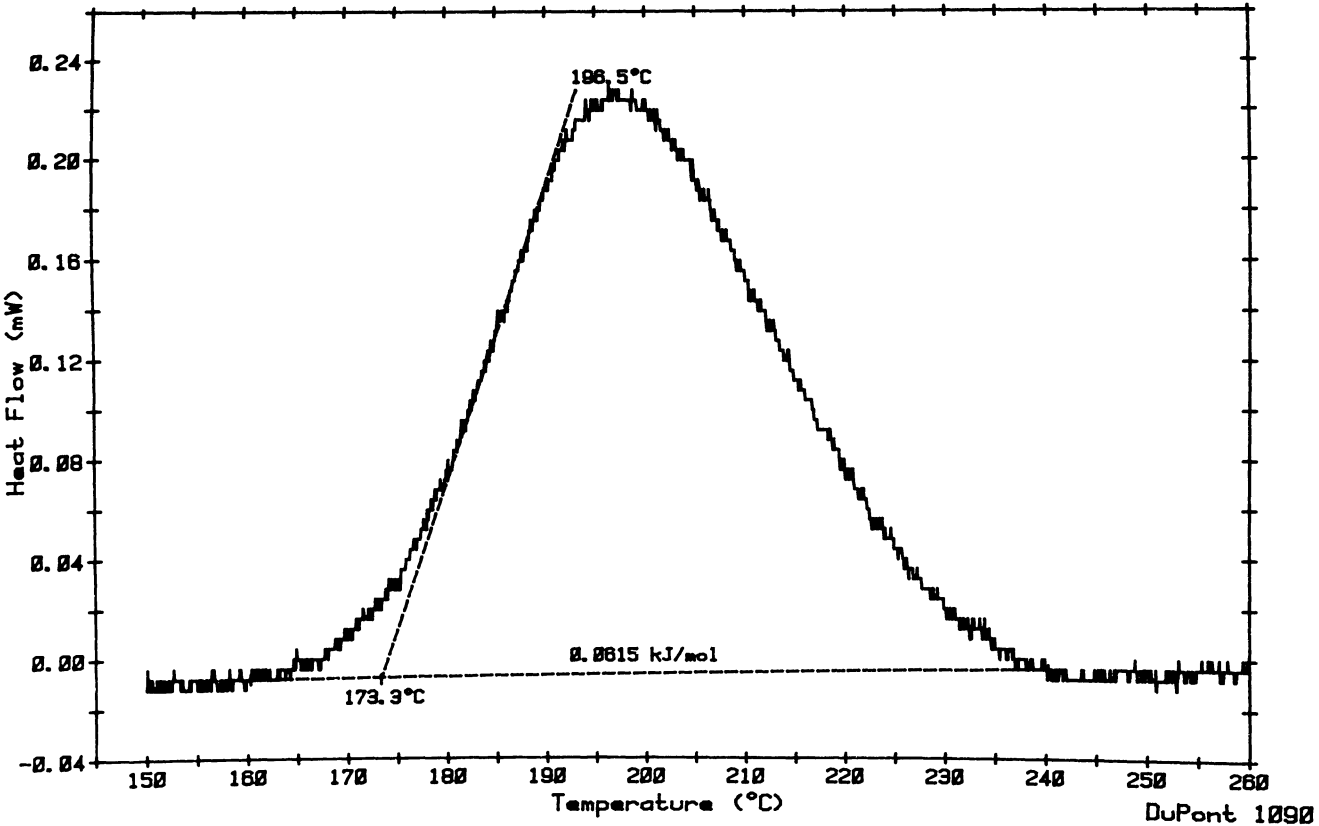
196.5°C
0.0815 kJ/mol
173.3°C
Heat Flow (mW)
0.24
0.20
0.16
0.12
0.08
0.04
0.00
-0.04
150
160
170
180
190
200
210
220
230
240
250
260
Temperature (°C)
DuPont 1090

Fig. 4.5

Isothermal recrystallization kinetics of 50%-rolled (110)[1$\bar{1}$2] single crystals at 350°C.

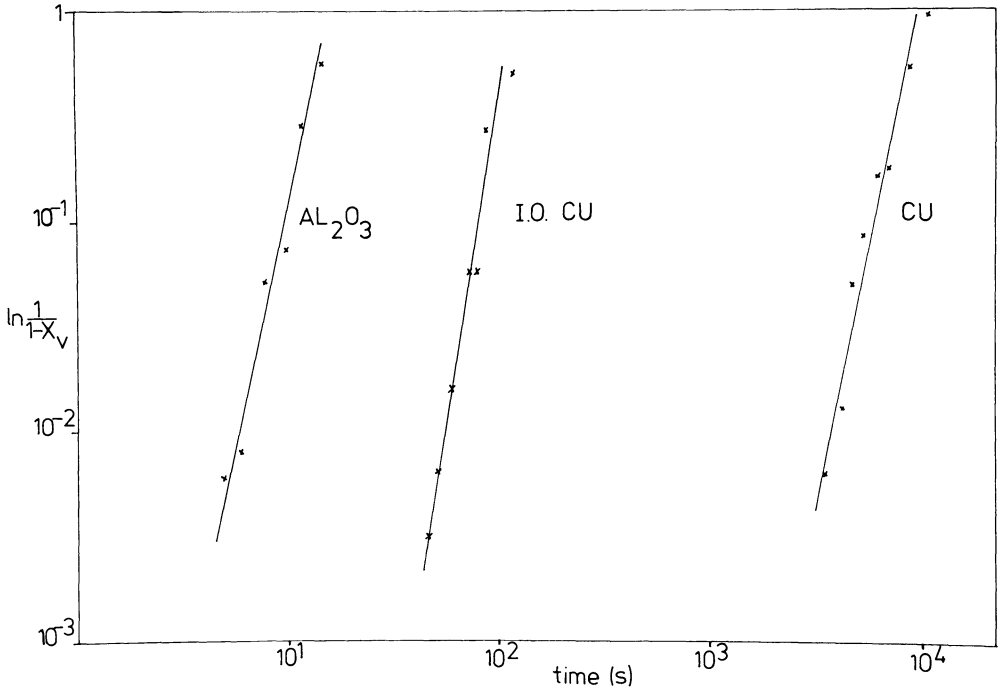
1
10^{-1}
10^{-2}
10^{-3}
$\ln \frac{1}{1-X_v}$
AL_2O_3
I.O. CU
CU
10^1
10^2
10^3
10^4
time (s)

Fig. 4.6

Stored energy and recrystallization temperature of a high purity copper single crystal (initial orientation (112)[$\bar{1}\bar{1}$1]) versus reduction of the thickness. (After Haessner and Hoschek, 1976).

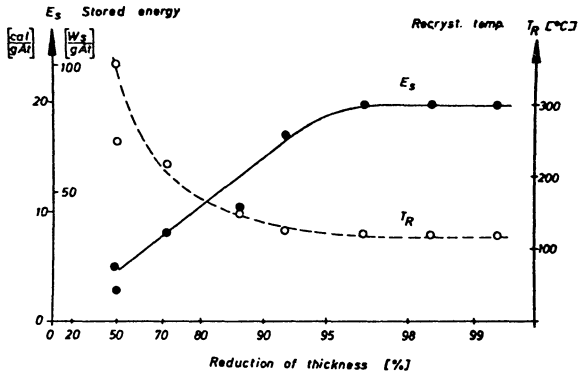
E_s Stored energy
[cal/gAl]
[Ws/gAl]
Recryst. temp. T_R [°C]
100
20
50
10
0
E_s
T_R
300
200
100
0 20 50 70 80 90 95 98 99
Reduction of thickness [%]

Fig. 4.7

Graph of stored energy as a function of strain for (111)[1$\bar{1}$0] single crystals.

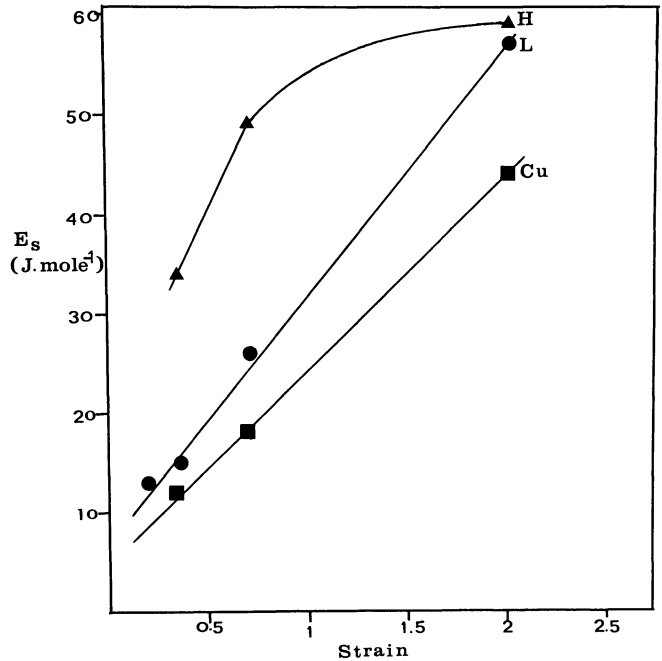
60
50
40
30
20
10
E_s
(J.mole^{-1})
H
L
Cu
0·5
1
1.5
2
2.5
Strain

Chapter 5

Recrystallization Kinetics in Two-Phase Alloys

5.1 Introduction

In this chapter the effect of particles on the stored energy of deformation is outlined and compared with the predicted increase in stored energy from calculations.

The effect of particles on the recrystallization kinetics is considered as a function of strain for two particle distributions. Slip homogenization and particle pinning are both considered as ways of inhibiting nucleation. Nucleation is shown to be associated with inhomogeneities and a model based on pinning by particles is presented in order to explain the effect of changes in interparticle spacing on nucleation at microbands.

5.2 The Change of Stored Energy due to Particles

Little work has been undertaken to measure the stored energies in particle-containing materials. Chin and Grant (1967), using annealing calorimetry, found that two copper-alumina alloys produced by high strain rate extrusion from a powder differed little in stored energy at 111.5J/mole and 108.8J/mole even though the volume fraction of alumina was 0.3 and 1.1 vol. % respectively (sic). They did not, however, measure the stored energy of the comparable single phase metal and concluded that comparison with other workers' data was

impossible since the stored energy appeared to be extremely dependent on the exact deformation conditions.

The addition of particles causes an increase in the stored energy of deformation compared to the single phase material by the production of `geometrically necessary' dislocations which are required to accommodate the particles during the deformation of the matrix. Using equations 4.5 and 4.6 together with the stored energy values one can estimate the total dislocation density in the particle-hardened alloy and the extra dislocation density calculated from the increase in stored energy due to the particles, ΔE. Observations of completely recrystallized specimens sometimes showed that some dislocations were left in tangles around particles, however, the number of these was extremely small compared to the deformed state, fig. 5.21. The results are shown in table 5.1. It is also possible to calculate the theoretical number of `geometrically necessary' dislocations, from equation 1.4, for each alloy; the results are also shown in table 5.1.

Table 5.1

Dislocation densities derived from the stored energy and from eq. (1.4).

True Strain	Dislocation densities $x10^{15} m/m^3$						
	Single Phase	Alloy L			Alloy H		
	from E_s	from E_s	from ΔE_s	from eq. 1.4	from E_s	from ΔE_s	from eq. 1.4
36%	1.12	1.40	0.28	1.17	3.16	2.04	3.52
69%	1.68	2.42	0.74	2.25	4.56	2.88	6.75
204%	4.10	5.31	1.21	6.66	5.50	1.40	19.96

Ashby (1970) has plotted the geometrically necessary dislocation density, ρ^G, as a function of strain for several values of the geometric slip distance, λ^G (=r/f for equiaxed particles), see fig. 5.1.

On the same graph he also plots the experimentally-determined statistically stored dislocation density, ρ^S, for a tensile-deformed copper single crystal: no simple geometric agreement exists to calculate ρ^S since accumulation of statistically stored dislocations is by mutual trapping through chance encounters. Comparing the number of geometrically necessary and statistically stored dislocations he arrived at the following conclusions. At large λ^G (>100 microns) ρ^G will contribute little to the total dislocation density ρ^T (where $\rho^T = \rho^S+\rho^G$). At intermediate λ^G values (~ 20 microns) ρ^G will dominate at low strains but will be swamped by ρ^S at high strains. For small λ^G (< 2 microns) ρ^G will dominate at all strains. He points out that his estimation of ρ^G from equation 1.4 is a lower limit to the increased dislocation density due to particles since the presence of geometrically necessary dislocations will also accelerate the accumulation of statistically stored dislocations.

Comparison of the dislocation densities measured here in the single phase and two-phase materials indicates that the geometrically necessary dislocations are neither swamped by nor dominate the statistically stored dislocation density, even though for λ^G values of 4.8 and 1.6 microns (for alloys L and H) one might expect, from Ashby's data, the geometrically necessary dislocation density to dominate, especially at lower strains. There are two reasons for this difference. Firstly, the statistically stored dislocation density in

the single phase is much higher for a given strain in these rolled single crystals than in the tensile-deformed specimen data used by Ashby since more slip planes operate and so tangles occur more frequently. Secondly, the statistically stored dislocation density data plotted by Ashby was experimentally determined and so includes recovery effects, whilst the geometrically necessary dislocation density plotted does not include these effects, although Ashby suggests these latter dislocations may be more susceptible to recovery. Comparison of the theoretical geometrically necessary dislocation densities with the measured dislocation densities in table 5.1 indicates that recovery does occur and its magnitude increases with dislocation density (and thus both the strain and the volume fraction of particles) e.g. note that the stored energy values of alloy L and H at a strain of 204% are very similar.

A particular crystal orientation appears to have an inherent maximum stored energy (and dislocation density) for a given deformation process, see fig. 4.6. The effect of increasing the number of particles seems to be to reach this maximum at lower strains and its value is raised slightly, since the particles will pin dislocations and thus prevent recovery. The fact that at high strains a small difference in dislocation density still remains is reinforced by the data of Grant (1964) and Haessner et al. (1979). Grant, table 1.1, still found a difference in yield stress at high strains between single-phase and particle-hardened alloys. The stored energy values, reported by Haessner et al. (1979), see table 4.4, showed that the value of the 'saturation' stored energy is raised by the addition of particles.

At medium strains the dislocation densities in the

particle-hardened material show increasing differences from the pure copper (this difference is greater for a larger volume fraction of particles) due to both `extra' geometrically necessary dislocations and also to the inhibition of dynamic recovery by the particles. This resistance to recovery was demonstrated in chapter 3 by the adherence of cell walls to {111} planes in the particle-hardened alloys. However, at high strains, dynamic recovery becomes more important and the properties of single phase and particle-hardened materials converge, although they do not become identical at the observed strains. The results are also shown in table 5.1.

5.3 The Effect of Orientation on the Recrystallization Kinetics

Baker and Martin (1980) and Humphreys and Martin (1966) both demonstrated a changeover from retarded to accelerated recrystallization kinetics as the particle size and spacing was increased. Although they used single crystals, the orientation of the single crystals was not constant. It was noted in section 4.4.2 that single phase crystals of differing orientations recrystallize at differing rates.

This orientation dependence of the recrystallization kinetics will have two effects. Firstly, the comparison of the particle-hardened data of Humphreys and Martin (1966) and Baker and Martin (1980) with a single phase copper crystal is of little value since the recrystallization rates of copper of different orientations vary greatly, see tables 4.5 and 4.7. Secondly, the effect of orientation on particle-containing material may only be of secondary importance, since the present work indicates that for crystals of the

same orientation both acceleration and retardation occur even when compared to internally oxidised copper. However the results tabulated in table 5.2 suggest that an orientation effect exists. From the experimental evidence cited in section 1.5.3, alloy M might be expected to have the lowest recrystallization temperature of the three alloys since it has both a larger particle size and interparticle spacing than alloys L and H. This is not found, although if one considers the reduction in recrystallization temperature compared to the appropriate orientation single phase, then alloy M is seen to have the largest effect.

Table 5.2

Recrystallization Kinetics at 69% Strain

Alloy	Recrystallization temperature (^{o}C)	Temperature of recrystallization below that of single phase. (^{o}C)
L (111)[1$\bar{1}$0]	287	-61
H (111)[1$\bar{1}$0]	278	-70
M (110)[1$\bar{1}$2]	281	-92

The crystal orientation appears therefore to have some effect on the recrystallization kinetics of particle-hardened alloys. Its effect may only be minor so that the recrystallization rates of the particle-hardened crystals reported by Humphreys and Martin (1966) and Baker and Martin (1980) are likely to be only affected a little.

5.4 Recrystallization Kinetics and the Effect of Strain

5.4.1 Copper

At 5% strain pure copper was found only to recover during annealing. At this deformation only dislocation tangles were present in the deformed microstructure, although some large cells were noted after annealing, fig. 5.2. This lack of recrystallization is due to the low driving force. At strains of 11% and above, recrystallization occurred. The recrystallization temperature, see fig. 5.4, and recrystallized grain size, fig. 5.5, were found to decrease as the prior strain was increased. All the above results would be predicted by the laws of Burke and Turnbull (1952) as listed in section 1.3.1.

5.4.2 Copper-alumina

Both copper-alumina alloys demonstrated complete suppression of recrystallization and only recovery occurred at strains up to 11%, even though the dislocation density, and hence driving force for recrystallization, were much greater than in the pure copper at these strains.

At strains above 11% both alloys L and H exhibited recrystallization. The recrystallization temperatures and grain sizes are also shown in figs. 5.4 and 5.5; the two graphs show great similarity.

At 20% strain alloy H showed retarded recrystallization compared to pure copper and a larger recrystallized grain size. All other strains in alloys L and H above 11% demonstrated accelerated

recrystallization kinetics compared to pure copper and a smaller recrystallized grain size. The grain sizes indicate that whilst both the rates of nucleation and growth may be affected by the particles, the nucleation rate is most greatly affected.

Some of the reasons for the above effects will now be discussed.

5.4.3 Inhibition of Recrystallization

Slip Homogenization

At the lowest strains (<11%) annealing of deformed specimens led only to a gradual loss of dislocation density and some formation of dislocation nets, figs. 5.3, 5.6, 5.7 and 5.10. After long anneals at high temperature, some low angle boundaries consisting of dislocation tangles around a local 'excess' of particles was all that remained of the deformed structure, figs. 5.8 and 5.9. This resistance to recrystallization has often been ascribed to slip homogenization i.e. smaller spacing between slip planes but less intense slip on each slip plane, resulting in smaller misorientations across cell walls and thus more difficult formation of a high angle boundary.

The present work, however, whilst finding a smaller cell size in the copper-alumina, found larger misorientations across cell boundaries, see chapter 3. The latter also suggests a larger dislocation density and hence a larger stored energy per unit area of boundary.

The stored energy per unit volume was determined and the cell size was measured, so that one can estimate the stored energy per unit

area of cell boundary from:-

$$\left|\begin{matrix}\text{stored energy/}\\ \text{unit volume}\end{matrix}\right| = \left|\begin{matrix}\text{Stored energy/}\\ \text{unit area of boundary}\end{matrix}\right| \times \left|\begin{matrix}\text{area of boundary/}\\ \text{unit volume}\end{matrix}\right| \quad (5.1)$$

If one considers a cubic cell of size 1, then the volume occupied by a cell is 1^3. The area of boundary surrounding the subgrain is $3l^2$ (since the subgrain has six faces but each face is shared with a neighbouring cell). Hence, the area of cell boundary per unit volume is $3l^2/l^3 = 3/l$. Thus equation 5.1 can be rewritten

$$E_s = E_b \times \frac{3}{l} \quad (5.2)$$

In fact sub-grains were not cubic, so that the cubic root of all the subgrain dimensions must be used for l; note the T.D. cell size was not measured but was assumed to be the same as the RD size, as noted by Hu (1969), and is essentially strain independent. Values of the stored energy per unit area of boundary are shown in table 5.3 at 69% strain.

Table 5.3

Material	Cell size (microns)				E_s	E_b
	RP normal	RDirection	TDirection	mean	$Jmole^{-1}$	Jm^{-2}
Cu	0.39	1.00	1.00	0.73	18	0.62
L	0.23	0.90	0.90	0.57	26	0.70
H	0.24	0.71	0.71	0.50	49	1.15

This calculation assumes that all dislocations are situated in

cell boundaries: thus the actual values of the stored energy per boundary may not be absolutely correct; also there are errors in measuring cell size dimensions. However, the relative values indicate that the stored energy per boundary, and hence dislocation density per boundary, is greater in the particle-containing material, in agreement with the observed boundary misorientations.

Similarly, Dillamore, Smith and Watson (1968) examined different orientations in polycrystalline iron and found that an increased stored energy was associated with a smaller cell size and larger average cell boundary misorientation.

Thus, in the present case at least, slip homogenization plays no part in preventing recrystallization. Indeed, an opposite effect to slip homogenization appears to be present and so recrystallization might be thought to be enhanced by the particles.

Another possible source of inhibition of nucleation is the pinning of sub-boundaries by particles. In order to consider the pinning effect, it is first necessary to assess the driving force at 11% strain.

5.4.4 Driving Force for Recrystallization

The driving force can be estimated from equation 4.9 and from the hardness values as outlined in section 4.4.3. The values of the 'constant' α^2/α_s can be determined from the experimental values of hardness and stored energy at higher strains, see table 5.4.

Table 5.4

Material & Strain	Hardness at $\varepsilon_o=\varepsilon-8\%$ (VPN)	Stored Energy (J/mole)	α^2/α_s $(=\tau^2/E_sG)$	mean α^2/α_s
20% L	85	13	0.95	
36% L	93.5	15	1.00	0.95
69% L	116.5	26	0.89	
36% H	114.5	34	0.66	0.62
69% H	128.5	49	0.58	

At 11% strain, the hardness values for L and H are 59 and 80 VPN which yields stored energies of 6.3 J/mole and 17.7 J/mole.

5.4.5 Pinning of Sub-boundaries

Using a Zener pinning model, where each particle exerts a maximum pinning force of $\pi r\lambda_{s.b}$, Duggan and Hutchinson (1975) assessed the locking of sub-boundaries by particles. For an area, A, (m^2/m^3) of subgrain boundary per unit volume and N_v $(=3f/4\pi r^3)$ particles per unit volume, the number of particles per unit volume on a subgrain boundary is N_v/A or $3f/4\pi r^3A$. Thus, the maximum retarding force on sub-boundaries per unit volume is

$$F_{s.b}^{max} = \frac{3f\lambda_{s.b}}{4r^2A} \qquad (5.3)$$

where A is given by 3/1. This assumes all particles lie on the sub-boundary, which is not found, however the majority are associated

with the boundary. The cell sizes in the Rolling direction and Transverse direction are those in table 5.3. Taking the rolling plane normal cell size for alloys L and H as 0.71 microns and 0.60 microns gives A as 3.6×10^6 micron^{-1} and 4.5×10^6 micron^{-1} respectively.

Assuming a value for $\lambda_{s.b}$ of 0.15Jm^{-2} gives the maximum pinning force on a sub-boundary as 3.38×10^5 Jm^{-3} and 6.77×10^5 Jm^{-3} or 2.4 Jmole^{-1} and 4.8 Jmole^{-1} for alloys L and H respectively.

Comparison of the calculated driving forces and pinning forces indicate that the sub-boundaries should not be pinned by particles. Subgrain growth was investigated extensively in alloy H at 20% strain where retarded recrystallization was exhibited. The stored energy of alloy H at this strain is about 32Jmole^{-1} (calculated from a hardness value of 107VPN) which is much larger than the Zener pinning force calculated earlier. However, experimentally, no subgrain growth was found even at long annealing times; although the overall dislocation density decreased markedly and cell boundaries became much sharper, figs. 5.12-5.16. Smith and Dillamore (1970) noted that recovery of the cell structure in deformed iron occurs in two stages. First a sharpening of cell walls and also a decrease in dislocations in the cell interiors. Only after these changes had occurred extensively did any subgrain growth occur. Similar investigations in accelerated alloys showed no evidence of subgrain growth and no loss of dislocations prior to the passage of the recrystallization front, fig. 5.11. These observations are in agreement with Baker and Martin (1980) where retarded alloys showed a hardness drop prior to and during recrystallization in the deformed matrix whilst accelerated alloys experienced no change in hardness. Bailey (1963) similarly noted little change in the deformed microstructure of pure copper prior to

recrystallization.

Two points emerge from the above results.

i)No subgrain growth occurs even though pinning calculations based on a simple Zener model suggest that it should. Hazzledine, Hirsch and Louat (1980) have recalculated Zener pinning using a more complex model and found that the Zener pinning expression gives values that are approximately correct. However, Jones and Hansen (1980) point out that the Zener pinning of boundaries may not be the only effect of the particles. Experimentally they found that subgrains stopped growing at 1 micron whereas a Zener pinning calculation suggested a limiting cell size would be reached at 7 microns. They suggest that particles may also inhibit individual dislocation movement in the sub-boundaries and prevent processes such as subgrain coalescence. Jones and Hansen (1980) have published micrographs which illustrate this point.

ii)Since no subgrain growth occurs, recrystallization nuclei cannot originate from the homogeneous cell structure.

5.4.6 Nucleation of Recrystallization

Although specimens of both alloys at all strains were examined for nuclei in the electron microscope, these examinations were unsuccessful at all but the highest strains. At strains up to 69% recrystallized grains could be found but these were always large. The chances of finding a small successful nucleus are low since, for alloy L, even at 69% strain only one successful nucleation event occurs in approximately $10^{-2}mm^3$ of specimen. When examining a good thin foil one views only about $10^{-4}mm^3$ of specimen in which many 'potential'

nucleation sites are present.

Many fairly small grains could be produced in specimens deformed to 204% strain after short anneals, fig. 5.17. However, as thin foils could only be produced from the rolling plane at these strains, no information about the nucleation site for these grains could be determined.

Since nucleation of recrystallization did not occur in the homogeneous structure as outlined in section 5.4.5 by implication nucleation must occur at deformational inhomogeneities. That these inhomogeneities are of greater importance than the driving (or pinning) forces is illustrated in fig. 5.18 where alloy L can be seen to recrystallize faster than the single phase copper at a given driving force even though particle pinning also occurs.

Now microbands increase in frequency and decrease in size as the strain is increased. This results in some microband clustering at higher strains. In a pure material, the increased frequency of microbands means that more potential nucleation sites are present. The smaller size of the microbands also results in a higher local strain energy density and so a greater local driving force for recrystallization.

Nucleation would also be more favoured at microband clusters since here boundaries will be able to establish a high angle interface after only a small amount of migration.

The results of these effects is more rapid nucleation at more nucleation sites as the strain increases. This is seen as a lowering of recrystallization temperature and a smaller recrystallized grain size at higher strains. Nucleation at inhomogeneities is thus consistent with the experimental observations.

For a two-phase alloy, it is difficult to assess quantitatively the driving forces and pinning forces involved at microbands. The average stored energy per unit volume is not the local driving force for recrystallization at microbands. There is a strain energy concentration at these regions and the local driving force will be greater.

Similarly it is difficult to assess the pinning force at microbands. The cell walls in the homogeneous cell structure are associated with the particles since the walls form from the tangles surrounding particles. However, it is not known whether microband walls are associated with particles, whether they avoid particles or whether they simply occur randomly.

The various recrystallization kinetics can, however, be explained here qualitatively in terms of microbands.

When particles are added the average stored energy will be increased and presumably the local strain energy density at microbands will be higher than in the microbands of the single phase material. Particle pinning of microbands will also occur. Three situations can be envisaged.

i) At low strains microbands are wide e.g. the microband at 11% strain in alloy L in fig. 3.30 is 0.34 microns wide. The microbands (and the homogeneous cells) are wider than the interparticle spacing in alloy L where Δ_2 is 0.22 microns. This situation is illustrated in fig. 5.19a. Thus all dislocation walls will contain particles and experience a retarding force preventing migration of cell boundaries and a retardation of dislocation rearrangement within the boundary. Thus, recrystallization will be completely suppressed since no high

angle boundaries can form. This was found in alloys L and H at low strains, <11%.

ii) At higher strains, the situation will be similar to that shown in fig.5.19b. Now the microband width is much smaller than the interparticle spacing e.g. in alloy M microbands are as small as 0.03 microns and cluster together whereas the interparticle spacing Δ_2=0.24 microns, see fig. 3.54.

The smaller width of microbands means that many sections of boundary are particle-free. The smaller width also results in a high local strain energy density so that boundary migration will thus have a large driving force. A large misorientation may be acquired by the migrating boundary before a particle is encountered. The average driving force for recrystallization at a given strain in two-phase alloys will be larger than the single phase, as will the local driving force, not only because of the larger dislocation density but also because of the more frequent microbands which may form clusters. Nucleation of recrystallization will then be accelerated compared to the single phase material. This acceleration occurred in all alloys as the strain was increased.

iii) An intermediate situation between i) and ii) may occur. The microband width will be smaller than in i) so that some microband walls will be particle-free. However, after a small amount of migration of a particle-free boundary, a particle will be encountered and this will exert a dragging force on the interface. However, compared to i) the local strain energy density will be larger and the migration of the boundary will allow some increase in misorientation of the interface. In this

case the interface will continue to migrate, due to the larger driving force than in i), but it will also experience particle pinning which slows the formation of the nucleus. Thus nucleation will occur but this may be retarded compared to the single phase material (due to the particle pinning effects).

Retarded recrystallization was found in alloy H (at 20% strain) but not in alloy L between the change from inhibition to acceleration of recrystallization. This is because alloy H had a smaller interparticle spacing, $\Delta_2 = 0.14$ microns, than alloy L, $\Delta_2 = 0.22$ microns, so that this third process could occur.

One can consider this model at a given strain and hence a given microband width and frequency for a variety of interparticle spacings. At small interparticle spacings relative to the microband width total suppression of recrystallization would be expected, situation i) above. At slightly larger interparticle spacings, a balance of the driving force and the retarding force due to the particles leads to nucleation of recrystallization but this will be retarded compared to the single phase material, situation iii) above. At interparticle spacings which are large compared to the microband width, little particle pinning would occur but an enhanced driving force due to the particles will lead to accelerated recrystallization, situation ii) above.

Thus, the retarding effect of particles on microbands can be used to explain the recrystallization kinetics both as a function of strain and of interparticle spacing.

5.5 Growth

As noted earlier, no change was observed in the deformed matrix during recrystallization in alloys exhibiting accelerated recrystallization kinetics. Thus one would expect the migration of the recrystallizing interface to be more rapid in two-phase alloys if the extra driving force, ΔE, due to the particles, was greater than the Zener pinning drag on the migrating interface i.e.

$$\Delta E > \frac{3f\gamma}{2r} \qquad (5.4)$$

Assuming a value for γ of $0.5 Jm^{-2}$ the r.h.s of equation 5.4 is 3.3 and 1.1 $Jmole^{-1}$ for alloys H and L respectively.

These are much smaller than the increases in driving force, ΔE, found. It is also possible that growth was still accelerated in alloy H at 20% strain when retarded nucleation was exhibited since ΔE initially was at least $15 Jmole^{-1}$. After annealing, the dislocation density fell but is unlikely to have fallen to less than $3.3 Jmole^{-1}$. The very large grain size found at this strain in alloy H indicated that nucleation was much more retarded than subsequent grain growth.

During growth, annealing twins were a frequent occurrence, fig. 5.21. They were often found on the edge of a recrystallizing interface, fig. 5.20. Their importance has been proposed as being that the formation of a twin leads to a lower interfacial energy and a more mobile interface so that the migrating interface can proceed more rapidly, Burke and Turnbull (1952).

5.6 Summary

Addition of a dispersed phase to copper single crystals has been found to cause an increase in stored energy and the increase is greater for a larger volume fraction of particles. This increase in stored energy over the single phase increases with strain. The calculated geometrically necessary dislocation densities (from the stored energies) are less than those predicted by Ashby (1970). The geometrically necessary dislocation density is of a similar order to the statistically stored dislocation density at the strains observed. The effect of particles on the stored energy is essentially that the 'limiting' stored energy is reached at lower strains; the value of this limiting stored energy may also be raised by the prevention of recovery by the particles.

Some evidence was found that the effect of orientation on recrystallization kinetics is not completely masked by the addition of a second-phase.

Calculations suggested that the number of dislocations per unit area of dislocation wall was greater in the particle-containing alloys than in the single phase and that this number increased with the volume fraction of particles. This is consistent with the larger misorientations found across cell boundaries in two-phase alloys compared to the single phase material. Thus slip homogenization is not found (rather the reverse) and cannot be invoked to explain suppression or retardation of recrystallization in particle containing materials.

Comparison of pinning forces on sub-boundaries based on a Zener model with the driving force for recrystallization suggests that

subgrain growth should occur. However, experimentally no such subgrain growth was found, suggesting, in agreement with other workers, that Zener pinning alone does not wholly account for the pinning effects of particles.

This lack of subgrain growth also excluded the homogeneous cell structure as the source of the nuclei for recrystallization.

Alloy H showed a change from complete suppression to retardation to acceleration of recrystallization as the strain was increased whilst alloy L showed only a change from retarded to accelerated recrystallization compared to the single phase. To account for these effects a model based on nucleation at microbands is proposed. The properties of microbands as a function of increasing strain, of decreasing in width and increasing in frequency is used to explain the above recrystallization kinetics by comparing the microband width to the interparticle spacing (and hence the pinning forces) and the increased driving forces due to the addition of the particles. This model can also be used to explain the recrystallization kinetics of alloys with different interparticle spacings at a given strain.

Calculations show that the rate of growth of recrystallization nuclei is greater than in the single phase in alloys exhibiting accelerated recrystallization. In retarded alloys, accelerated growth compared to the single phase may also occur.

Fig. 5.1

Graph of the statistically stored (shaded band) and geometrically-necessary dislocation density, plotted against strain. (After Ashby, 1970).

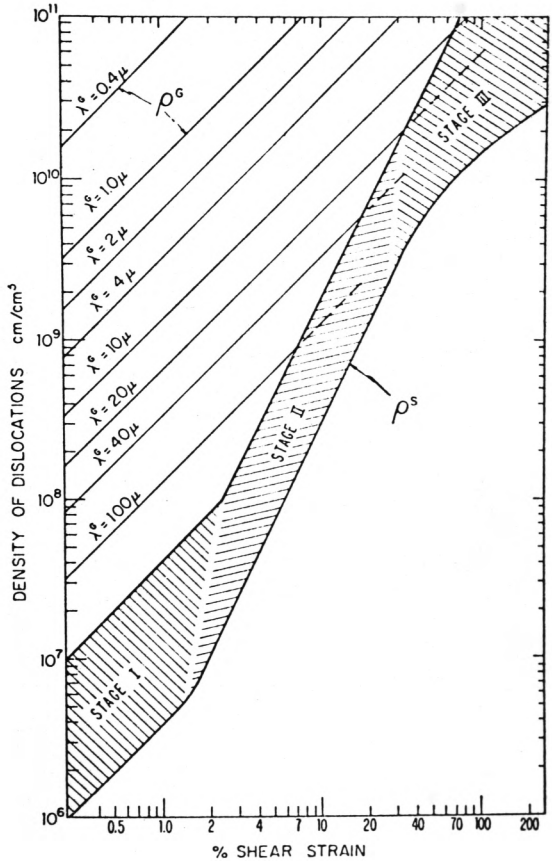
10^{11}
10^{10}
10^{9}
10^{8}
10^{7}
10^{6}
DENSITY OF DISLOCATIONS cm/cm³
λ^e=0.4μ
λ^e=1.0μ
λ^e=2μ
λ^e=4μ
λ^e=10μ
λ^e=20μ
λ^e=40μ
λ^e=100μ
ρ^G
ρ^S
STAGE I
STAGE II
STAGE III
0.5
1.0
2
4
7
10
20
40
70
100
200
% SHEAR STRAIN

Fig. 5.2

Cells in pure copper, strained 5% and annealed for 1 hour at 600°C.

Fig. 5.3

Cells in alloy L, strained 11% and annealed for 1 hour at 600°C.

{111}trace
{111}trace
g[200]
1μ

g[111]
0·5μ

Fig. 5.6

Alloy L, strained 5% and annealed for 1 hour at 550°C showing some dislocation networks at 'a'.

Fig. 5.7

Alloy H, strained 11% and annealed for 1 hour at 700°C showing the reduction in dislocation density.

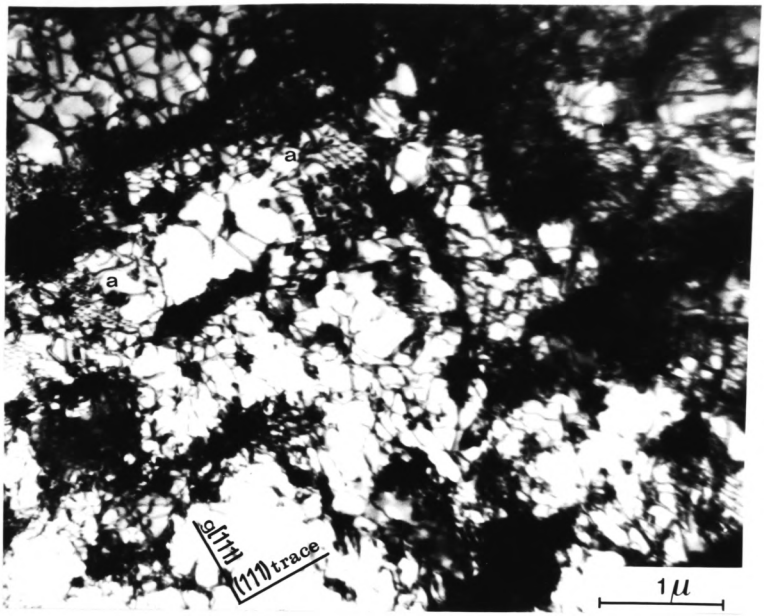
a
a
g[111]
(111) trace
1μ

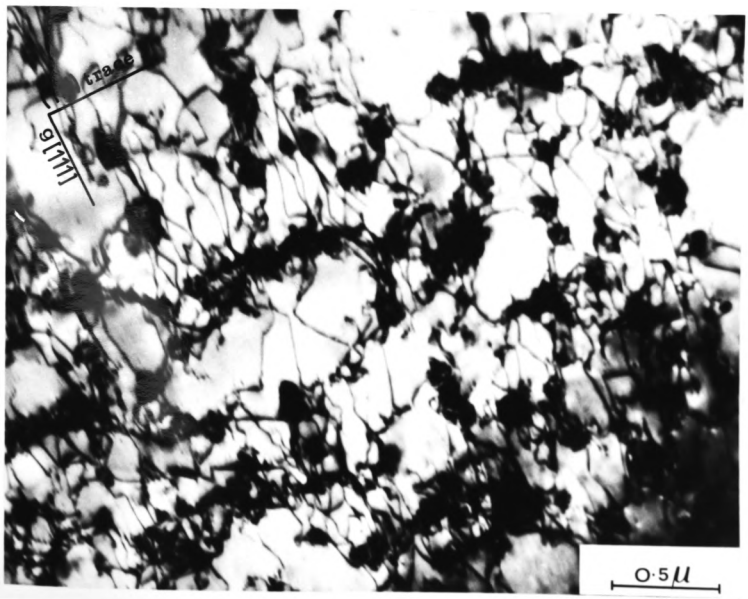
trace
g[111]
0·5μ

Fig. 5.8

Alloy H, strained 5% annealed 12 hours at 750°C showing dislocation boundary.

Fig. 5.9

Alloy H, strained 5% annealed 18 hours at 700°C showing dislocation boundary (misorientation across boundary is only $\sim 0.5^{\circ}$).

{111} trace
g[111]
0·5μ

g[111]
0·25μ

Fig. 5.10

Alloy H, 11% strain, annealed for 1 hour at 600°C.

Fig. 5.11

Alloy L, 20% strain, annealed for 135 sec. at 382°C, when recrystallization has started.

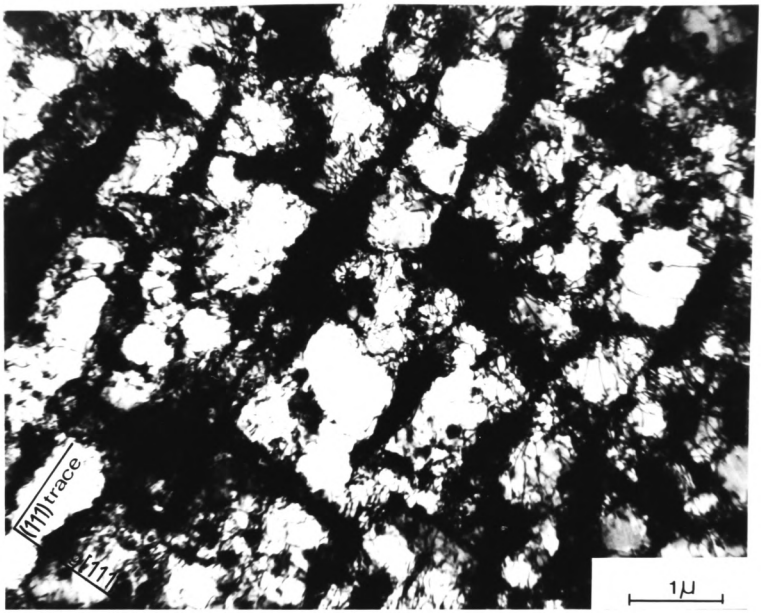
{111} trace
1μ

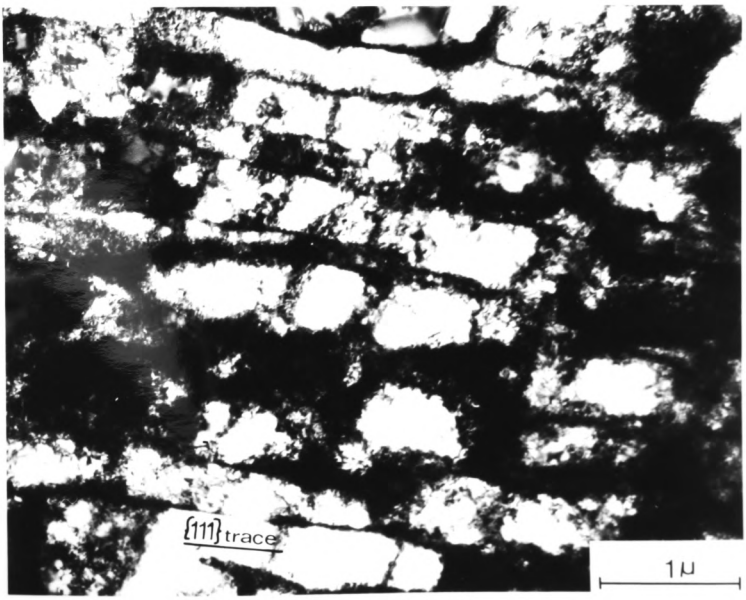
{111} trace
1μ

Fig. 5.12

Alloy H, 20% strain, annealed for 1 hour at 550°C. Little change from the as-deformed state.

Fig. 5.13

Alloy H, 20% strain, annealed for 16 hours at 550°C. Showing recrystallization front.

(111) traces
1μ

g [111]
(111) trace
(111) trace
g [111]
1μ

Fig. 5.14

Alloy H, strained 20% and annealed for 16 hours at 550°C. Specimen shows a loss in dislocation density and sharper cell walls compared to the deformed state.

Fig. 5.15

As above.

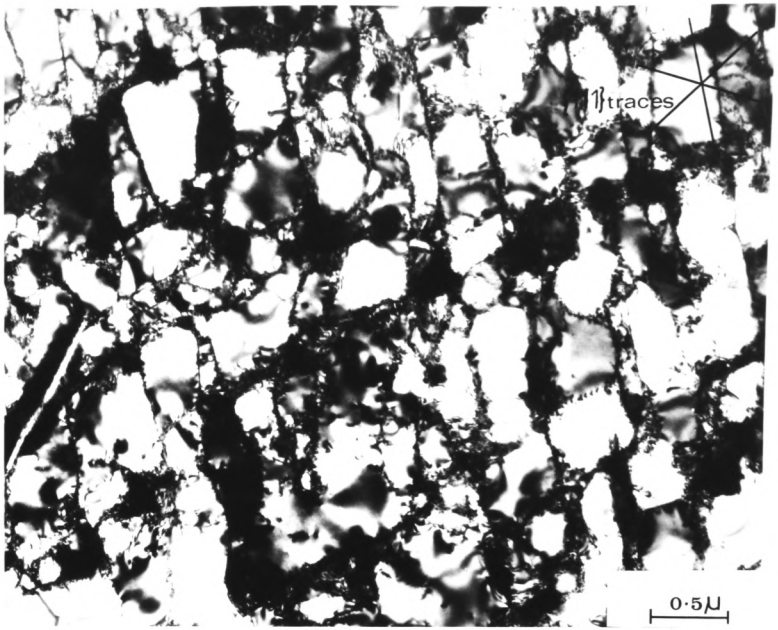
{111} traces
0·5μ

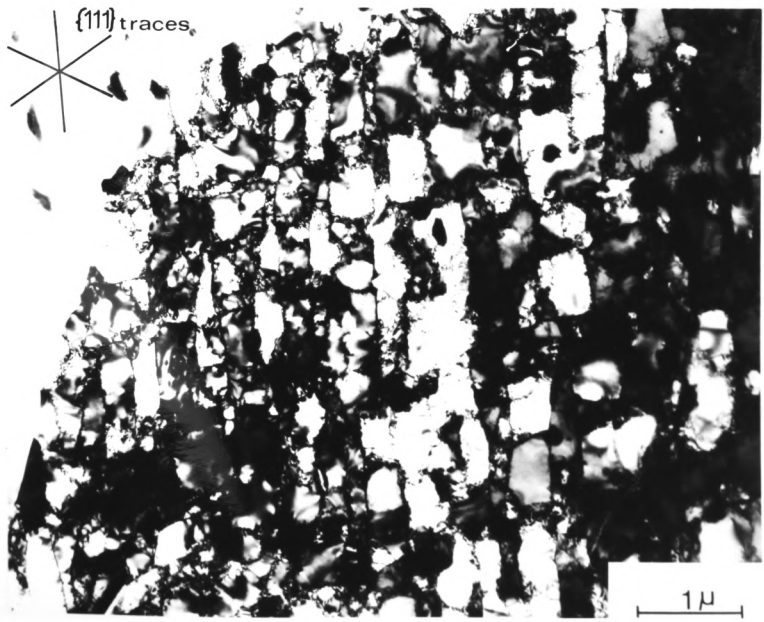
{111} traces
1μ

Fig. 5.16

Alloy H, strained 20% and annealed for 16 hours at 550°C. Shows a dislocation network at 'a'.

Fig. 5.17

Alloy M, 204% strain. Grain found after an in-situ anneal in the HVEM.

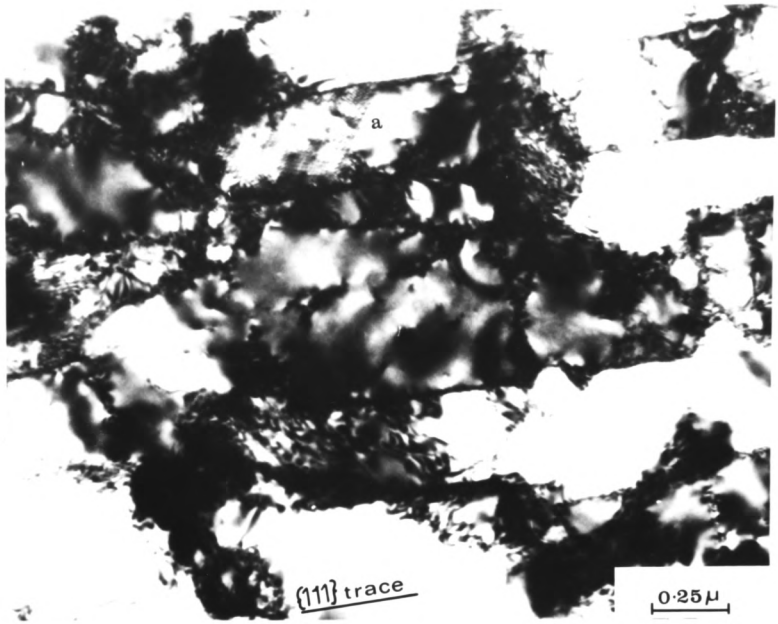
a
(111) trace
0·25μ

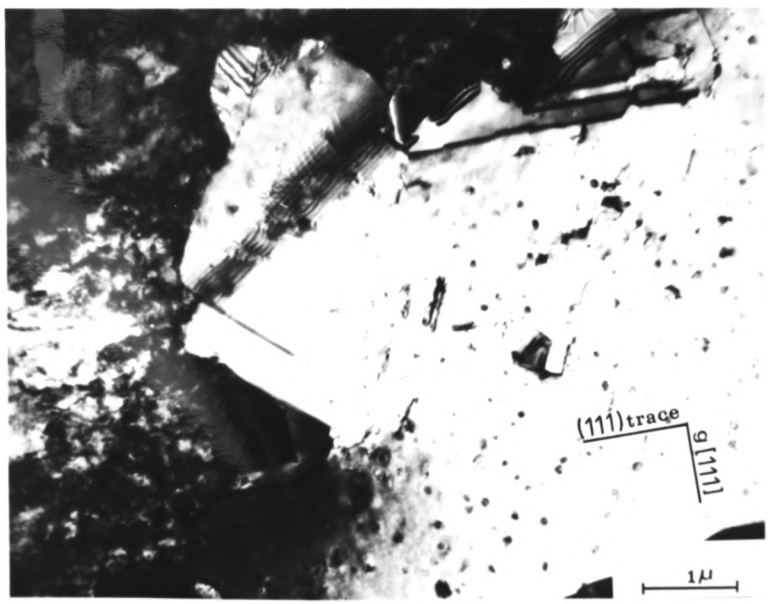
(111) trace
g [111]
1μ

Fig. 5.18

Graph of stored energy against recrystallization temperature for (111)[1$\bar{1}$0] single crystals.

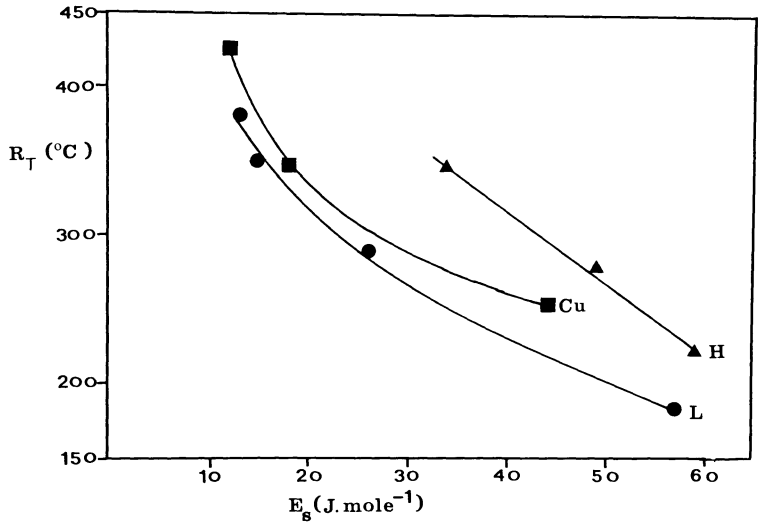
450
400
300
200
150
R_T (°C)
10
20
30
40
50
60
E_s (J.mole^{-1})
Cu
H
L

Fig. 5.19

Schematic diagram of microband structure.

a) at low strain

b) at higher strain.

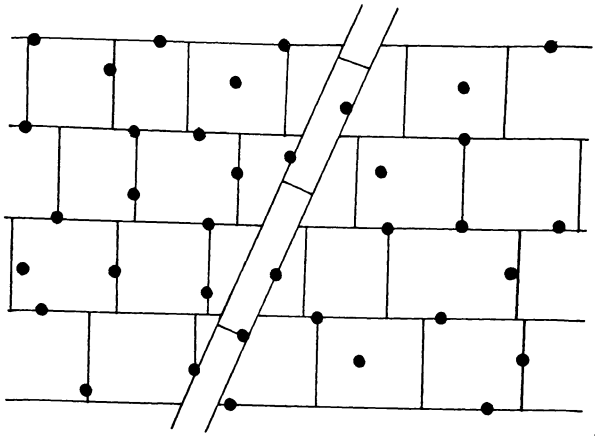

RD

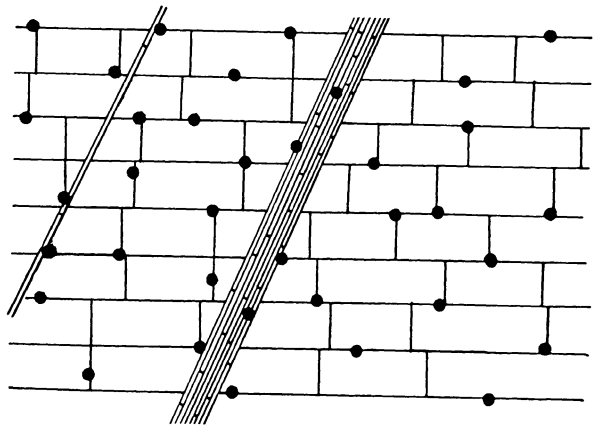

Fig. 5.20

Alloy L, strained 69% and annealed for 12sec. at 350°C. Shows twin (T) formed on the edge of a recrystallized grain (R) growing into the deformed matrix (U).

Fig. 5.21

Alloy L, strained 69% and annealed for 12sec. at 350°C. Shows some dislocations left around particles after the recrystallization front has passed.

U
T
R
{111} trace
{111} trace
0·1 μ

g [020]
(111) trace
1 μ

Fig. 5.22

Alloy M, strained 69% and annealed for 5sec. at 350°C. Shows particle retardation on a migrating boundary.

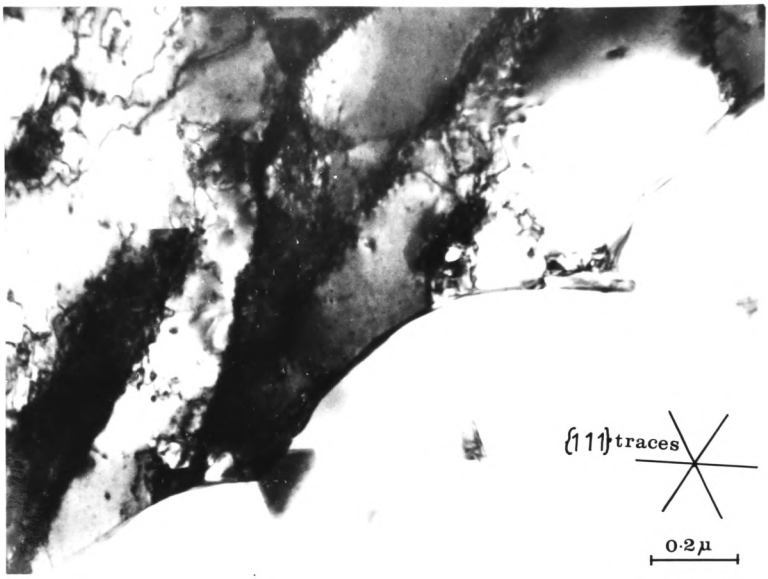
{111} traces
0·2μ

Conclusions

1) Cells form at lower strains in copper-alumina single crystals than in pure copper, the cells are also smaller. This effect is attributed to the 'extra' geometrically necessary dislocations which occur around particles and from which the cells form. Thus a larger number of particles was found to lead to a smaller initial cell size.

2) The cell size and width of the cell size distribution are found to decrease with increasing strain; they are always smaller at a given strain in the particle-containing alloys due to the presence of geometrically necessary dislocations. The cell size, l, and hardness, σ_H, were found to obey the relation $\sigma_H \propto l^{-1}$. Initially the rate of cell size decrease was faster than the geometric deformation rate but the rate of decrease slowed at higher strains. This can be explained in terms of a balance between dislocation multiplication, which leads to cell wall creation at low strains, and dynamic recovery which leads to cell wall annihilation at higher strains.

3) In the copper-alumina crystals, cells are aligned along {111} planes, this was ascribed to particles preventing relaxation of the dislocation structure. At 69% strain, a banded structure with sharp walls forms by recovery from the cells which occur at lower strains. This structure shows less alignment with {111} planes. The structure is similar to that found in copper at high strains and suggests that in copper the banded structure also forms from the cell structure.

4) Microbands were found to occur at all strains along {111} planes. They decreased in width and increased in frequency as the strain increased. The latter property led to transition bands and microband clusters at high strains. The microband density was found to be higher in the particle-containing material, this was attributed to the greater difficulty in accommodating the strain in the particle-hardened matrix.

5) Misorientations, as indicated from spot splitting in diffraction patterns and contrast differences between cells, are larger in the particle-containing material. Direct measurements using focused probe microdiffraction found misorientations of $3\text{-}4^{o}$ in an alumina-containing crystal at 69% strain, this was larger than the misorientations across ordinary cells $0.3<\theta<0.8^{o}$ or microbands ($\sim 2^{o}$) in copper at this strain.

   Calculations of the number of dislocations per sub-boundary, from the measured cell size and stored energy, indicates that there are more dislocations in a boundary in the particle-containing alloys. Thus, although smaller cells are found in the particle-containing alloys, slip homogenization (in which less slip occurs on each slip plane) is not found.

6) An internal oxidation treatment of pure copper is found to have no detectable effect on the dislocation structure or the energy stored after deformation. However, the recrystallization temperature is lowered with respect to pure copper; this effect was ascribed to the gettering of residual solute.

7) (111)[1$\bar{1}$0] copper single crystals were found to recrystallize more rapidly on annealing, after rolling to 69% strain, than (110)[1$\bar{1}$2] crystals, even though the latter had a higher stored

energy. The recrystallization kinetics cannot, however, be predicted from the stored energy alone, they also depend on the microstructural inhomogeneities present which can act as nucleation sites.

8) When dislocation densities in deformed copper are calculated from either the stored energy or the hardness change, they are found to be in reasonable agreement.

9) A linear increase of the stored energy of deformation with strain is found: this was shown to be compatible with a metal that shows parabolic work hardening characteristics.

10) Addition of particles to copper single crystals was found to increase the stored energy of deformation. This increase was greater at higher strains.

11) The geometrically necessary dislocation densities calculated from the measured stored energies are less than those predicted by Ashby (1970). This deviation increases with strain i.e. as dynamic recovery becomes more important.

12) Comparison of the retarding force due to Zener pinning of sub-boundaries by particles with the measured driving force for recrystallization suggests that sub-grain growth should occur. Experimentally no such subgrain growth was found, although some dislocation loss and sharpening of cell boundaries occurred, suggesting that Zener pinning does not wholly account for the pinning effect of particles on boundaries.

13) Copper-alumina alloys were found to show complicated recrystallization kinetics as a function of strain. As the strain was increased, one alloy (H) demonstrated a change from complete suppression, to retardation, to acceleration of recrystallization

compared to the internally-oxidised single phase material. An alloy containing fewer particles (L) was found only to show a change from suppression to acceleration of recrystallization as the strain was increased. Grain size measurements indicated that nucleation of recrystallization was affected more than the subsequent growth by the addition of particles. Thus, since nuclei did not form from subgrains, see 12) above, a model of nucleation based on the properties of microbands was used to explain the recrystallization kinetics.

14) Calculations showed that grain growth was likely to be accelerated in alloys which demonstrated accelerated recrystallization kinetics.

Suggestions for Further Work

1) Acceleration of recrystallization by particles too small to produce Particle Stimulated Nucleation has so far only been observed in internally oxidised copper alloys. Further investigation is required to see whether this effect can occur in other systems; careful control of the matrix solute content would be required.

2) Internally oxidised specimens have the limitation that only thin specimens can be produced, thus the degree of deformation is limited. This limitation means that the recrystallization nucleation frequency is low. Thus the likelihood of observing small nuclei in pre-annealed specimens is low and in-situ annealing in an electron microscope is difficult. The nucleation of recrystallization is most easily observed at high strains, thus another system, say Aluminium-Silicon, in which small particles can be produced and high deformations acheived could be used for in-situ microscopy to observe the effect of particles on nucleation.

3) The recrystallization data available could be made more comprehensive by measurements of the recrystallization kinetics as a function of strain for dispersions containing different particle sizes and spacings.

4) The nature of microbands and the reasons for their occurrence need to be more fully investigated both in single-phase and two-phase materials.

References

Abrahamson, E.P. (1962) Trans. A.I.M.E. 224 727.

Ahlborn, H. and Sauer, D. (1968) Z. Metal. 59 658.

Allain, J, Naudon, A. and Caisso, J. (1979) Acta Met. 27 545.

Anderson, W.A. and Mehl, R.F. (1945) Trans. A.I.M.E. 161 140.

Ashby, M.F. (1966) Phil. Mag. 14 1157.

Ashby, M.F. (1970) Phil. Mag. 21 399.

Ashby, M.F. and Ebeling, R. (1966) Trans. A.I.M.E. 236 1396.

Aust, K.T. and Rutter, J.W. (1959) Trans. A.I.M.E. 215 119.

Aust, K.T. and Rutter, J.W. (1960) Trans. A.I.M.E. 218 682.

Avrami, M. (1939) J. Chem. Phys. 7 1103.

Avrami, M. (1940) J. Chem. Phys. 8 212.

Avrami, M. (1941) J. Chem. Phys. 9 177.

Bahk, S. and Ashby M.F. (1975) Scripta Met. 9 129.

Bailey, J.E. (1963) Phil. Mag. 8 233.

Bailey, J.E. and Hirsch, P.B. (1960) Phil. Mag. 5 485.

Bailey, J.E. and Hirsch, P.B. (1962) Proc. Roy. Soc. 267A 11.

Baker, I. (1979) Part II Thesis.

Baker, I. and Martin, J.W. (1980) J. Mat. Sci. 15 1533.

Bainbridge, D.W., Li, C.H. and Edwards, E.H. (1954) Acta Met. 2 322.

Beck, P.A. (1954) Adv. Phys. 3 245.

Beck, P.A., Ricketts, B.G. and Kelly, A. (1959) Trans. A.I.M.E. 215 949.

Beck, P.A. and Sperry, P.R. (1950) J. Appl. Phys. 21 150.

Bellier, S.P. and Doherty, R.D. (1977) Acta Met. 25 521.

Bever, M.B., Holt, D.L. and Titchner, A.L. (1973) Prog. Mat. Sci. 17.

Blade, J.C., Clare, J.W.H. and Lamb, H.J. (1959) J. Inst. Met. 88 365.

Bollman, W. (1959) J. Inst. Met. 87 439.

Bonisonni, G. and Pagnelli, M. (1965) ALUMINO 34 287.

Brimhall, J.L. and Huggins, R.A. (1966) Trans. A.I.M.E. 233 1077.

Brown, K. and Hatherly, M. (1970a) J. Inst. Met. 98 317.

Brown, K. and Hatherly, M. (1970b) J. Inst. Met. 98 310.

Burgers, W.G. and Verbraak, C.A. (1957) Acta Met. 5 765.

Burke, J.E. and Turnbull, D. (1952) Prog. Met. Phys. 3 220.

Cahn, J.W. (1962) Acta Met. 10 789.

Cahn, R.W. (1949) J. Inst. Met. 76 121.

Cahn, R.W. (1950) Proc. Roy. Soc. A63 323.

Cahn, R.W. (1956) Acta Met. 4 449.

Cahn, R.W. (1964) Deformation Twinning, Gordon & Breach, New York.

Cahn, R.W. (1965) Ed. Physical Metallurgy, North Holland, Amsterdam.

Cahn, R.W. (1966) Recrystallization, grain growth and textures, ASM, Metals Park, Ohio, p99.

Cahn, R.W. (1971) Recrystallization of metallic materials, (Ed. Haessner), Reiderer, Stuttgart, p43.

Cairns, J.H., Clough, J., Dewey, M.A.P. and Nutting, J. (1971) J. Inst. Metals 99 93.

Chin, L.L.J. and Grant, N.J. (1967) Powder Met. 10 344.

Chopra, O.K. and Neissen, P. (1974) J. Mat. Sci. 9 279.

Clarebrough, L.M. (1950) Austr. J. Sci. Res. A3 72.

Comte, P.-A. and Form, W. (1976) Z. Met. 67 158.

Corti, C.W., Cotterill, P. and Fitzpatrick, G.A. (1974) Int. Met. Rev. 19 77.

Cotterill, P. and Mould, P.R. (1976) Recrystallization and grain growth in metals, Surrey University Press.

Cottrell, A.H. (1953) Prog. Met. Phys. 4 255.

Craig, J.V. and Stock, A.C. (1970) J. Aust. Inst. Met. 15 1.

Dillamore, I.L., Morris, P.L., Smith, C.J.E. and Hutchinson, W.B. (1972) Proc. Roy. Soc. A329 405.

Dillamore, I.L., Roberts, J.G. and Bush, A.C. (1979) Met. Sci. 13 73.

Dillamore, I.L., Smith, C.J.E. and Watson, T.W. (1968) Met. Sci. 1 49.

Dimitrov, O. (1965) Mem. Rev. Sci. Met. 62 59.

Doherty, R.D. (1978) Recrystallization of metallic materials, 2nd Ed., (Ed. Haessner), Reiderer-Verlag, Stuttgart, p23-62.

Doherty, R.D. (1980) 1st. Riso Int. Symp. 'Recrystallization and Grain Growth in Multi-Phase and Particle-Containing Materials', Roskilde, Denmark, p57.

Doherty, R.D. and Cahn, R.W. (1972) J. Less Common Metals 28 279.

Doherty, R.D. and Martin, J.W. (1962/1963) J. Inst. Metal 91 332.

Duggan, B.J. and Hutchinson, W.B. (1975) Proc. 4th Euro. Conf. on Texture in Metals.

Ebeling, R. and Ashby, M.F. (1966) Phil. Mag. 13 805.

Ells, C.E. and Evans, W. (1963) Trans. A.I.M.E. 227 438.

Embury, J.D., Keh, A.S. and Fisher, R.M. (1966) Trans. A.I.M.E. 236 1252.

Essman, V. (1965) Phys. Status Solidi 12 723.

Exner, H.E. (1972) Int. Met. Rev. 17 25.

Faivre, P. and Doherty, R.D. (1979) J. Mat. Sci. 14 897.

Fisher, J.C., Hart, E.W. and Pry, R.H. (1953) Acta Met. 1 336.

Friedel, J. (1964) Dislocations, Pergammon Press.

Fullman, R.L. (1953) Trans. A.I.M.E. 197 447.

Gatti, A. and Fullman, R.L. (1959) Trans. A.I.M.E. 215 762.

Gjostein, N. and Rhines, F.N. (1959) Acta Met. 7 319.

Gladman, T., McIvor, I.D. and Pickering, F.B. (1971) J.I.S.I. 209 380.

Gottstein, G., Bewerange, J., Mecking, H. and Wollenberger, H. (1975) Acta Met. 23 641.

Gould, D. (1971) D.Phil. Thesis, Oxford University.

Graham, C.D. and Cahn, R.W. (1956) Trans. A.I.M.E. 206 517.

Grant, N.J. (1964) The strengthening of metals, (Ed. Peckner), Reinhold, London, p189.

Granzer, F. and Haase, G. (1961) Z. Phys. 162 504.

Grewen, J., Noda, T. and Sauer, D. (1977) Z. Met. 68 260.

Haessner, F., Hornbogen, E and Mukherjee, M. (1966) Z. Metal. 57 171.

Haessner, F. and Hoschek, G. (1976) Scripta Met. 10 63.

Haessner, F., Hoschek, G. and Tölg, G. (1979) Acta Met. 27 1539.

Hall, E.O. (1954) Nature 173 948.

Hansen, N (1975) Mem. Sci. Rev. Met. 72 189.

Hansen, N. and Bay, B. (1972) J. Mat. Sci. 7 1351.

Hansen, N. and Bay, B. (1979) Met. Trans. 10A 279.

Hansen, N. and Bay, B. (1981) Acta Met. 29 65.

Hazzledine, P.M., Hirsch, P.B. and Louat, N. (1980) 1st. Risø Int. Symp. 'Recrystallization and Grain Growth of Multi-Phase and Particle Containing Materials', Roskilde, Denmark, p159.

Heller, H.W.F., Van Dord, J.H., Wolff, G. and Verbraak, C.A. (1981) Met. Sci. 15 333.

Hibbard, W.R. and Tully, W.R. (1961) Trans. A.I.M.E. 221 336.

Hilliard, J.E. and Cahn, J.W. (1961) Trans. A.I.M.E. 221 344.

Hirsch, P.B., Howie, A., Nicholson, R.B., Pashley, D.W. and Whelan, M.J. (1977) Electron Microscopy of Thin Crystals, Krieger, New York, p51.

Hirsch, P.B. and Humphreys, F.J. (1970) Proc. Roy. Soc. A318 45.

Hirsch, P.B. and Valdré, U. (1963) Phil. Mag. 8 237.

Holt, D. (1970) J. Appl. Phys. 41 3197.

Honeycombe, R.W.K. and Boas, W. (1948) Austr. J. Sci.Res. A1 70.

Hornbogen, E. (1980) 1st. Risø Int. Symp. 'Recrystallization and Grain Growth of Multi-Phase and Particle Containing Materials', Roskilde, Denmark, p198.

Hornbogen, E. and Köster, U. (1978) Recrystallization of metallic materials, (Ed. Haessner), Riederer-Verlag, Stuttgart, p159.

Horuchi, K. Asakura, G., Wasserman, G. and Grewen, J. (1975) Texture 2 17.

Howie, A. (1960) Proc. Euro. Conf. on E.M. Delft, p383.

Hu, H. (1963) Recovery and Recrystallization of Metals (Ed. Himmel), Interscience, New York, p311.

Hu, H. (1969) 'Textures in Research and Practice' (Eds. J.Grewen & G. Wasserman), Springer, Berlin, p200.

Huber, J. and Hatherly, M. (1979) Met. Sci. 13 665.

Humphreys, F.J. (1967) D.Phil. Thesis, Oxford University.

Humphreys, F.J. (1977) Acta Met. 25 1323.

Humphreys, F.J. (1979a) ICSMA 5 1, Aachen, p663.

Humphreys, F.J. (1979b) Acta Met. 27 1801.

Humphreys, F.J. (1979c) Met. Sci. 13 136.

Humphreys, F.J. (1980a) Annales de Chemie 5 25.

Humphreys, F.J. (1980b) 1st. Risø Int. Symp. 'Recrystallization and Grain Growth of Multi-Phase and Particle Containing Materials', Roskilde, Denmark, p35.

Humphreys, F.J. and Martin, J.W. (1966) Acta Met. 14 775.

Humphreys, F.J. and Martin, J.W. (1967) Phil. Mag. 16 927.

Humphreys, F.J. and Stewart, A.T. (1972) Surf. Science 31 389.

Hutchinson, W.B. (1974) Met. Sci. 8 185.

Inman, M.C., Zwilsky, K.M. and Boone, D.H. (1964) Trans. Amer. Soc. Metals 57 701.

Jago, R. and Hatherly, M. (1975) Met. Sci. 9 83.

Johnson, W.A. and Mehl, R.F. (1939) Trans. A.I.M.E. 135 416.

Jones, A.R. and Hansen, N. (1980) 1st. Risø Int. Symp. 'Recrystallization and Grain Growth in Multi-Phase and Particle Containing Materials', Roskilde, Denmark, p13.

Jones, A.R., Ralph, B. and Hansen, N. (1979) Proc. Roy. Soc. A368 345.

Kamma, C. and Hornbogen, E. (1976) J. Mat. Sci. 11 2340.

Karduck, P., Goux, J.M. and Gottstein, G. (1979) ICSMA5, Aachen, p107.

Kneynsberg, H.P., Slakhorst, J.W.H.G and Verbraak, C.A. (1979) Acta Met. 27 101.

Komatsu, N. and Grant, N.J. (1962) Trans. A.I.M.E. 224 705.

Kreisler, A. and Doherty, R.D. (1978) Met. Sci. 12 551.

Langford, G. and Cohen, M. (1969) A.S.M. Trans. Quart. 62 623.

Leslie, W.C., Mickulak, J.T. and Aul, F.W. (1963) Iron and its dilute solid solutions (Ed. C.W. Spencer & F.E. Werner), Interscience, New York, p119.

Lewis, M.H. (1963) D.Phil. Thesis, Oxford University.

Lewis, M.H. and Martin, J.W. (1963) Acta Met. 11 1207.

Li, C.H., Edwards, E.H., Parker, E.R. and Washburn, J. (1953) Acta Met. 1 223.

Li, J.C.M. (1962) J. Appl. Phys. 33 2958.

Liu, Y.C. and Hibbard, W.R. (1953) Trans. A.I.M.E. 197 672.

Lücke, K. and Detert, K. (1957) Acta Met. 5 628.

Lücke, K. and Stuwe, H.P. (1963) Recovery and Recrystallization of metals (Ed. Himmel), Interscience, New York, p171.

Mader, K. and Hornbogen, E. (1974) Scripta Met. 8 979.

Makin, M.J. (1968) Phil. Mag. 18 637.

Malin, A.S. and Hatherly, M. (1974) 8th. Int. Conf. on E.M., Canberra, Australia, 1 582.

Malin, A.S. and Hatherly, M. (1979a) Met. Tech. August 308.

Malin, A.S. and Hatherly, M. (1979b) Met. Sci. 13 463.

Martin, J.W. (1957) Metallurgica 56 161.

Meijering, J.C. and Druyvesteyn, M.J. (1947) Phillips Res. Rep. 2 81, 260.

Messager, C. (1961) Mem. Rev. Sci. Met. 58 557.

Michael, L.C. and Ricketts, B.G. (1967) Trans. A.I.M.E. 239 1841.

Middleton, A.B., Pfeil, L.B. and Rhodes, E.C. (1949-50) J. Inst. Met. 75 595.

Montariol, F. (1963) Metaux et Corrosion 38 323.

Morris, L.R. (1976) ICSMA4, Nancy, France, p649.

Mould, P.R. and Cotterill,P. (1976) Recrystallization and grain growth in metals, Surrey University Press, London.

Neilson, J.P. (1954) Trans. A.I.M.E. 200 1084.

Nobili, D. and De Maria, R. (1965) J. Nucl. Mat. 17 5.

Nutting, J. (1974) 8th Int. Cong. on E.M., Canberra, 1 580.

Orowan, E. (1954) Dislocations in metals, A.I.M.E. p181.

Phillips, V.A. (1966) Trans. A.I.M.E. 236 1302.

Phillips, V.A. (1967) Trans. A.I.M.E. 239 1955.

Phillips, V.A. and Phillips, A. (1952) J. Inst. Met. 81 145.

Porter, J.R. and Humphreys, F.J. (1979) Met. Sci. 13 83.

Preston, O. and Grant, N.J. (1961) Trans. A.I.M.E. 221 164.

Ray, R.K., Hutchinson, W.B. and Duggan, B.J. (1975) Acta Met. 23 831.

Rhines, F.N., Johnson, W.A. and Anderson, W.A. (1942) Trans. A.I.M.E. 147 205.

Richards, T.L. and Pugh, S.F. (1959) J. Inst. Met. 88 141.

Rönnpagel, D., Schulz, G., Hattendorf, H. and Schwink, Ch. (1979) ICSMA5, Aachen, p41.

Russell, K.C. and Ashby, M.F. (1970) Acta Met. 18 891.

Samuels, L.E. (1954) J. Inst. Met. 83 359.

Sandström, R. (1980) 1st. Risø Int. Symp, 'Recrystallization and Grain Growth in Multi-Phase and Particle Containing Materials', Roskilde, Denmark, p45.

Schofield, T.H. and Bacon, A.E. (1961) Acta Met. 9 653.

Smith, C.J.E. and Dillamore, I.L. (1970) Met. Sci. 4 161.

Smith, C.S. (1948) J. Inst. Met. 74 747.

Swann, P.R. (1963) Electron Microscopy and Strength of Crystals, (Ed. G. Thomas & J. Washburn), Interscience, New York.

Tabata, T., Yamanaka, S. and Fujita, H. (1978) Acta Met. 26 405.

Tabor, D. (1951) J. Inst. Metal 79 1.

Tanner, L.E. and Sevri, I.S. (1966) Met. Sci. & Eng. 1 153.

Ticknor, L.B. and Bever, M.B. (1952) Trans. A.I.M.E. 194 941.

Thompson, S.J. and Flewitt, P.E.J. (1975) J. Less Common Metals 40 269.

Underwood, E.E. (1970) Quantitative Stereology, Addison Wesley, p18.

Van Arkel, A.E. and Burgers, W.G. (1930) Z. Physik 48 690.

Vandermeer, R.A. and Gordon, P. (1959) Trans. A.I.M.E. 215 577.

Vandermeer, R.A. and Gordon, P. (1963) Recovery and recrystallization of metals (Ed. Himmel), Interscience, New York.

Vandermeer, R.A. and Snyder, Jr., W.B. (1977) Met. Trans. 10A 1031.

Vasudevan, A.K., Petrovic, J.J. and Roberson, J.A. (1974) Scripta Met. 8 861.

Viswanathan, R. and Bauer, C.L. (1973) Acta Met. 21 1099.

Wakefield, P.T., Malin, A.S. and Hatherly, M. (1977) J. Aust. Inst. Met. 22 143.

Walter, J.L. and Dunn, C.G. (1959) Acta Met. 7 424.

Walter, J.L and Koch, G.F. (1963) Acta Met. 11 923.

Welsch, G., Young, B.J. and Hehemann, R.F. (1979) ICSMA5 3, Aachen, p1693.

Westerman, E.J. and Lenel, F.V. (1960) Trans. A.I.M.E. 218 1010.

Williams, W.H. and Eborall, R. (1953) J. Inst. Met. 81 501.

Wingrove, A.L. (1972) J. Inst. Metals 100 313.

Wood, D.L. (1959) Trans. A.I.M.E. 215 925.